Summer 2017

R&D of a High-Performance DIRC Detector For a Future Electron-Ion Collider

Stacey Lee Allison
Old Dominion University

R&D OF A HIGH-PERFORMANCE DIRC DETECTOR FOR A FUTURE ELECTRON-ION COLLIDER

by

Stacey Lee Allison
B.S. May 2012, University of North Georgia
B.S. May 2012, University of North Georgia
M.S. May 2014, Old Dominion University

A Dissertation Submitted to the Faculty of
Old Dominion University in Partial Fulfillment of the
Requirements for the Degree of

DOCTOR OF PHILOSOPHY

PHYSICS

OLD DOMINION UNIVERSITY
August 2017

Approved by:

Charles Hyde (Director)

Mark Havey (Member)

Grzegorz Kalicy (Member)

Jay Van Orden (Member)

Mike Overstreet (Member)

ABSTRACT

R&D OF A HIGH-PERFORMANCE DIRC DETECTOR FOR A FUTURE ELECTRON-ION COLLIDER

Stacey Lee Allison
Old Dominion University, 2017
Director: Dr. Charles Hyde

An Electron-Ion Collider (EIC) is proposed as the next big scientific facility to be built in the United States, costing over $1 billion in design and construction. Each detector concept for the electron/ion beam interaction point is integrated into a large solenoidal magnet. The necessity for excellent hadronic particle identification (pion/kaon/proton) in the barrel region of the solenoid has pushed research and development (R&D) towards a new, high-performance Detection of Internally Reflected Cherenkov light (DIRC) detector design. The passage of a high energy charged particle through a fused silica bar of the DIRC generates optical Cherenkov radiation. A large fraction of this light propagates by total internal reflection to the end of the bar, where the photon trajectories expand in a large volume before reaching a highly segmented photo-detector array. The spatial and temporal distribution of the Cherenkov light at the photo-detector array allows one to reconstruct the angle of emission of the light relative to the incident charged particle track. In order to reach the desired performance of 3σ π/K separation at 6 GeV/c particle momentum a new 3-layer spherical lens focusing optic with a lanthanum crown glass central layer was designed to have a nearly flat focal plane. In order to validate the EIC DIRC simulation package, a synergistic test beam campaign was carried out in 2015 at the CERN PS with the PANDA Barrel DIRC group using a prototype DIRC detector. Along with the analysis of the CERN test beam data, measurements of the focal plane of the 3-layer lens were performed using a custom-built laser setup at Old Dominion University. Radiation hardness of the lanthanum crown glass was tested using a 160 keV X-ray source and a monochromator at the Catholic University of America. Results of these test-bench experiments and the analysis of the 2015 CERN test beam data are presented here.

ACKNOWLEDGEMENTS

The work presented in this manuscript was carried out with support from the U.S. Department of Energy, the Brookhaven National Laboratory "Generic Detector R&D Program for the EIC" (eRD14), and GSI Helmholtzzentrum für Schwerionenforschung GmbH.

I would like to thank my thesis advisor, Dr. Charles Hyde, for his patience and understanding in allowing me to work on a project that I truly enjoy.

I would like to thank my thesis supervisor, Dr. Grzegorz Kalicy, for all of his guidance in learning DIRC technology.

I would like to thank my collaborators at GSI for giving me the opportunity to experience working hands-on with a DIRC detector.

Finally, I would like to thank all my friends and family, especially my parents Jennifer and Stacy Allison. Without their love and support I would not be where I am today.

TABLE OF CONTENTS

LIST OF TABLES

LIST OF FIGURES

CHAPTER 1

INTRODUCTION

The Electron-Ion Collider (EIC) is planned as the Department of Energy's next big nuclear physics facility to be built in the Unite States. It will be the world's first collider with polarized electron and ion beams, as well as having the capability of delivering beams of heavier, unpolarized ions. Electron beam energies reaching $2 - 21$ GeV/c and proton beam energies up to 250 GeV/c necessitate a sophisticated 4π detector.

Excellent hadronic particle identification (PID) not only at the end-caps but also in the barrel region around the beam-beam interaction point is crucial for the success of the physics program of an EIC. For the end-caps there is ample space for Ring Imaging Cherenkov (RICH) detectors which have been shown to provide excellent PID for large momentum particles, however, due to the limited space available in the barrel region a different approach must be taken. A modified RICH detector, known as a DIRC (Detection of Internally Reflected Cherenkov light) [1] is an attractive solution for PID of particles with large transverse momentum transfer as it occupies less than 5 cm of radial space while still providing excellent PID performance, as shown by the performance of the BaBar barrel DIRC [2].

Although based on the design of BaBar's barrel DIRC, a DIRC at an EIC presented many challenges in reaching the required π/K separation power of 3σ at 6 GeV/c particle momentum. A more compact expansion volume necessitated the design of a new 3-layer spherical lens focusing optic to improve resolution. Testing of this new lens installed in a prototype DIRC detector was done in a particle beam at the CERN Proton Synchrotron (PS) to test and compare the performance of the 3-layer lens design with other focusing and radiator options.

Along with performance in a particle beam the new lens was also subjected to radiation hardness tests using a 160 keV X-ray source to determine the durability of the lanthanum crown glass used for the middle layer of the lens. The "flat" focal plane of a prototype lens was also measured and compared to simulation prediction.

CHAPTER 2

ELECTRON-ION COLLIDER

It has been known for nearly a century that neutral atoms are composed of Z electrons and a nucleus containing Z protons and N neutrons. It took another 50 years for Murray Gell-Mann and George Zweig to independently develop a model proposing that nucleons themselves are made up of constituent components, called quarks, bound together by the exchange of gluons [3]. This led to the development of the fundamental theory of the strong interaction, known as Quantum Chromo-Dynamics (QCD) [4]. It is now a strong goal of the nuclear physics community to understand the interactions of quarks and gluons and how those interactions make manifest both nucleons themselves, which account for nearly all the mass of the visible matter in the universe, as well as the nucleons' spin, mass, magnetic moment, and nuclear binding energy. Because of the well-known properties of the electromagnetic interaction, electron scattering is an ideal process for such studies.

Although it would theoretically be possible to study these properties using fixed-target electron beam experiments, it is three-fold prohibitive: (a) it is much more costly to construct an accelerator to accelerate electrons to the necessary momentum (on the order of TeV) than to build a collider, (b) it is more difficult and complicated to do transverse nucleon polarization studies with a fixed target due to the nature of the required magnetic fields, and (c) it is very difficult to study the target fragments of a fixed target reactions due to the lower energy of the final state products, whereas in a collider the fragments will be boosted in the same direction as the ion beam. In the 2007 Nuclear Science Advisory Committee's (NSAC) Long-Range Plan, research and development of an Electron-Ion Collider (EIC) was given priority [5]. In the 2015 NSAC Long-Range Plan an EIC was endorsed and deemed a priority as the next major facility to be built in the United States [6].

The EIC will not be the first facility to have the capability of colliding electrons and positrons with protons. The HERA accelerator in Hamburg, Germany was the world's first electron-proton collider, reaching electron energies of up to 28 GeV and protons to nearly 1 TeV with a luminosity on the order of 10^{31} cm^{-2} s^{-1} before shutting down in 2007. Figure 1 shows the combined H1 and Zeus experimental data from HERA for the measurement of the structure function for positron-proton scattering along with fixed target data for a

wide range of both x, the Bjorken scaling variable, and Q^2, the square of the quark four-momentum transfer [7]. The structure function quantifies the distribution of longitudinal momentum fraction x, at the resolution scale $1/Q^2$. Note that here x is the Bjorken variable and not the quark momentum fraction, given by

$$X = \frac{q^0 + q^z}{P^0 + P^z} \tag{1}$$

where q and P are the quark and proton four-momentum respectively. In DIS, however, given the hypothesis of a free scattering on quarks with mass $m_q^2 \ll 1$ implies that $X \to x = \frac{Q^2}{2p \cdot P}$.

The EIC hopes to improve upon the already rich science produced at HERA threefold: (a) by increasing the luminosity of the accelerator to on the order of 10^{34} cm^{-2} s^{-1}, (b) by allowing for the use of ion beams from deuterium to uranium, and (c) by allowing for both transversely and longitudinally polarized beams of electrons and light ions. With these improvements the EIC will be able to look into hadronic initial and final states with much greater detail than previous experiments.

2.1 SCIENCE GOALS

The goal of an EIC is to discover the mechanisms by which QCD is responsible for the structure and dynamics of nucleons, the nature of the nucleon-nucleon force, and the universal features of the gluon distributions at high density in the proton at low x.

2.1.1 NUCLEON SPIN

One major question still challenging nuclear physicists is "What is the origin of the nucleon spin?". In the 1980s the naive answer was that the total nucleon spin was the sum of the spin of its three valance quarks, but many years of experimentation has revealed that it is much more complicated (Fig. 2), with the contributions both from quark and gluon spin and orbital angular momentum still in question. The EIC will be capable of much more detailed study of the contributions to the nucleon structure by enabling multi-dimensional projections of the distribution of quarks and gluons in space, longitudinal and transverse momenta, spin, and flavor.

2.1.2 THE EMC EFFECT

It was first observed by the European Muon Collaboration (EMC), and confirmed by other experiments that there is a modification between the nucleon structure function, F_2,

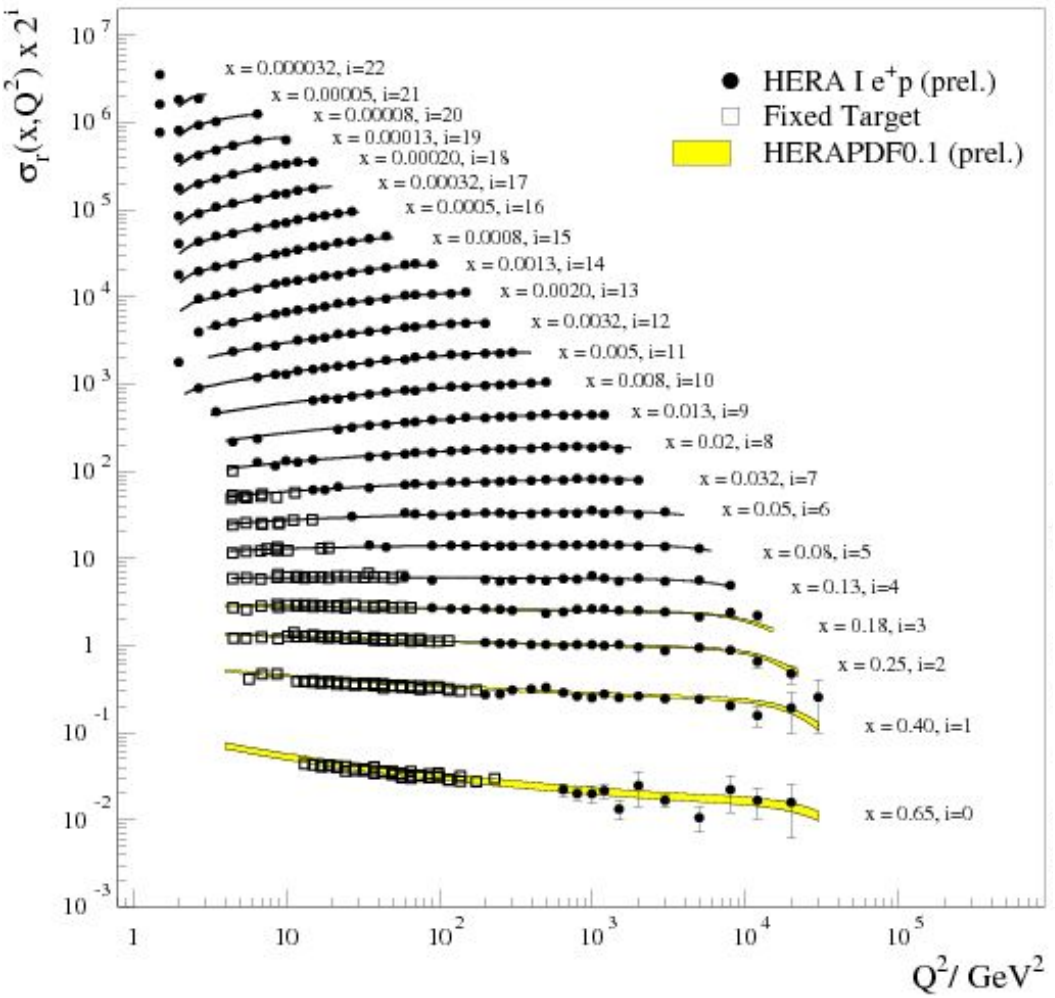

FIG. 1: The reduced cross section $\sigma_r(x, Q^2)$ as a function of Q^2. Filled circles are combined H1 and Zeus data from HERA for proton-positron collisions, hollow squares are from fixed target experiments, and the yellow are the Q^2 predictions from HERAPDF0.1 [7].

of deuterium to those of heavier elements as a function of Bjorken x [9]. Figure 3 shows the ratios of the Deep Inelastic Scattering (DIS) cross sections of ^{3}He (top) to Deuterium and ^{4}He (bottom) to Deuterium as examples of this effect. Initial assumptions were that these cross section ratios would be unity, but measurements have clearly shown a suppression in this ratio for $0.3 < x < 0.8$, the now-called EMC Effect. One can also see an enhancement of the ratio for $0.1 < x < 0.3$ known as anti-shadowing, and the region of $x < 0.1$ where the ratio is again suppressed is the shadowing region.

The reason for this modification to the DIS cross section is still a mystery, but the EIC hopes to shed light on this phenomenon by studying various coherent exclusive reactions,

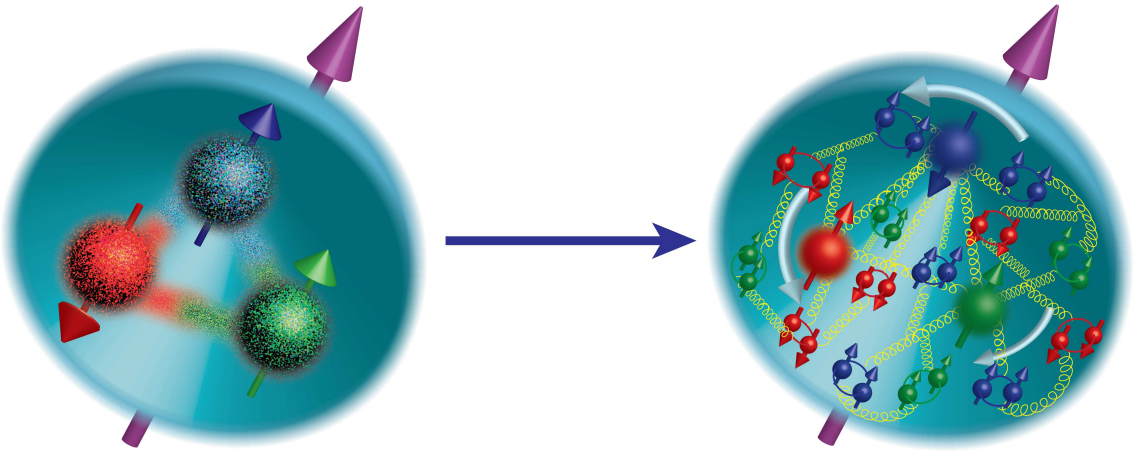

FIG. 2: Evolution of our understanding of nucleon spin structure. Left: In the 1980s, a nucleons spin was naively explained by the alignment of the spins of its constituent quarks. Right: In the current picture, valence quarks, sea quarks and gluons, and their possible orbital motion are expected to contribute to overall nucleon spin [8].

such as J/Ψ production via $eA \rightarrow eAJ/\Psi$, which could allow for the quantification of initial conditions in heavy-ion collisions by mapping out the geometry of the nucleus in high-energy processes. This mapping can also help to understand other collective dynamics in inelastic collisions, such as the shadowing and anti-shadowing effects. where multiple nucleons interact coherently with the probe.

2.1.3 GLUON DISTRIBUTIONS INSIDE NUCLEI

As mentioned above, the EMC effect, the modification of the distribution of quarks in a nucleus versus their distribution in nucleons, is a known (yet still mysterious) phenomenon. It is suspected that this modification also occurs for gluons, with experiments such as ALICE showing evidence for gluon shadowing for $x \approx 10^{-3}$ [11]. The EIC hopes to measure this suppression of the structure functions thanks to its wider range of kinematics both in x and Q^2, allowing not only for the measurement of gluon shadowing ($x < 0.05$), but also anti-shadowing ($x \approx 0.1$), and possibly the EMC effect for gluons ($x > 0.3$), shedding light on the origins of the EMC effect.

2.2 FACILITIES

As of the writing of this thesis there are two competing designs for an EIC facility to

be built in the United States: a figure-8 accelerator design for Thomas Jefferson National Accelerator Facility (JLab) (Figure 4), and a LINAC-ring (or ring-ring) accelerator design for Brookhaven National Lab (BNL) (Figure 5).

The JLab EIC (JLEIC) is planned to be approximately 1.4 km in circumference and have a footprint of roughly 500 m by 170 m. The design is a ring-ring with electrons and ions being stored in separate beam lines and collided at two interaction points (IPs) (outlined in red in Figure 4) on the figure-8. The JLab CEBAF SRF linac will be used as an electron injector for electrons with 3 - 11 GeV/c momentum. The second ring will store an ion beam with momentum of 20 to 100 GeV/c for protons, up to 50 GeV/c per nucleon for light to medium mass N = Z nuclei, and up to 40 GeV/c per nucleon for heavy nuclei. The ion beams are generated and accelerated in a new ion injector complex with a LINAC plus figure-8 design that will be utilized to preserve ion polarization. The two main rings will be stacked vertically in the same underground tunnel [12].

The BNL facility, named eRHIC, will use a new electron beam facility based on an Energy Recovery LINAC that will be built inside of the Relativistic Heavy Ion Collider (RHIC) tunnel to collide with RHIC's pre-existing polarized proton/ion beam. The existing hadron ring will accelerate protons up to 250 GeV/c, $^3He^{+2}$ up to 167 GeV/c per nucleon, and heavier ions (e.g. gold or uranium) up to 100 GeV/c per nucleon. The new electron ring will be capable of producing electrons from 2 - 21 GeV/c [13]. Figure 5 shows the current design layout of the eRHIC facility (top) and the Brookhaven eA Solenoidal Tracker (BeAST) detector proposed for the interaction region (bottom).

2.2.1 PARTICLE IDENTIFICATION REQUIREMENTS AND SOLUTIONS

The large center of mass energies and diverse physics program at an EIC necessitate a very sophisticated detector suite. The most basic process that the EIC will observe is inclusive DIS with nearly full reconstruction of the hadronic final state. The ability to accurately identify hadrons in the final state is therefore a key requirement for the physics program, as is shown by Figure 6 which shows the momentum distributions of pions and kaons for each region of interest for typical beam energies for both BNL and JLab.

As can be seen in Figures 4 and 5, the layouts of the two detector concepts for JLab and BNL are slightly different, but the solutions for PID requirements are very similar. In the hadron endcap, because of the large final state energies the ideal PID detector would be a gaseous, mirror-based Ring Imaging Cherenkov (RICH) detector. This will provide $\pi/K/p$ separation up to 50 GeV/c momentum. The hadrons produced going towards the

electron endcap scales in both energy and quantity with the energy of the electron beam energy. Although the maximum electron beam energies of JLab and BNL differ, PID up to 10 GeV/c momentum seems to be suitable for both facilities, and so a modular aerogel RICH detector is currently under development. In the central barrel region the necessary momentum coverage is not as high as that of the endcaps because the transverse momentum transfer from the electron beam to the ion beam is generally less than 10 GeV/c. This smaller momentum range coupled with a smaller space to fit a detector make a detector based on Detection of Internally Reflected Cherenkov light (DIRC) technology a desirable choice.

The design and prototype testing of components for a high-performance DIRC detector is the subject of this thesis and an ideal solution for PID in the EIC barrel region.

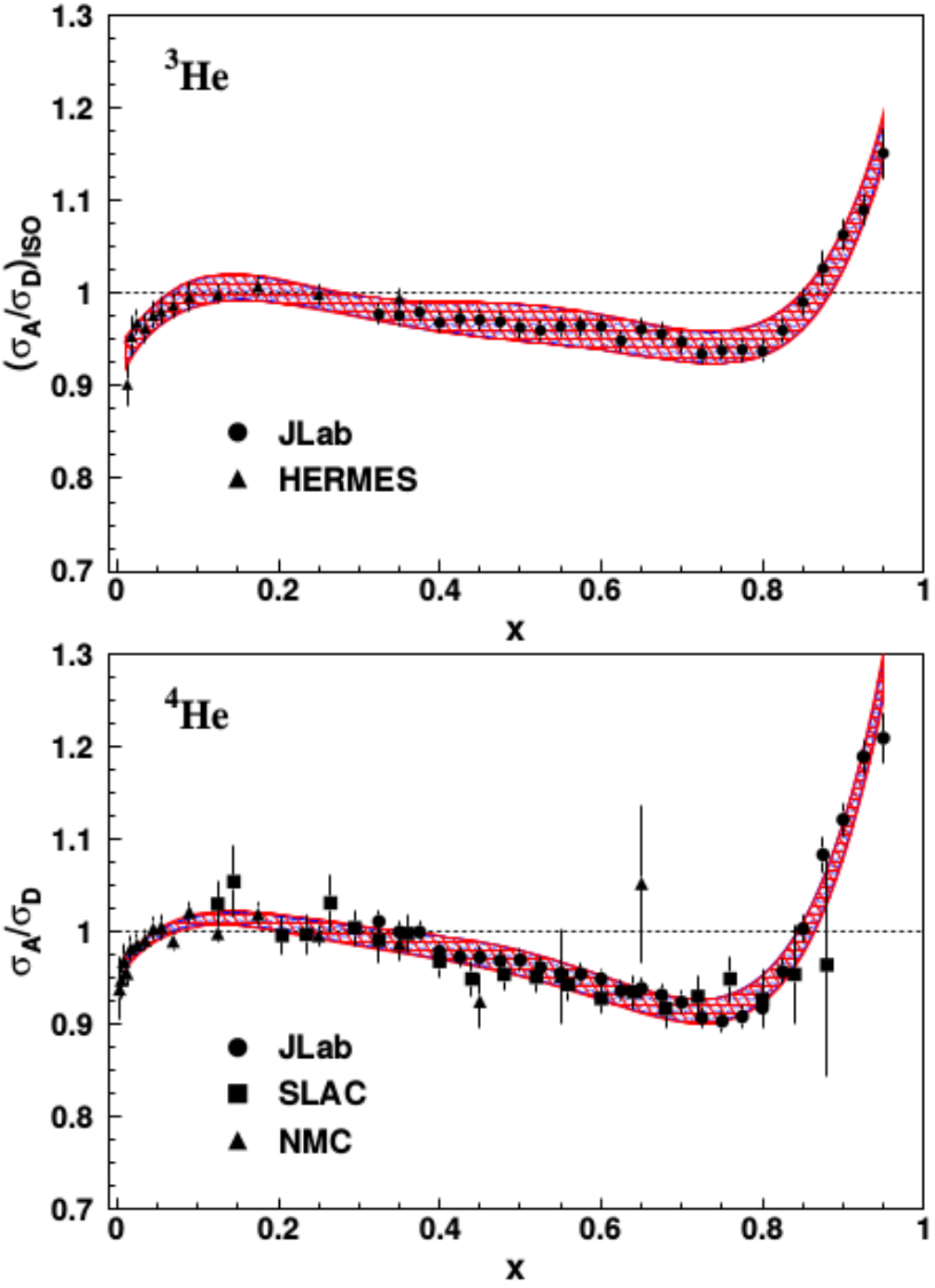

FIG. 3: Two examples of the EMC effect. Top: Ratios of ^{3}He to Deuterium DIS cross sections from JLab (circles) and HERMES (triangles). Bottom: Ratios of ^{4}He to Deuterium DIS cross sections from JLab (circles), SLAC (squares), and HERMES (triangles) [10].

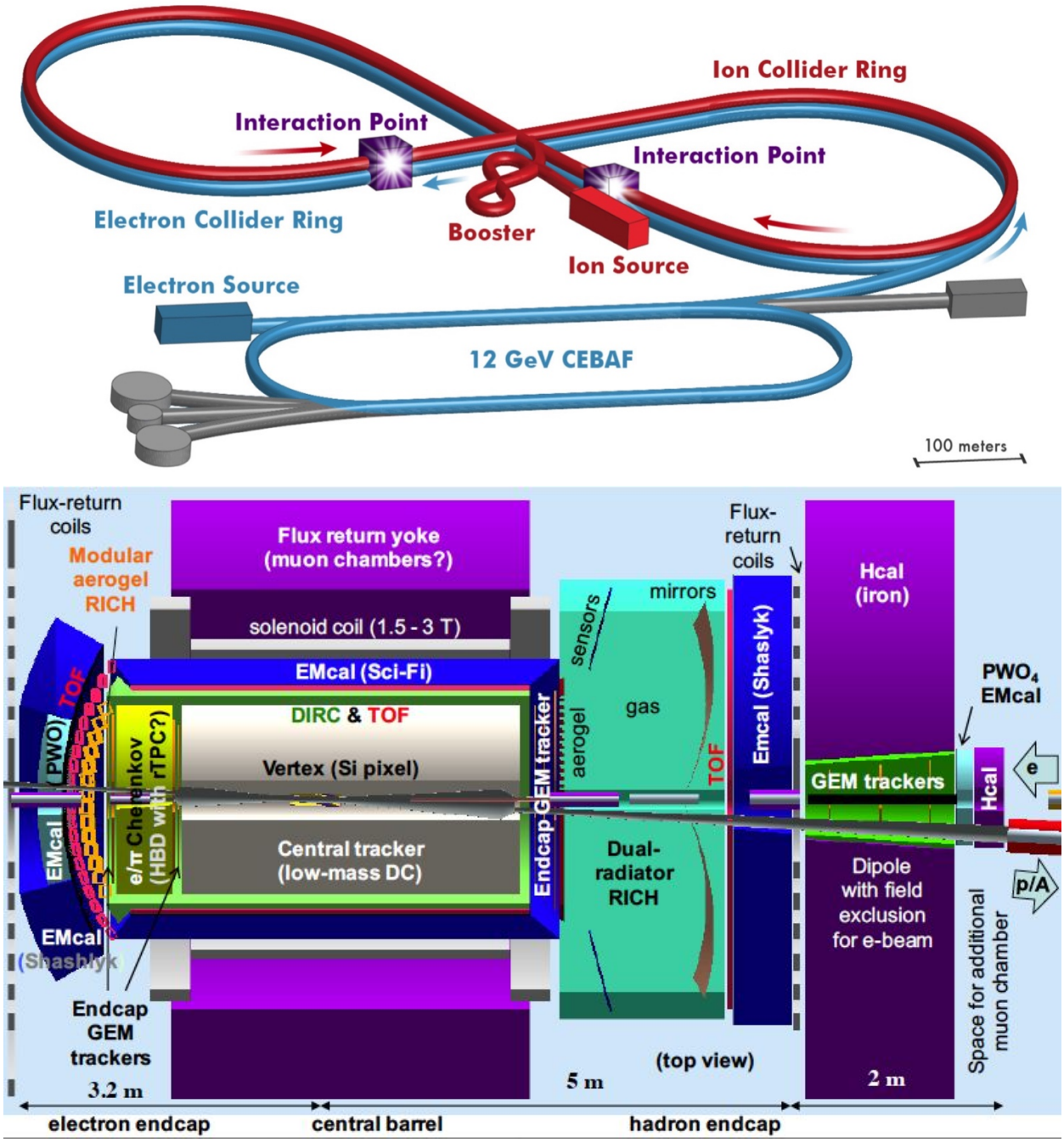

FIG. 4: The top figure is a design of the EIC facility for JLab. The two interaction points (IP) are highlighted in purple, and the current baseline design for the detector at the left-most IP is shown at the bottom [14].

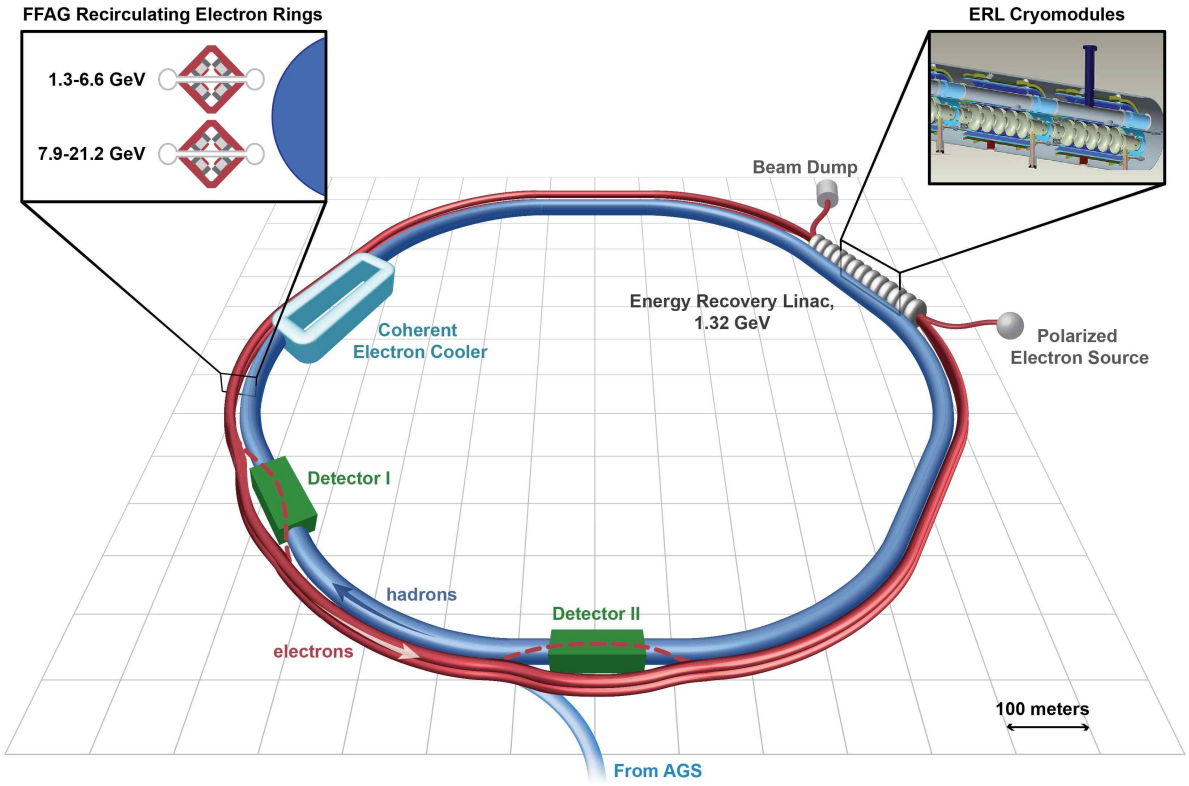

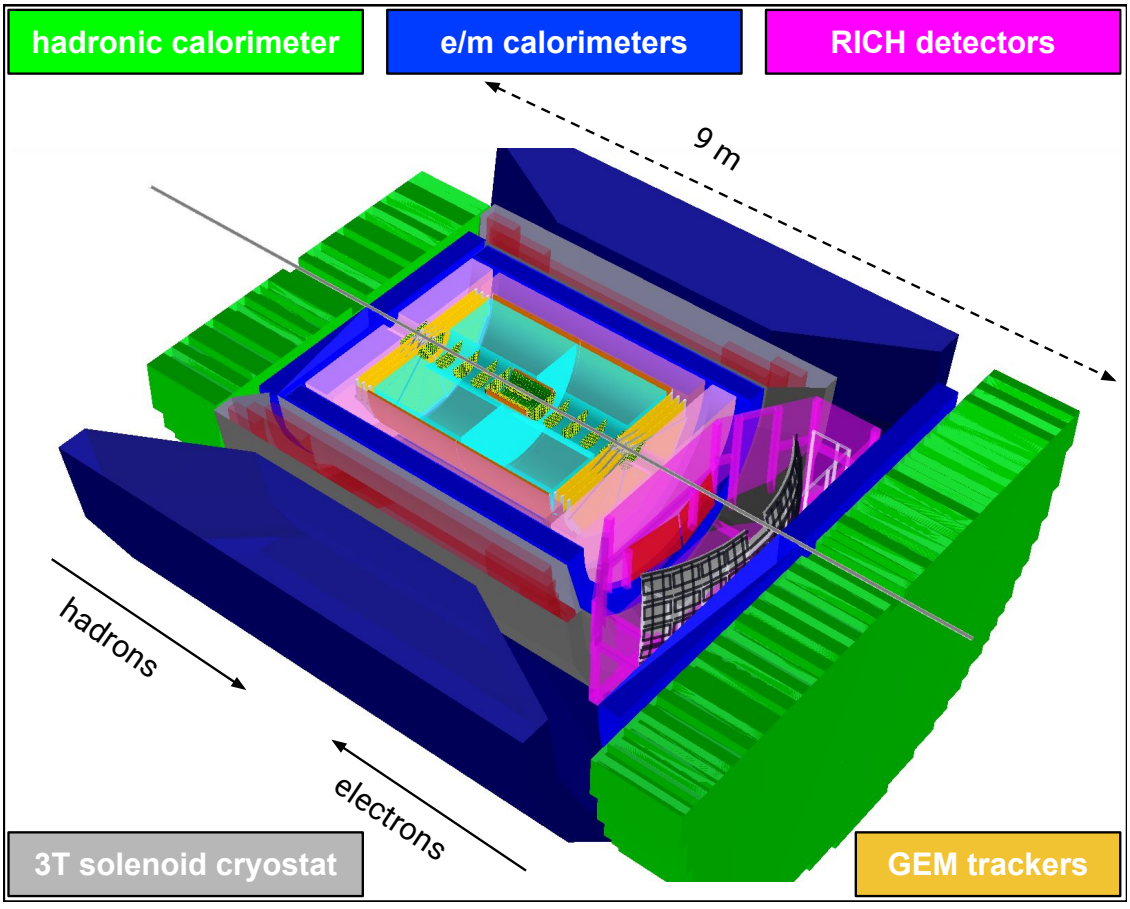

FIG. 5: The top figure is a design of the LINAC-ring option for an EIC facility at BNL. The proposed BeAST (Brookhaven eA Solenoidal Tracker) detector is shown at the bottom [14].

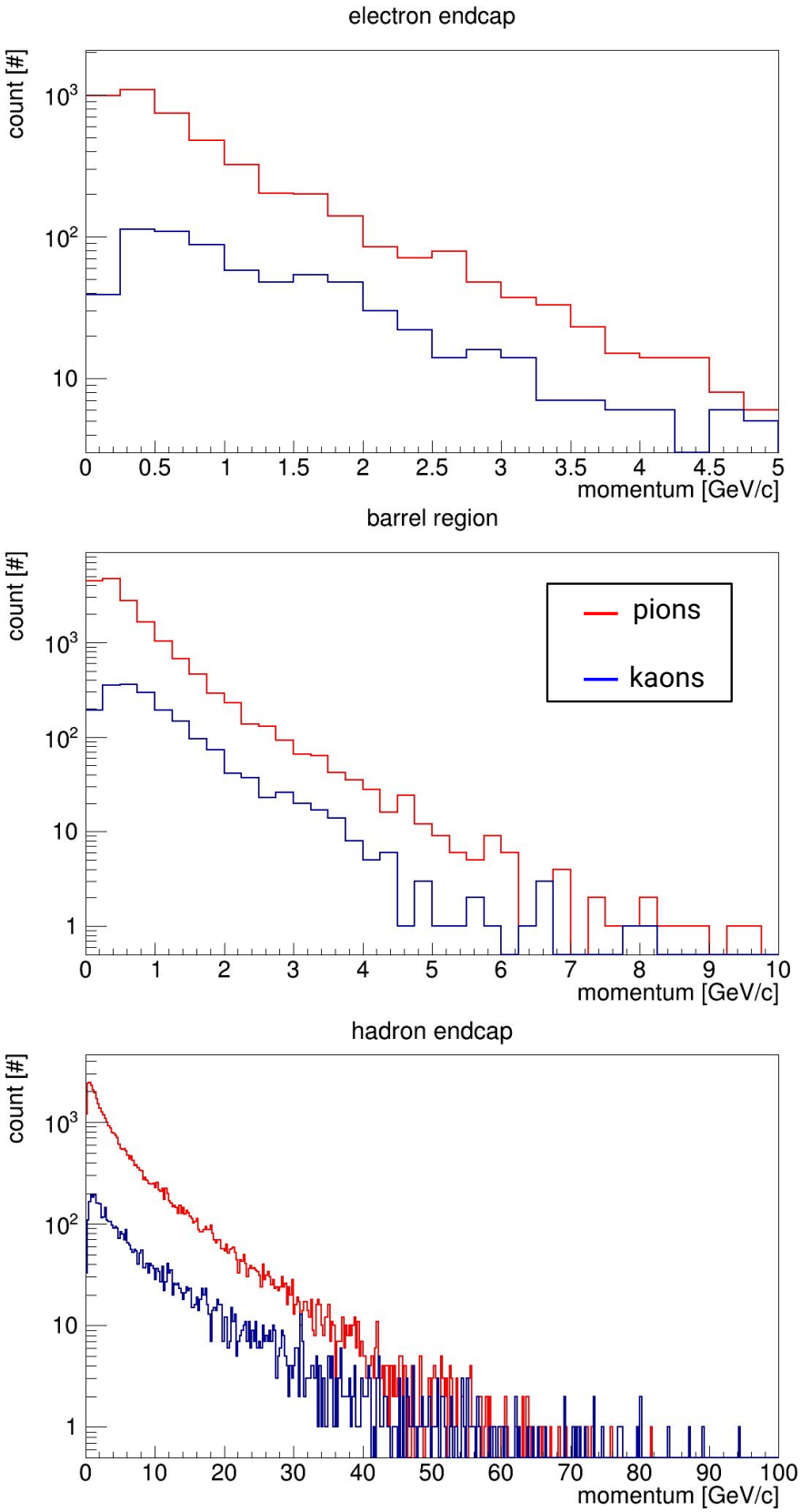

FIG. 6: Momentum distributions for pions (red) and kaons (blue) in the electron endcap (top), barrel region (middle), and hadron endcap (bottom). Plots were produced using the pythia simulation package for DIS events corresponding to collisions between 10 GeV electrons and 100 GeV protons, a common BNL/JLab kinematic, shown for a bin of $10 < Q2 < 100$ GeV^2 [14].

CHAPTER 3

DIRC TECHNOLOGY

DIRC detectors are based on the concept of the Detection of Internally Reflected Cherenkov light (DIRC) produced in a solid radiator (typically fused silica) to identify charged particles. It is a special type of Cherenkov counter, which uses the unique properties of Cherenkov radiation to separate charged particle species.

3.1 CHERENKOV RADIATION

Einstein postulated in his Theory of Relativity that the speed of light in a vacuum, c, is the limit of the velocity of massive particles. In an optically transparent medium, however, the speed at which light propagates is modified: $c_{med} = c/n$, where n is the index of refraction of the medium. Pavel Cherenkov discovered in 1934 that massive particles moving through a medium faster than the speed of light in that medium emit light in the form of now-called Cherenkov radiation. Cherenkov was able to establish several interesting properties of this radiation: it is only emitted from charged particles above a certain velocity threshold $v > c/n$, the intensity is proportional to the particle's path length, emission is prompt, and the light is polarized with a continuous wavelength spectrum. Later, in 1937, Ilya Frank and Igor Tamm theoretically formulated this radiation with fantastic agreement to Cherenkov's findings, and the three shared the 1958 Nobel Prize in Physics for their efforts [15].

Further studies confirmed that Cherenkov radiation is emitted uniformly in azimuth (ϕ_c) around the particle's direction of travel with the polar opening angle θ_C defined as

$$\cos\theta_C = \frac{1}{\beta n(\lambda)}, \tag{2}$$

where $\beta = v_p/c$, v_p is the particle's velocity, and the index of refraction is a function of the emitted photon wavelength. In a typical, dispersive optical medium the opening half-angle of the shock wave produced by the Cherenkov radiation, η_C defined in Figure 7, is not complementary to the Cherenkov angle. The relationship between the two is given by

$$\cot\eta_C = \left[\frac{\mathrm{d}}{\mathrm{d}\omega}(\omega\tan\theta_C)\right]_{\omega_0} = \left[\tan\theta_C + \beta^2\omega n(\omega)\frac{\mathrm{d}n}{\mathrm{d}\omega}\cot\theta_C\right]_{\omega_0} \tag{3}$$

where ω_0 is the central value of the considered frequency range. Because the second term in (3) is zero only for non-dispersive media the shock wave front is not perpendicular to the Cherenkov cone in real detectors.

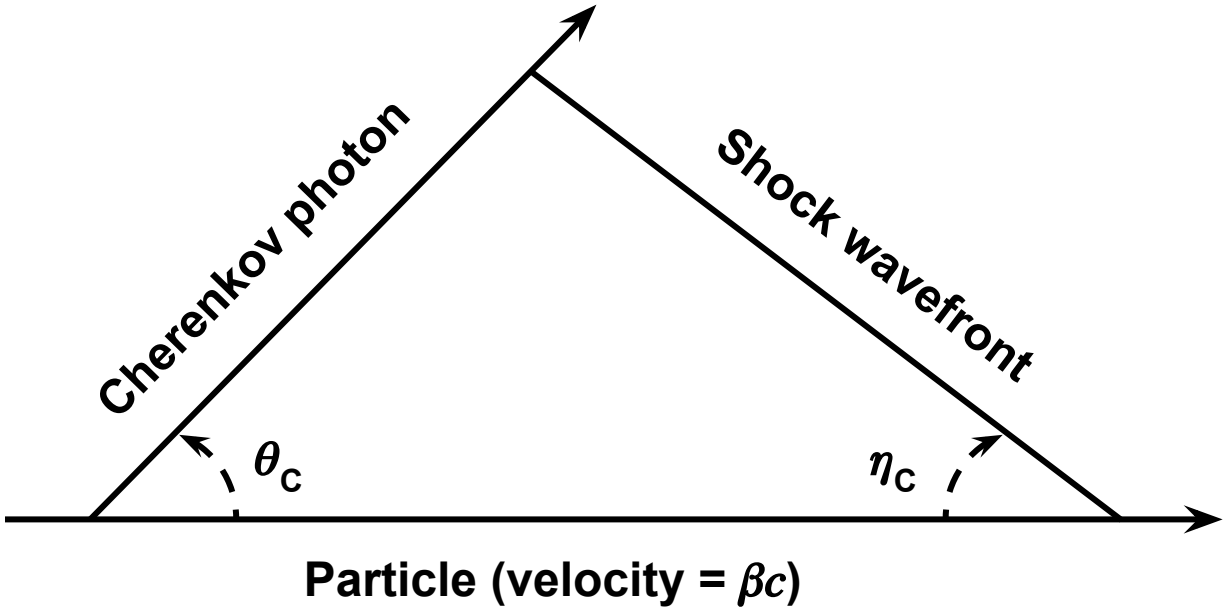

FIG. 7: Illustration of the Cherenkov cone [16].

Because particles lose very little energy when radiating Cherenkov photons the emission is very weak. The number of photons $N_{photons}$ emitted per path length L (in cm) by a moving particle with charge z is given by the Frank-Tamm equation

$$\frac{N_{photons}}{L} = \frac{\alpha^2 z^2}{r_e m_e c^2} \int \sin^2 \theta_C(E) \mathrm{d}E \tag{4}$$

where E is the photon energy in eV, the integral is taken over the region where $n(E)$ is greater than 1, $\alpha = \frac{1}{137}$ is the fine structure constant, z is the projective charge in units of electron charge, and $\frac{\alpha^2}{r_e m_e c^2} = 370$ cm^{-1} eV^{-1}.

3.2 APPLYING THE CHERENKOV EFFECT TO PARTICLE ID

In order to identify particle species one must know both the mass and charge of the particle in question. Because the Cherenkov angle encodes the particle's velocity it is, in principle, a simple matter to measure the particle's momentum with a tracking chamber as well as the velocity obtained from (2) to determine the mass and charge. Figure 8 shows how different particle species can be distinguished for a given momentum in fused silica.

Threshold counters are Cherenkov detectors used for particle identification (PID) by exploiting the fact that only particles above the threshold velocity $\beta > 1/n$ will emit Cherenkov photons. Therefore lighter particles will emit Cherenkov light while heavier particles will not for a given momentum.

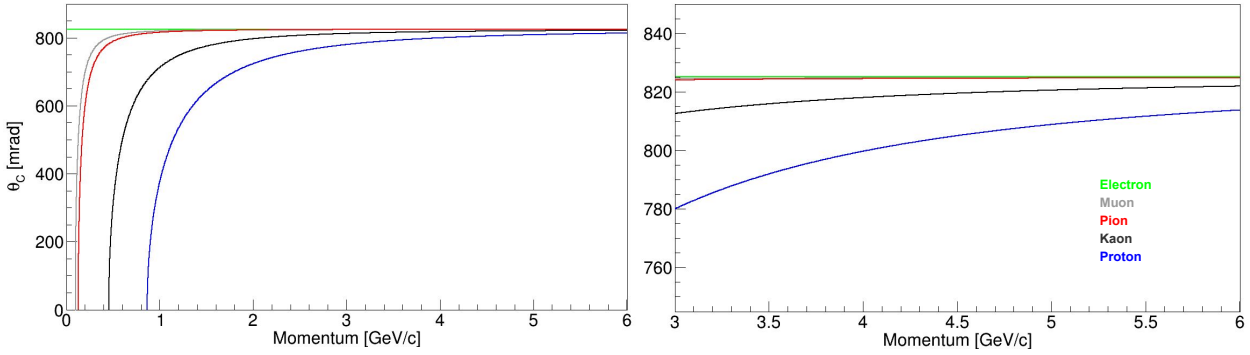

FIG. 8: Particle momentum (in GeV/c) versus Cherenkov angle (in mrad) for different particle species in fused silica ($n \approx 1.473$). While the full range (left) makes it seem as if separation between heavier species becomes more and more challenging, zooming in (right) shows that it is indeed to possible separate protons, kaons, and pions even at higher particle momentum.

3.3 RING IMAGING DETECTORS

Ring Imaging Cherenkov (RICH) detectors are designed to efficiently identify and separate different particle species over a wide range of momenta.

The information about a particle's velocity can be combined with momentum information from a tracking system to determine the mass as [16]

$$m = \frac{p}{c}\sqrt{n^2 \cos^2 \theta_C - 1} \tag{5}$$

A basic RICH system is shown in Figure 9. A volume of radiator, either gaseous (e.g. C_4F_{10}) or solid (e.g. aerogel), is positioned upstream of an array of photosensors. A charged particle traveling through a thin radiator above the threshold velocity will continuously emit Cherenkov photons in a cone. The resulting image on the photosensor array is an annulus of thickness $d \tan \theta_C$ and an inner radius of $L \tan \theta_C$, where d is the distance the particle traveled inside the radiator, L is the distance between the radiator and the photosensors, and θ_C is the usual Cherenkov angle (Figure 9b). PID is done by measuring the average radius of the annulus and reconstructing the Cherenkov angle geometricly.

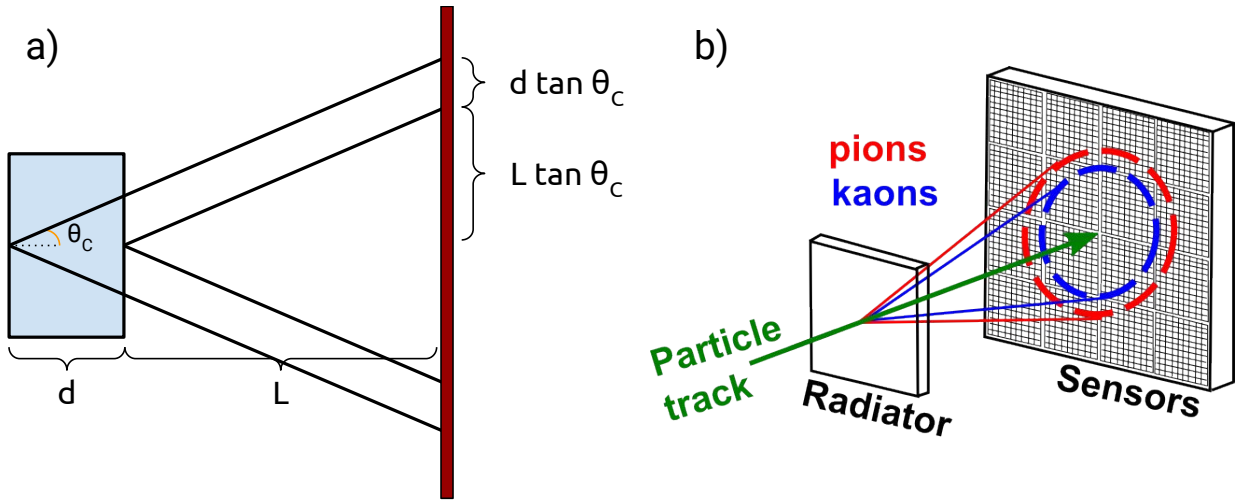

FIG. 9: Basic concept of a proximity focusing Ring Imaging Cherenkov (RICH) detector (a), and an example of how they can be used to do PID based on particle mass (b) [17].

3.4 DIRC DETECTORS

DIRC detectors work much the same way as a RICH in that they collect Cherenkov photons produced from a radiating material and use the created image on the photosensors to reconstruct the Cherenkov angle. In the case of a DIRC, the radiating medium is also used as a light guide as some of the Cherenkov photons undergo total internal reflection inside the radiator and are guided towards one end of the radiator to a readout (Figure 10). The radiator of choice is a solid bar made of fused silica, with an index of refraction $n = 1.468$ at a photon wavelength of $\lambda = 420$ nm. A rectangular cross section and highly smoothed and polished sides ensure that the magnitude of the Cherenkov angle is preserved to within < 1 mrad during internal reflection. Photons that are created propagating away from the readout are reflected back towards the readout by a mirror. Once the photons exit the radiator they are allowed to separate through an expansion volume before being imaged in both (x, y) position as well as time. The arrival position and propagation time of each detected photon are combined with tracking information to reconstruct the Cherenkov angle and determine the corresponding PID likelihoods (reconstruction methods and techniques for DIRC detectors will be discussed in detail in Chapter 6).

The performance of a DIRC detector is given by the resolution in the Cherenkov polar opening angle of the particle track, $\sigma^2_{\theta_C,\text{track}}$, which can be written as:

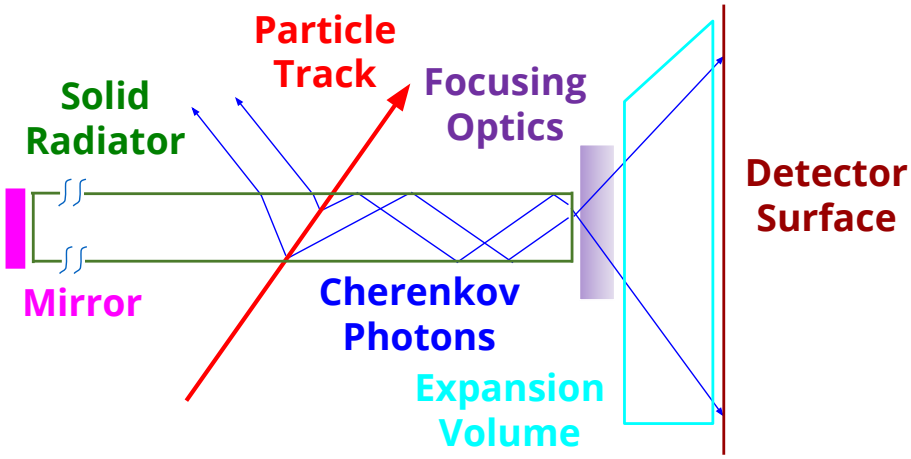

FIG. 10: The basic components of a DIRC detector. A solid radiator, typically fused silica (green); a mirror to redirect backward-going photons (pink); optional focusing optics (purple); an expansion volume to allow photons to separate in space (cyan); and a detector surface (brown) to record the position and arrival time of Cherenkov photons (blue).

$$\sigma^2_{\theta_C,\text{track}} = \sigma^2_{\theta_C}/N_\gamma + \sigma^2_{\text{correlated}} \tag{6}$$

where σ_{θ_C} is the average single photon Cherenkov angle resolution, N_γ is the number of measured photons per track, and $\sigma_{\text{correlated}}$ includes several correlated terms that contribute to the resolution such as the uncertainty in the particle track direction coming from external tracking systems, chromatic dispersion, and pixel size. Because the track direction is crucial to the reconstruction of the Cherenkov angle, this error needs to be small for the performance to not suffer. For the EIC a tracking resolution on the order of 1 mrad is required for adequate PID.

As of the writing of this thesis the only DIRC detector used in a full experiment is the BaBar DIRC at SLAC National Accelerator Laboratory, which was successfully operated from 1999 through 2008 [2]. It proved to be a robust, stable, and easy to operate system for more than 8 years, providing excellent pion/kaon separation for all tracks from B-meson decays. It used 4.9 m long radiator bars with a rectangular cross section of 17.25×35 mm^2. Each bar was made of four 1.225 m long fused silica bars glued end-to-end. The bars were placed in 12 hermetically sealed containers, called bar boxes, each holding 12 radiator bars for a total of 144 bars. At the end of each box was attached a wedge of fused silica and a window to allow the photon image to expand before entering the water-filled expansion volume and being read out on one of 10,752 photomultiplier tubes (see Figure 11). Figure

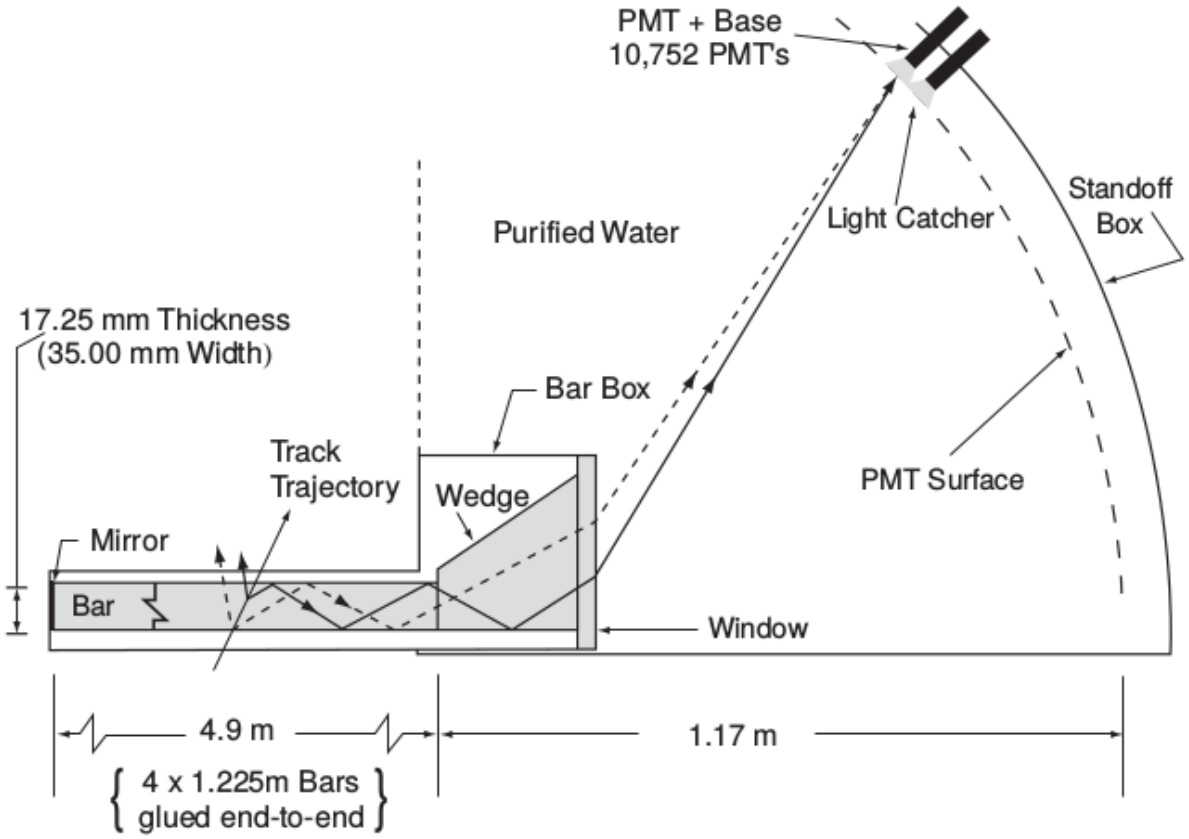

FIG. 11: Schematic of the BaBar DIRC and detection region [2].

12 summarizes the performance of the BaBar DIRC, showing excellent Cherenkov angle reconstruction (2.5 mrad, only 14% larger than the design goal of 2.2 mrad) and photon yield per track.

3.4.1 DIRCS IN FUTURE EXPERIMENTS

The BaBar DIRC has since inspired many other experiments/facilities, including the EIC, to utilize this new, novel PID system in a variety of ways (Figure 13). The Focusing DIRC (FDIRC) proposed for the now-cancelled SuperB collider in Italy was the first to propose using some form of focusing for the Cherenkov photons, allowing for a factor of 10 smaller expansion volume [19] [20]. The barrel DIRC for the PANDA experiment at FAIR in Germany will use shorter radiator bars for a more compact design [21], while the PANDA disc DIRC will be used in the forward region and will be the first disc DIRC to be used

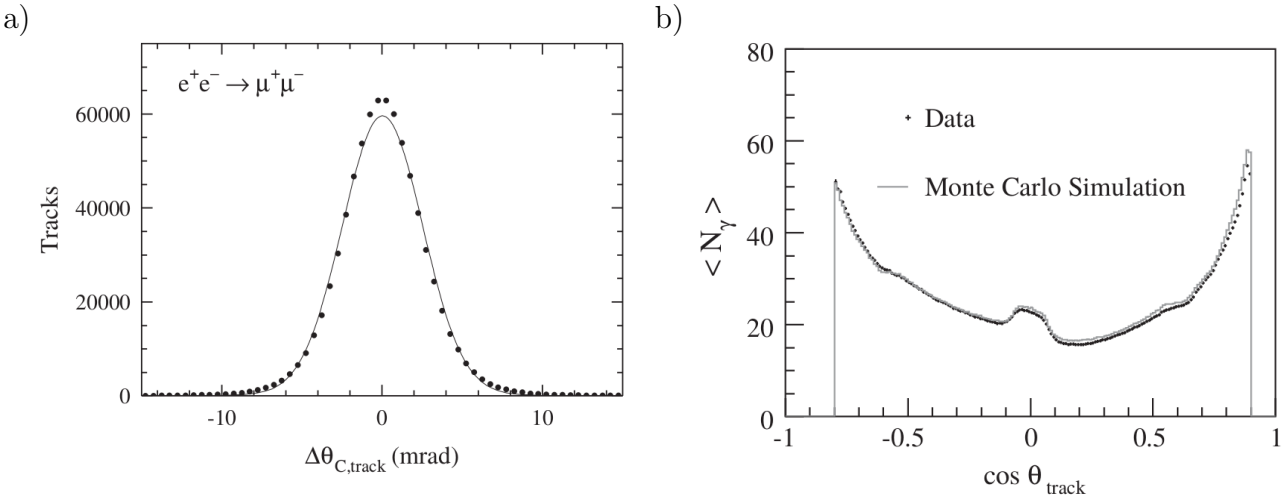

FIG. 12: Performance of the BaBar DIRC for $e^+e^- \to \mu^+\mu^-$ events [2]. a) shows the difference between the measured and expected Cherenkov angle (dots) and a Gaussian fit to the data with a 2.5 mrad width (line). b) is the average number of detected photons vs. track polar angle for data (dots) and GEANT4 [18] simulation (line).

in a high-performance 4π detector [22]. Belle II at the SuperKEKB accelerator in Japan will utilize wide plates as radiators and focus on fast timing for PID in the barrel region [23]. The TORCH detector, similar to the PANDA disc DIRC, will be a large-area detector focusing on precision time-of-flight to do PID for low momentum kaons at the upgraded LHCb experiment [24]. The GlueX experiment at JLab will be recycling four bar boxes from the BaBar experiment to cover the forward region of their spectrometer; utilizing focusing similar to the FDIRC design [25].

3.5 HIT PATTERNS AND PARTICLE SEPARATION METHODS

As mentioned previously, a DIRC detector is a compact RICH system that relies on internal reflection of the Cherenkov photons in the radiating material. However, as is illustrated in Figure 10, not all of the light produced inside the radiator is internally reflected, as photons with an angle less than the critical angle (approximately 43° for the interface from fused silica to air) with respect to the surface will escape the radiator. Because of this loss of photons the hit pattern of a DIRC is only roughly half of a typical RICH ring, which is then mirrored and folded in a complex way based on the shape of the expansion volume and where the photon exits the radiator. If the expansion volume is more radially compact the two ring segments become stacked side by side. To complicate matters further,

if the expansion volume is small enough that reflections from the sides occur then the ring segments are folded on top of themselves to create much more complicated hit patterns. Figure 14 illustrates this folding of the hit pattern due to expansion volume size. Figure 15 shows the contribution to the folded pattern from single reflections inside a prism shaped expansion volume.

Two approaches were used in the analysis presented in this thesis for particle species separation: reconstruction of the Cherenkov angle using a geometric reconstruction method similar to the one used by the BaBar DIRC, and time-based imaging using probability density functions (PDFs) [1] similar to that to be used by the Belle II imaging Time of Propagation (iTOP) counter.

3.5.1 CHERENKOV ANGLE RECONSTRUCTION

The emission angle between a single photon and the particle track can be reconstructed from the observed photon coordinates on the detector plane. The spatial position of the centers of the radiator bar and the struck pixel are known and used to define the 3-dimensional unit direction vector $\vec{k} = (k_x, k_y, k_z)$ pointing from the center of the bar end to the center of the pixel (shown in Figure 16). The k-vector is defined as the photon exit vector just inside the bar. The direction vector from the bar center to the pixel center along with Snell's law are used to determine the k-vector. Excluding aberrations, any photon reaching this pixel originated with the same direction vector at the end of the bar, regardless of the photon origination point. Together with the particle direction $\vec{p} = (p_x, p_y, p_z)$ the Cherenkov angle for each photon can be calculated from

$$\theta_C = \arccos\left(\frac{\vec{k}\cdot\vec{p}}{|p|}\right) \tag{7}$$

In order to assign a value of the k-vector for each pixel a photon gun is used in GEANT4 to illuminate the detector plane. Roughly 10^5 photons are created at the center of the bar near the bar/expansion volume interface uniformly in a solid angle of 1.3π steradians and allowed to propagate through the expansion volume and onto the photosensors. The initial value of the k-vector, the propagation time, number of bounces inside the expansion volume, and sensor and pixel number are all stored in a large table, called a lookup table (LUT). The values in the LUT are independent of particle species and momentum and only depends

[1] In this manuscript, 'PDF' refers to a 'probability distribution function' and does NOT refer to either an Adobe® Portable Document Format or to a parton distribution function.

upon the detector geometry (e.g. the focusing optic, or the location of the bar relative to the expansion volume). Because of this a LUT for a given geometry can be generated before taking data. Another advantage to the geometric reconstruction is that a full simulation of the particle track is not needed which saves a lot of computation, as much of the computing power used during a simulation is used for the photon propagation through the bar.

Unfortunately, the direction of the k-vector as reconstructed by the pixel does not uniquely define the directionality of $\vec{k}_{org}$. Because the number of reflections inside the bar cannot be known there are 8 possibilities, or ambiguities, for the original directionality of the photon that must be considered (forward/backward, up/down, and left/right). Figure 17 illustrates a 2D simplification of this problem, showing 4 possible photon directions propagating from the particle track. Here each of θ_{1-4} are possible values for the true Cherenkov angle. In the full 3D space this leads to up to 8 possibilities to be considered for the k-vector for each detected photon, and therefore up to 8 values of the Cherenkov angle θ_C.

In addition to ambiguities coming from guessing the initial directionality of the k-vector inside the bar there are also ambiguities coming from the multiple possible paths that a photon could take from the center of the bar to a pixel inside the expansion volume. Figure 19 shows a prism-shaped expansion volume, similar to that used in the analysis presented later in Chapter 6, showing the labeling of the surfaces and an example of ambiguous photon paths from the bar to a pixel on the detector plane.

The number of ambiguous paths that are reconstructed can be reduced by averaging the initial direction of all photons in the LUT that have the same number and types of reflections and land in the same pixel. For a simplified example, see Figure 18

The Cherenkov angle is not, however, only reconstructed for one photon, but for between 20 and 120 photons per particle track. For each photon at least one of these reconstructed θ_C values is correct, while the others contribute to a combinatorial background in a spectrum of the reconstructed angle, an example of which can be seen in Figure 20 for 7 GeV/c protons with a 125° polar angle and made with an averaged path LUT.

3.5.2 TIME-BASED IMAGING

The other method of particle species separation that can be used for a DIRC is time-based imaging or time-based reconstruction, similar to that used by the Belle II Time-Of-Propagation counter. To do time-based reconstruction one must first generate a PDF of the timing information of each detector pixel for each value of particle species, momentum, polar track angle, and detector geometry (e.g. lens and bar types), thus giving a 5-dimensional

function of the timing distribution of photon hits [21]. Currently these PDFs cannot be computed analytically, so they are constructed computationally by either taking actual test beam data, or running simulations with sufficient statistics such that each pixel that can have a hit with the configuration of interest has a large enough occupancy to produce a more or less smooth PDF.

To reconstruct a data or simulation file using these PDFs the photon arrival time for each pixel with a recorded hit is compared to the PDF for each particle species, and the time-based likelihood of that hit corresponding to a given particle species X is calculated as $L_X = \ln(h_X)$, where h is the value of the PDF for the given hit time. One can then do a pair-wise difference of these likelihood values (e.g. $L = L_p - L_\pi$) to build a log-likelihood distribution between two particle hypotheses and extract a separation power for particle identification. The separation power for time-based reconstruction between two particle species is given by the magnitude of the difference of the two log likelihood plots divided by the average sigma. An example of time-based reconstruction for a bar radiator with a prism expansion volume is shown in Figure 21 for pions and kaons in a plate radiator with a prism expansion volume. This method of particle separation is also very useful for plate-type radiators as the LUTs in the geometric reconstruction assume the photons come from the center of the bar, which is no longer a good assumption for wide plates.

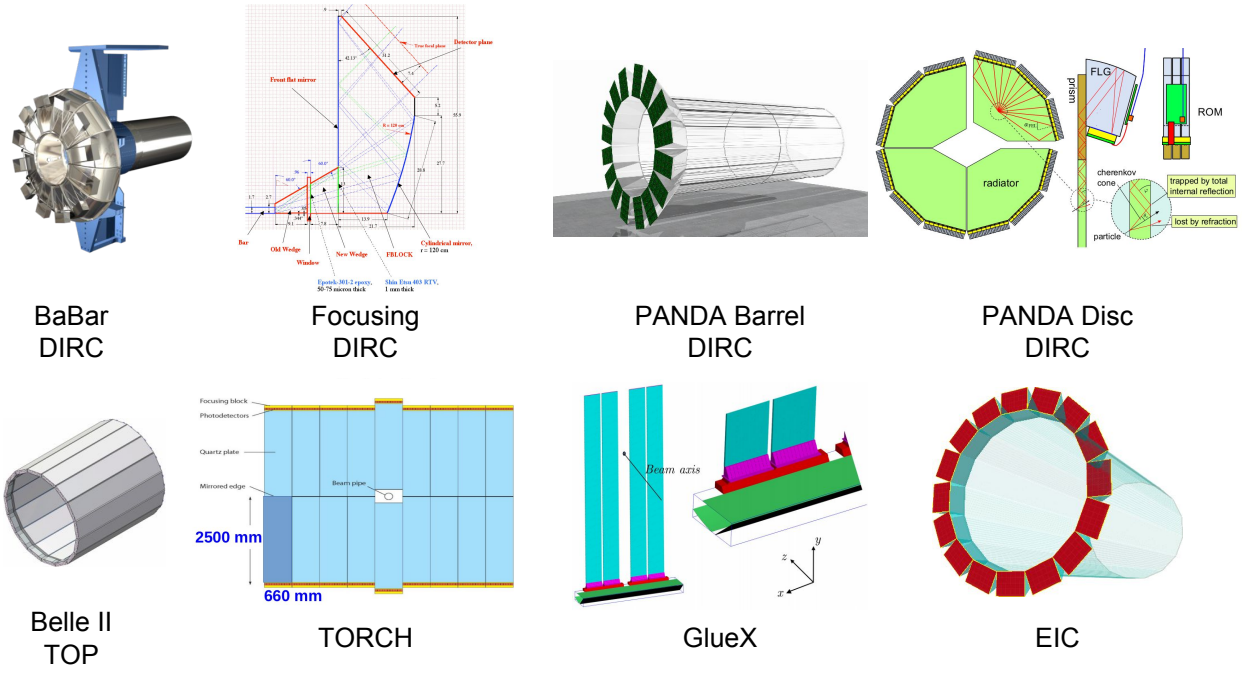

FIG. 13: Evolution of the DIRC concept. From top left to bottom right: BaBar Barrel DIRC [2], Focusing DIRC [20], PANDA Barrel DIRC [21], PANDA Disc DIRC [22], Belle II Time of Propagation DIRC [23], LHCb TORCH DIRC [24], GlueX DIRC [25], and the EIC DIRC.

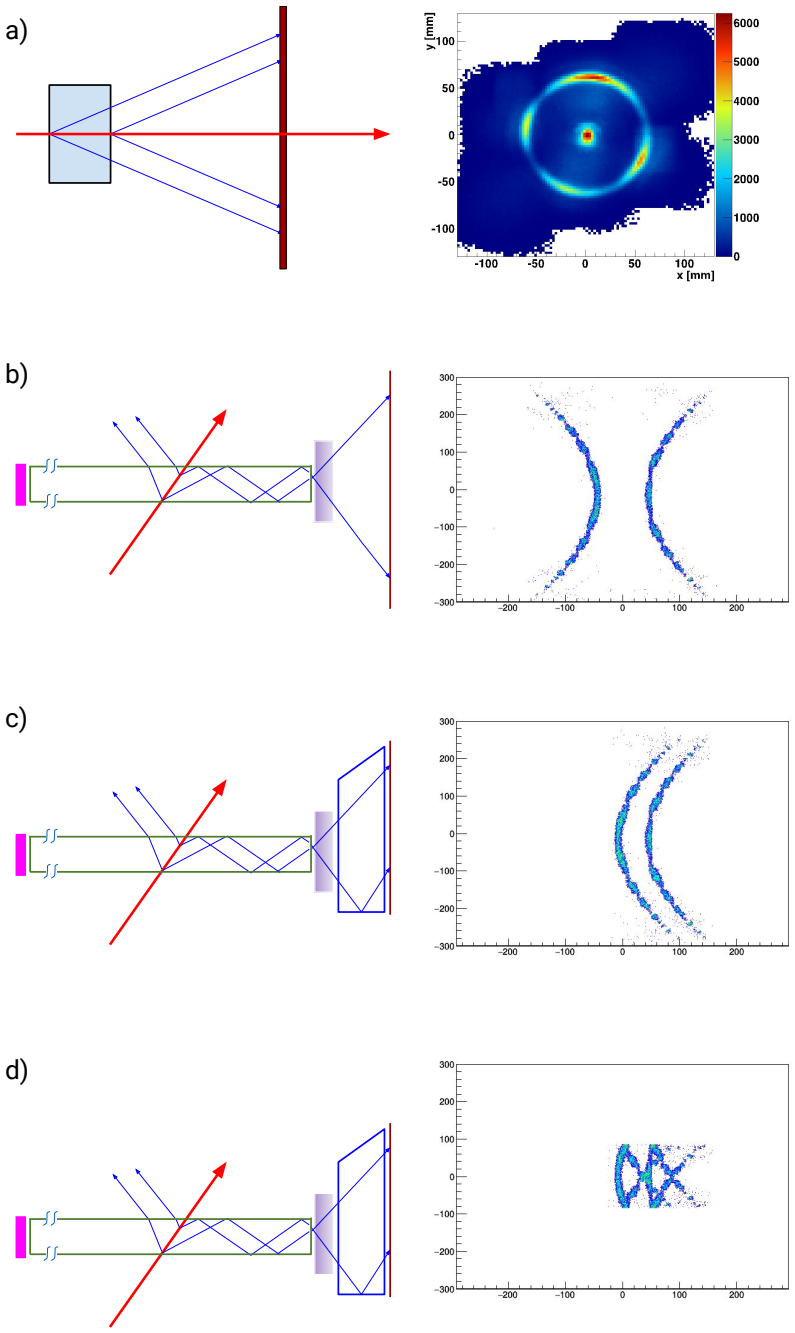

FIG. 14: Various detector geometries (left) and the resulting simulated hit patterns (right) from 1000 identical particles. A typical RICH detector (a), produces a very nice ring pattern. A DIRC detector with a sufficiently large expansion volume using a thin radiator bar (b) produces two ring segments. A DIRC with a radially compact expansion volume (c) will reflect one of the ring segments so that it will stack side by side. Finally, a DIRC detector with a compact expansion volume both radially and transversely (i.e. into and out of the page) (d) will cause the ring segments to fold in on themselves, making a fish-like pattern. The DIRC patterns are viewed from the back of the detector plane and rotated 90° clockwise relative to the corresponding geometry.

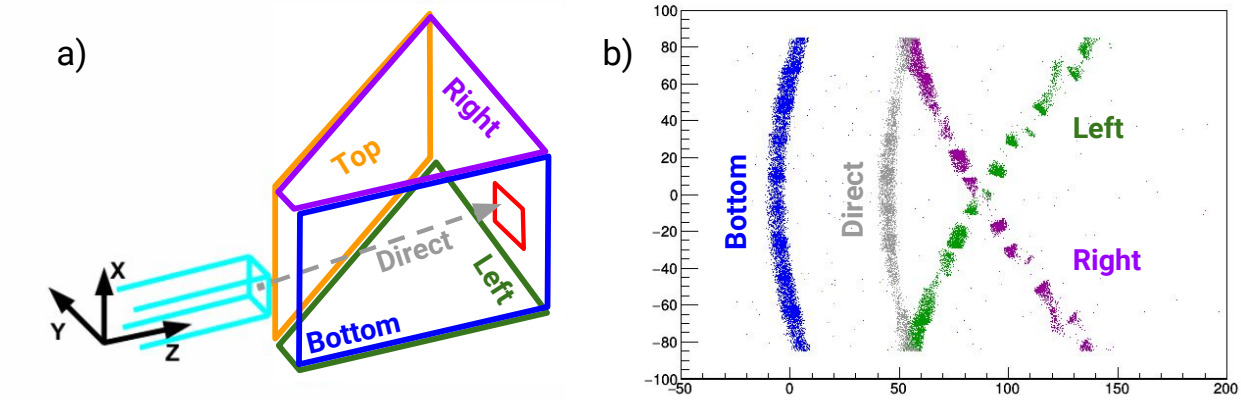

FIG. 15: For a prism-shaped expansion volume (a) [17], different segments of the hit pattern correspond to different paths taken (b). Paths with multiple reflections inside the prism (e.g. bottom-left) have been excluded for simplicity.

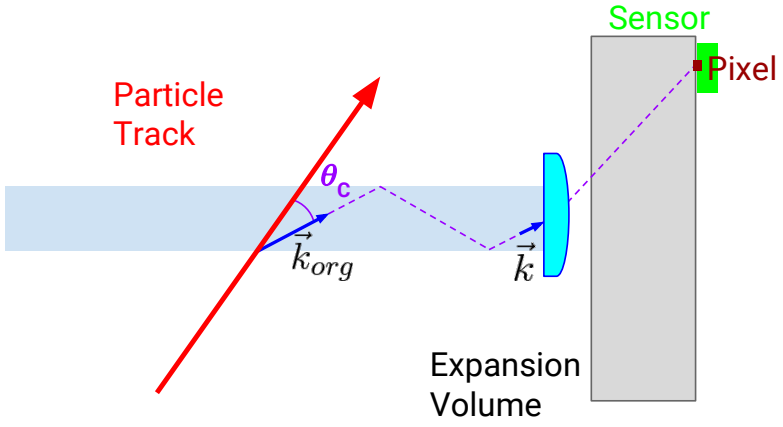

FIG. 16: Schematic of the geometric reconstruction concept, with a photon (purple) being emitted from the particle track. The direction of the k-vector can be used to determine the original direction vector, $\vec{k}_{org}$, of the photon and is used for the reconstruction of θ_C [17].

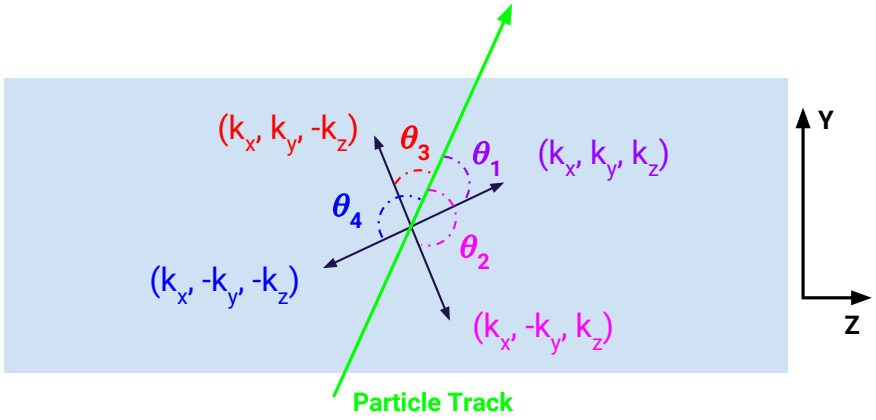

FIG. 17: 2D illustration showing all possible combinations of k-vector directions off of the particle track [17]. Not shown are the additional 4 components where $k_x \rightarrow -k_x$.

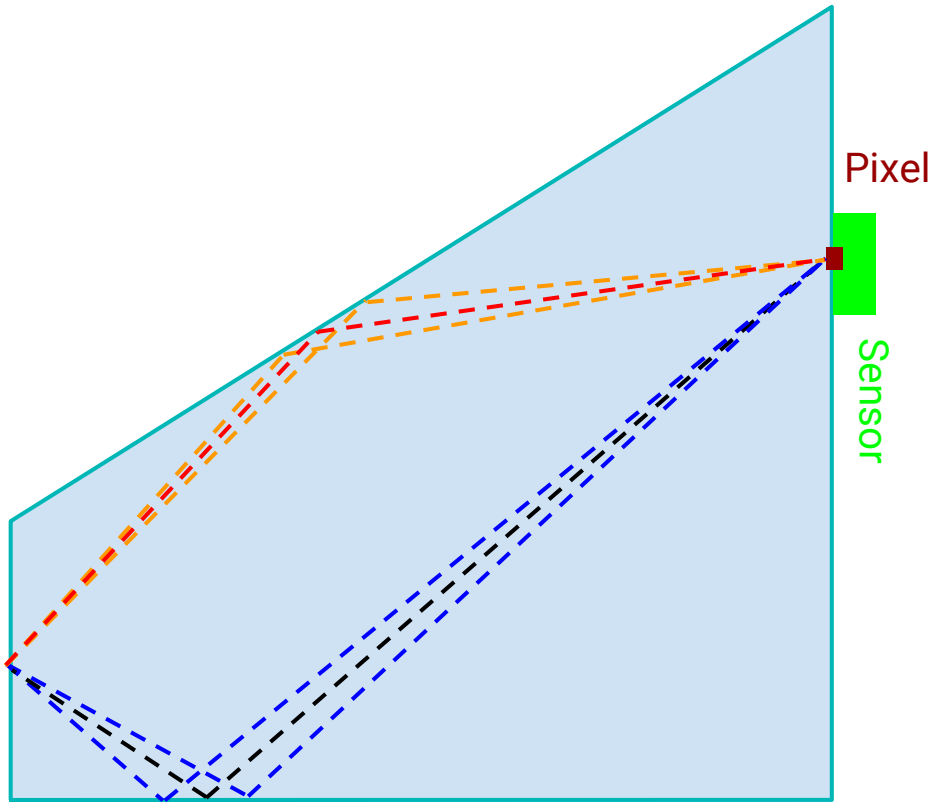

FIG. 18: A 2D example of averaging LUT entries to reduce prism ambiguity reconstructions. The two photons reflecting off of the bottom prism face (blue) have been averaged to the one black photon. The two photons reflecting off of the top prism face (orange) have been average to the red photon. In this simplified example the number of entries in the LUT have been reduced by half. Angles have been exaggerated.

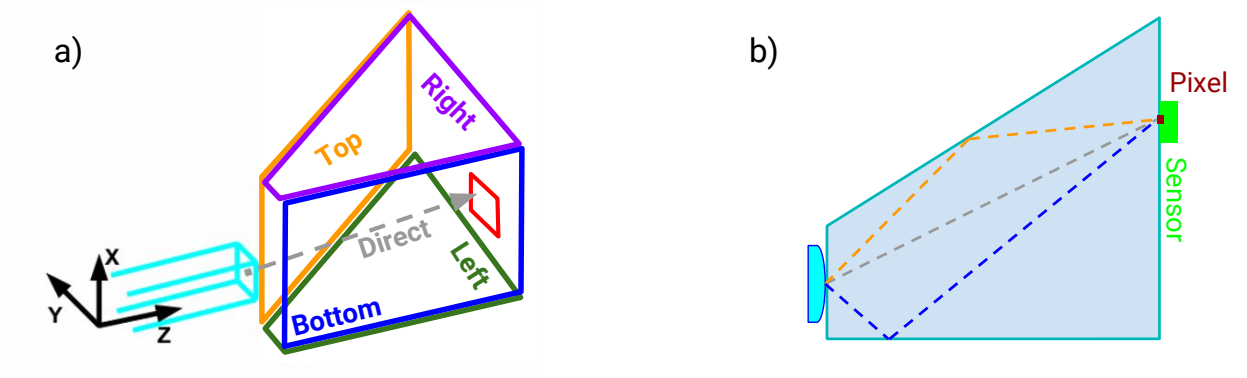

FIG. 19: Illustration of possible ambiguities in the θ_C reconstruction coming from possible paths in a prism-shaped expansion volume [17]. Each face is labeled in a) along with an example of a direct path, while b) shows 3 possible paths that lead from the bar to a certain pixel: 1 top reflection (gold), 1 bottom reflection (blue), and 1 direct path (gray).

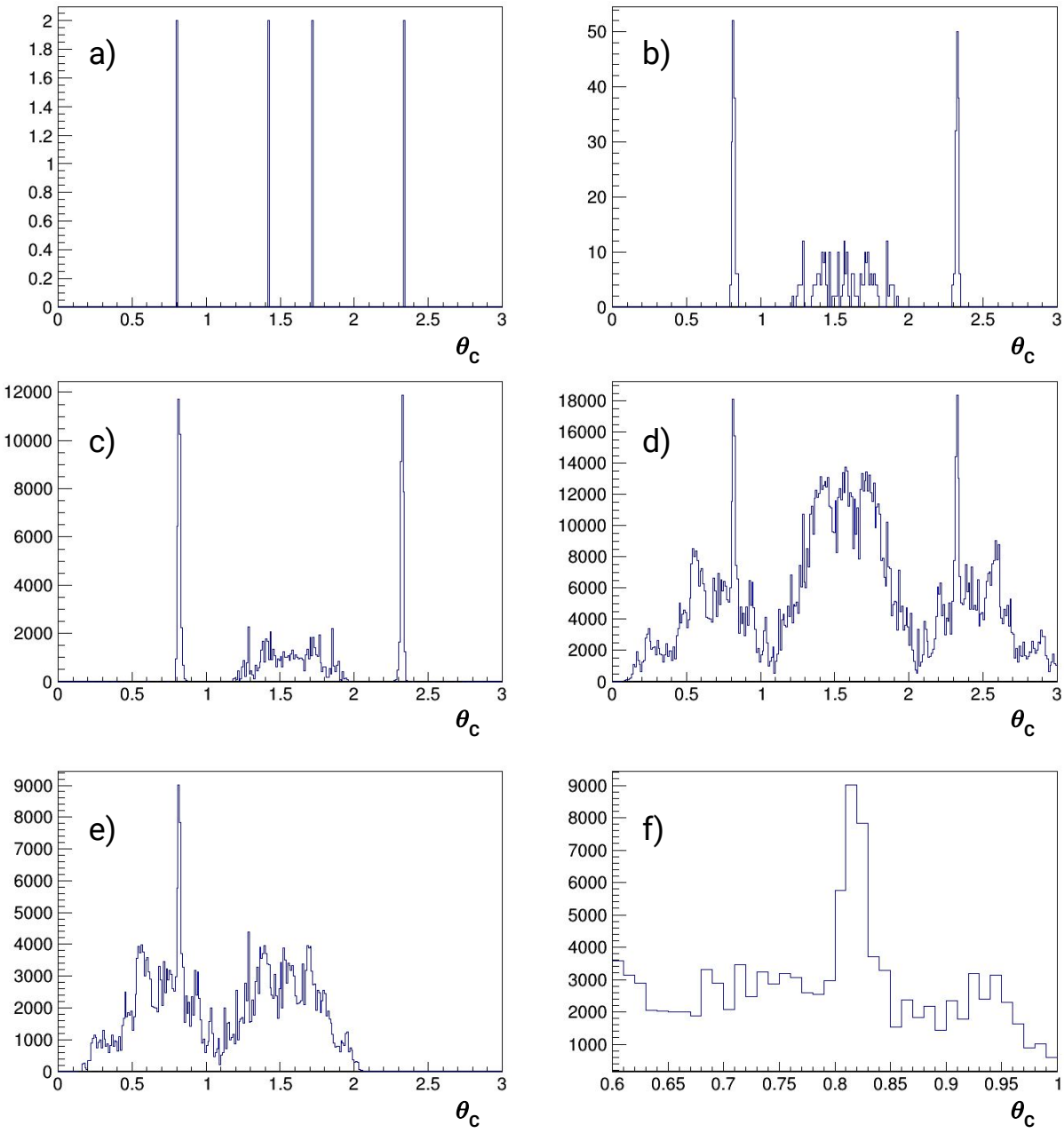

FIG. 20: Simulated reconstructed Cherenkov angle per photon from a 7 GeV/c particle with a polar angle of 125°. a) one photon from a proton with only bar ambiguities. b) all photons from one proton with only bar ambiguities. c) all photons from 1000 identical protons with only bar ambiguities. d) all photons from 1000 identical protons with both bar and prism ambiguities. e) same as d) but with constraints on the photon angle with the bar surface being greater than the critical angle for total internal reflections and neglecting y direction flips due to zero beam divergence. f) a zoom showing a buildup around the calculated value of 816 mrad along with a combinatorial background.

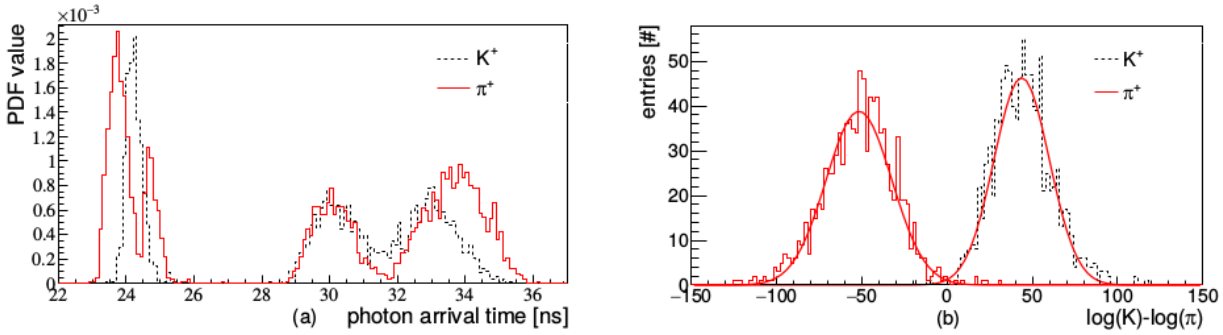

FIG. 21: An example of time-based reconstruction for a plate radiator with a prism expansion volume for kaons (dashed) and pions (solid red). Photon arrival times for one MCP-PMT pixel are shown in a), and b) is the log-likelihood difference for kaon and pion hypotheses for multiple 3.5 GeV/c particles at 22° polar angle [21].

CHAPTER 4

HIGH-PERFORMANCE DIRC@EIC

The BaBar DIRC was able to reach a performance of 3 standard deviations (s.d.) separation for pions and kaons at up to 4 GeV/c particle momentum. The PANDA Barrel DIRC wishes to achieve similar performance, but due to space constraints they will be using a smaller expansion volume and must therefore rely on optical focusing of the Cherenkov photons to reach this performance. In both cases the separation power requires a per track Cherenkov angle resolution (Eq. 6) of 2.5 mrad The physics goals of an EIC require a pion/kaon separation of 3 s.d. at up to 6 GeV/c momentum, which requires 1 mrad track Cherenkov angle resolution. The graph in Figure 22 shows pion-kaon separation as a function of particle momentum for different assumptions of the per track Cherenkov angle resolution, highlighting the achieved performance of BaBar and the desired performance of PANDA and EIC. In order to reach this high resolution in a compact space the EIC DIRC must incorporate cutting-edge technology in focusing optics and photo sensor granularity and timing resolution.

4.1 HIGH-PERFORMANCE DIRC COMPONENTS AND DESIGN

The baseline design of a DIRC for EIC has been constructed in a GEANT4 simulation based on that of the PANDA prototype DIRC, as shown in Figure 23. There are 16 modules, called bar boxes, each containing 11 radiator bars 4200 mm long with a cross section of 17×35.4 mm^2. The 16 bar boxes are arranged in a barrel with a radius of 1 m around the beam line. Mirrors are coupled to one end of each bar, and a special 3-layer lens, discussed in more detail later, is attached to the other end. The lens is then coupled directly to a prism-shaped expansion volume made of fused silica, the same material as the radiator bars. The prism has an opening angle of 38° with dimensions of $284.3 \times 390 \times 300$ mm^3. The 284.3×390 mm^2 detector plane of each prism is covered with micro-channel plate photomultiplier tubes (MCP-PMTs) with 27,690 2×2 mm^2 pixels, for a total of 443,040 channels across the entire detector to record the location and arrival time of each detected Cherenkov photon. The dependence of the performance on the granularity of the detectors is shown later in this chapter.

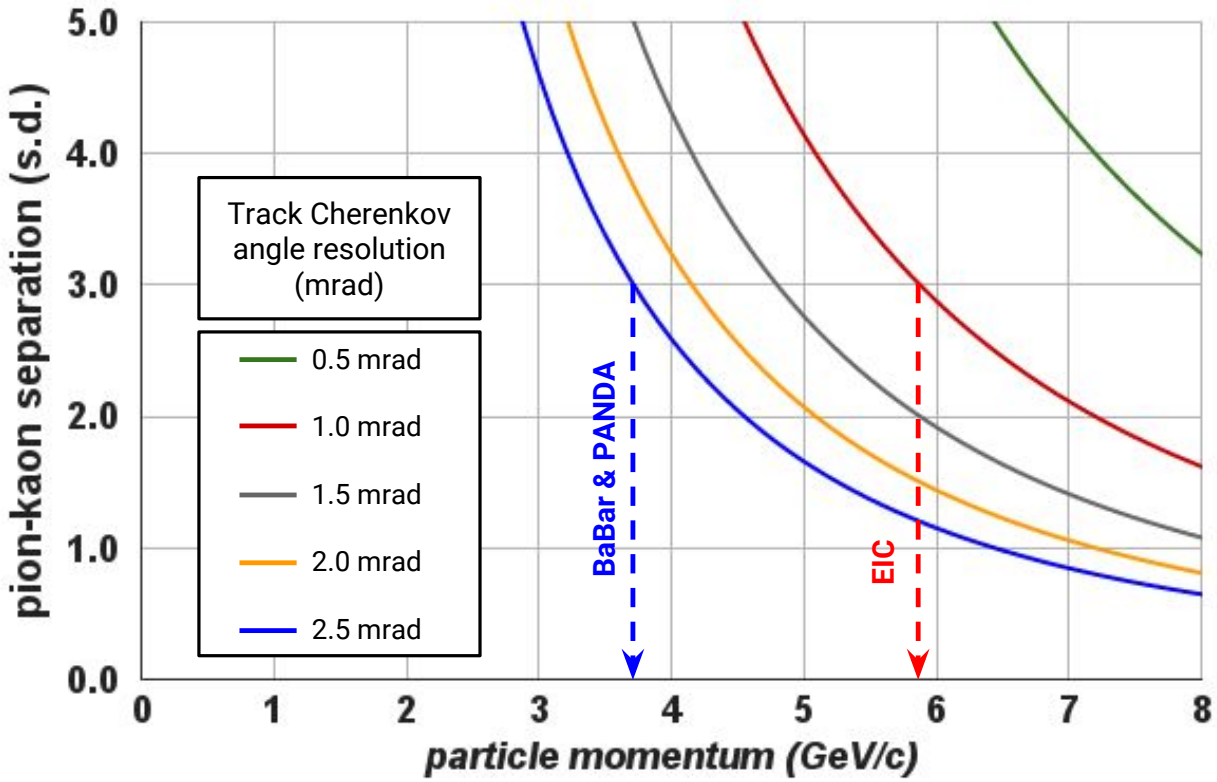

FIG. 22: Pion-kaon separation as a function of particle momentum for different assumptions of the per track Cherenkov angle resolution [26]. The PID requirements of the EIC necessitate a per track resolution of 1 mrad, while BaBar and PANDA needed only 2.5 mrad resolution.

4.1.1 FOCUSING OPTICS

The pixel and bar size of a DIRC detector are important contributions to the Cherenkov angle resolution for small expansion volumes. The influence of the bar size can, however, be offset by focusing the Cherenkov photons. The FDIRC R&D program first developed the concept of using focusing mirrors for DIRC detectors. The PANDA Barrel DIRC group settled on using a focusing lens between the radiator bar and the expansion volume. A standard lens made of fused silica with an air gap between the lens and the expansion volume was first studied. However, the focal plane of a single lens is highly parabolic in shape. Figure 24 shows that while an air gap lens provides good focusing of the Cherenkov pattern in the central region of the ring, where photons are more or less perpendicular to the lens, it becomes defocused nearer to the edges of the pattern and loses photons. This deterioration of the image quality for steeper angles is a combination of lens aberrations, the curved focal plane, and the so-called kaleidoscopic effect [27].

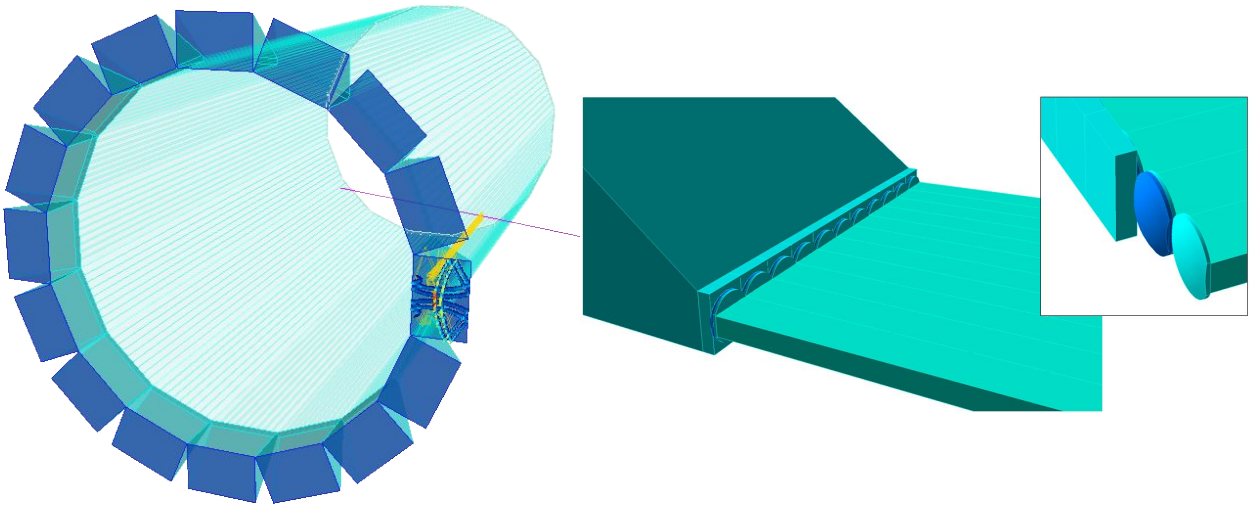

FIG. 23: A 3D view of the current DIRC at EIC baseline design. Left: the full GEANT4 simulation with 16 bar boxes, 176 radiator bars, a 3-layer lens focusing optic, and a 38° prism expansion volume. Right: a zoom in on a single bar box and the layering of the lens [26].

A 2-layer compound lens composed of fused silica and a layer of high-refractive index material Lanthanum crown glass (NLaK33) [28], $n \approx 1.75$, was also studied. This design couples directly to the expansion volume, greatly reducing the loss of photons at steeper angles. Figure 25 shows a comparison of the photon yield from a bar radiator with no focusing (green), a standard air gap lens (red), and a 2-layer lens (blue) for two cases. In the 125° case (left) both lenses have comparable photon yields, because the angle between the photons and the lens is fairly shallow. In the 90° case (right), however, the photon yield for the air gap lens is dramatically lowered due to the steep angles between the photons and the lens. The photon yield for the no focusing option is quite deceiving in that it produces a much higher average photon yield than either lens, but the reconstruction of the Cherenkov angle is nearly impossible to within a reasonable measure for the perpendicular case.

The 2-layer lens design solves the problem of photon yield loss from the air gap lens at steeper angles and will allow the PANDA Barrel DIRC to reach their desired separation power. However, as discussed earlier, this separation power of 3 s.d. at 4 GeV/c is insufficient for the requirements of a DIRC at EIC. The key to solving this problem was in designing a special 3-layer spherical compound lens. The advantage of this 3-layer lens design over a traditional optical lens or the 2-layer lens is the shape of the focal plane. According to simulation the focal plane of the 3-layer lens is relatively flat, as shown in Figure 26. Photos

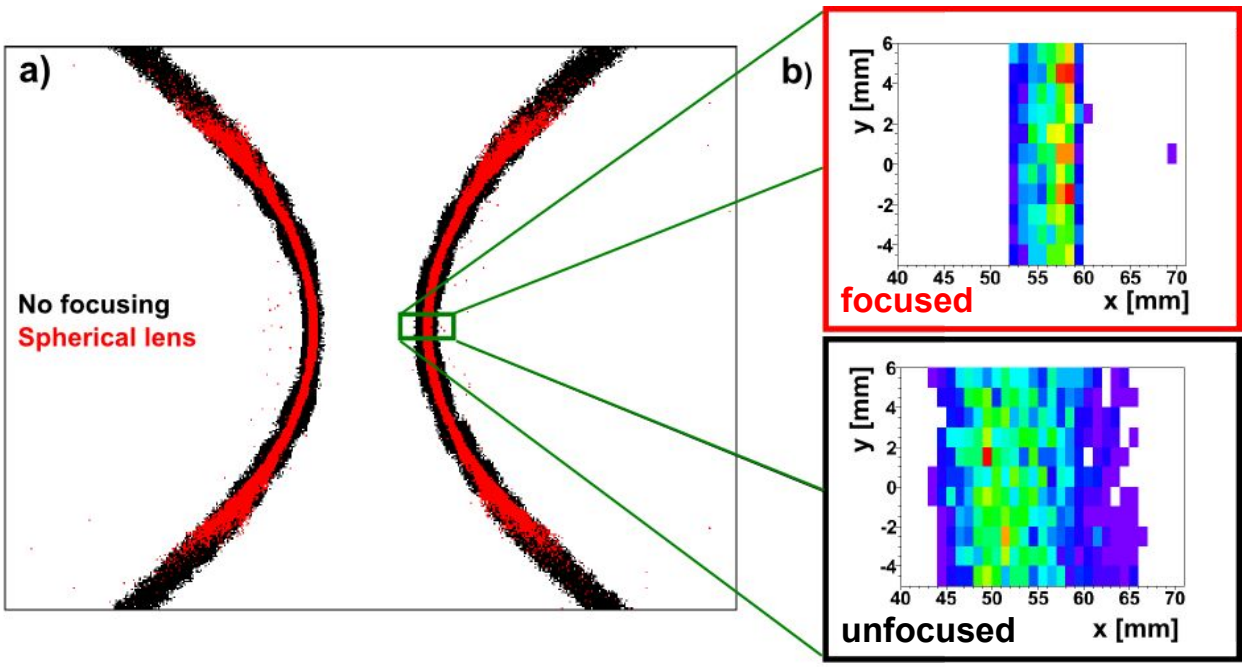

FIG. 24: Simulated hit pattern of PANDA DIRC without (black) and with (red) air gap lens focusing (a) [17]. On the outer edges of the ring image the lens is becoming dispersive and losing photons, while near the center of the rings the lens does a good job of focusing the image, as seen more clearly in b).

of a prototype lens tested at CERN in 2015 and an exploded view of the lens layers and dimensions are shown in Figure 27. It contains a layer of NLaK33 sandwiched between two layers of fused silica. The two radii of the middle layer were optimized to remove aberrations present in standard lenses by first defocusing and then refocusing transmitted photons to create a flat focal plane, matching the geometry of the prism expansion volume. Five prototype lenses were produced for evaluating the performance of the lens design in a test beam, for measuring the radiation hardness of the NLaK33 material, and for evaluating the focal plane. These tests will be discussed in greater detail in Chapters 5 and 6.

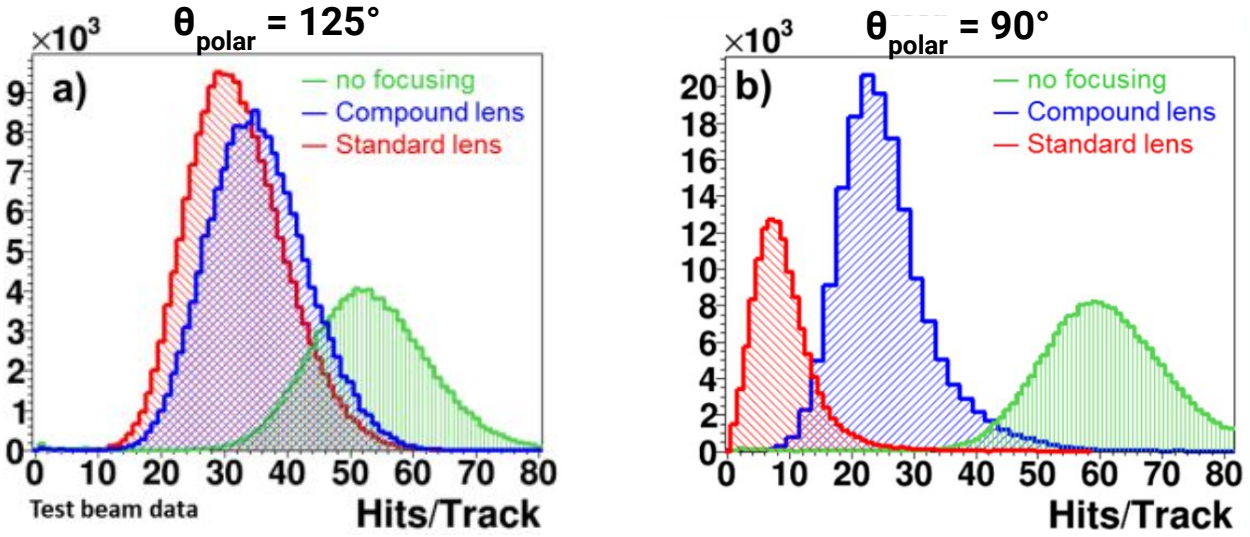

FIG. 25: Comparison of the photon yield per track for a DIRC bar with no focusing (green), a standard air gap lens (red), and a 2-layer compound lens (blue) for polar angles of 125° (left) and 90° (right) [17]. The standard and compound lenses have comparable yields at 125°, but the standard lens clearly loses a large amount of photons in the perpendicular case.

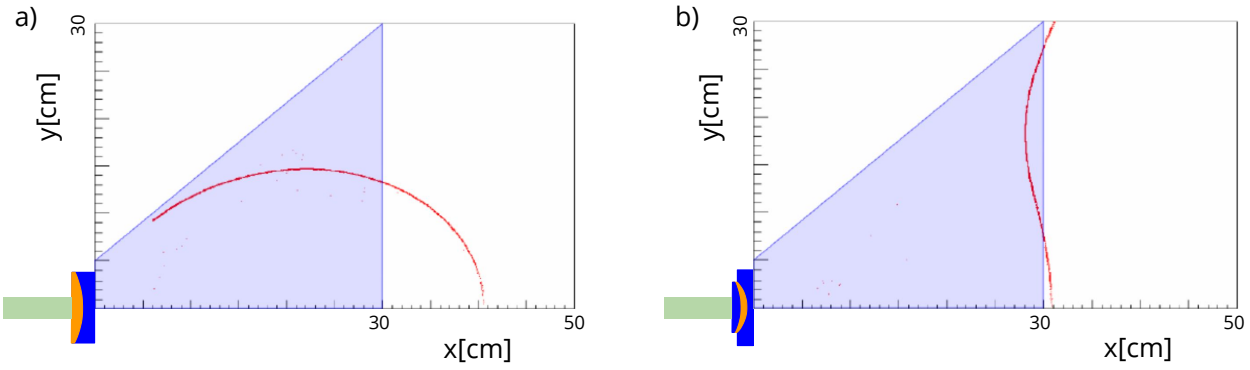

FIG. 26: The simulated focal planes (red lines) of a 2-layer lens (left) and the 3-layer lens (right) compared to the shape of the expansion volume prism (grey) [17]. Obviously the focal plane of the 2-layer lens is highly parabolic in shape, whereas the 3-layer lens focal plane is relatively flat, allowing for a better resolution of the Cherenkov angle.

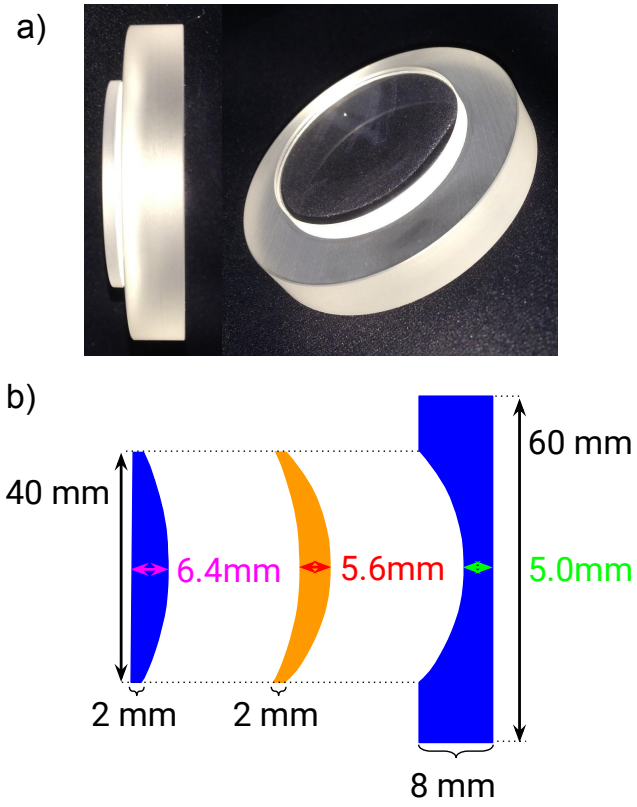

FIG. 27: Prototype 3-layer lens built for optical testing (a), and an exploded view of each layer with dimensions (b) [29].

4.2 SIMULATED PERFORMANCE

4.2.1 GEOMETRIC RECONSTRUCTION

Simulated reconstructions of the Cherenkov angle for kaons and pions at 6 GeV/c with a 125° polar angle using the design parameters above are shown in Figure 28. The signal is very clean and the mean and SPR of the distribution are easily extracted. Figure 29a shows the photon yield, or multiplicity, per polar angle for fifty 6 GeV/c pions, and Figure 29b shows the Single Photon Resolution (SPR) [1] per polar angle for fifty 6 GeV/c kaons (red) and pions (blue). The per track Cherenkov angle resolution, given by Eq. (6), is shown in Figure 30 for assumptions of 0.25 mrad (black), 0.5 mrad (red), 0.75 (green), and 1 mrad (blue) correlated term contributions with 6 GeV/c pions [2]. The simulations were done assuming that the sides of the 3-layer lens focusing optic were not reflective, therefore reducing the photon yield and making the performance slightly worse.

The SPR of the reconstructed Cherenkov angle was found to scale with the pixel size of the MCP-PMTs roughly as $SPR \approx SPR_0\sqrt{1 + size^2/a^2}$, as shown in Figure 31. Clearly the 4 mm pixel size, though not ideal, is comparable in performance to the 2 mm pixel size. This is an important factor to consider in the final design due to the increase of the cost per pixel of MCP-PMTs and with the electronics readout per channel as the size of the pixels decreases.

4.2.2 TIME-BASED RECONSTRUCTION

The methods for time-based reconstruction, as described in Chapter 3, were also implemented for the EIC DIRC: 60,000 pions and kaons were simulated in GEANT4 using the current EIC DIRC design geometry and PDFs were generated for each detector pixel; the PDFs were then used to produce log-likelihood separation for each particle hypothesis. Figure 32 shows the log-likelihood separation for pions and kaons at polar angle of 30°. Figure 33 shows the separation power (top) and the PID efficiency/mis-identification over all polar angles.

Overall the results for both geometric and time-based reconstruction show that due to

[1] Three points are normally required to define a circle and thus extract a radius. However, with a perfect RICH detector it is sufficient to know only a single point on the ring as one also knows the center of the circle (i.e. the particle track). Here, too, it is sensible to talk about the resolution of single photon events as the center of the "circle" for a DIRC (i.e. the polar angle) is known from tracking.

[2] NB: the per track Cherenkov angle resolution will be slightly different for each particle species, however, because the SPR for each particle is almost identical, showing only the results for pions is sufficient.

the design's large expansion volume, small pixel size, and ease of signal reconstruction the performance of this design can reach the desired performance for the required physics.

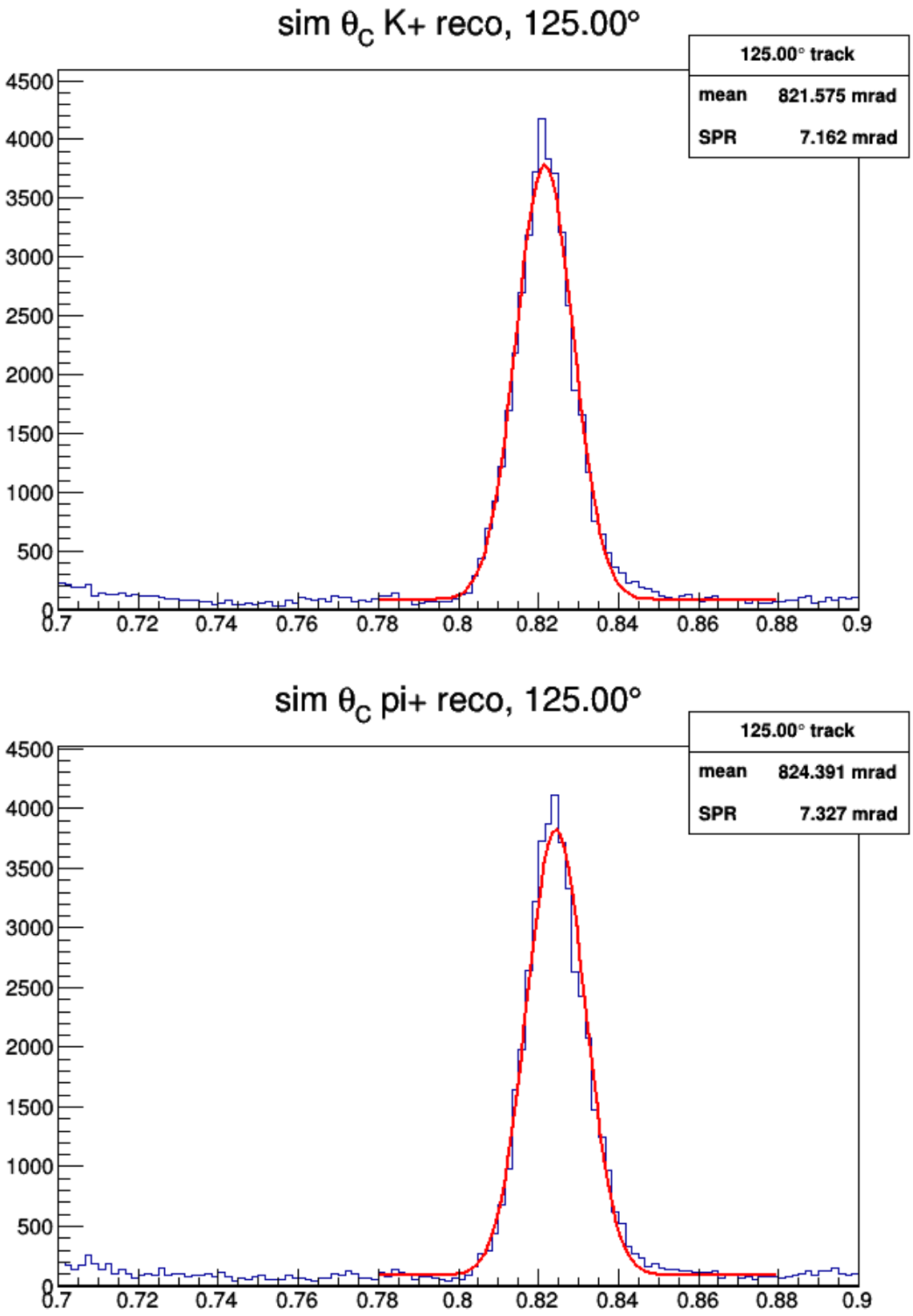

FIG. 28: Reconstructed θ_C spectrum for 6 GeV/c kaons (top) and pions (bottom) and a 125° polar angle.

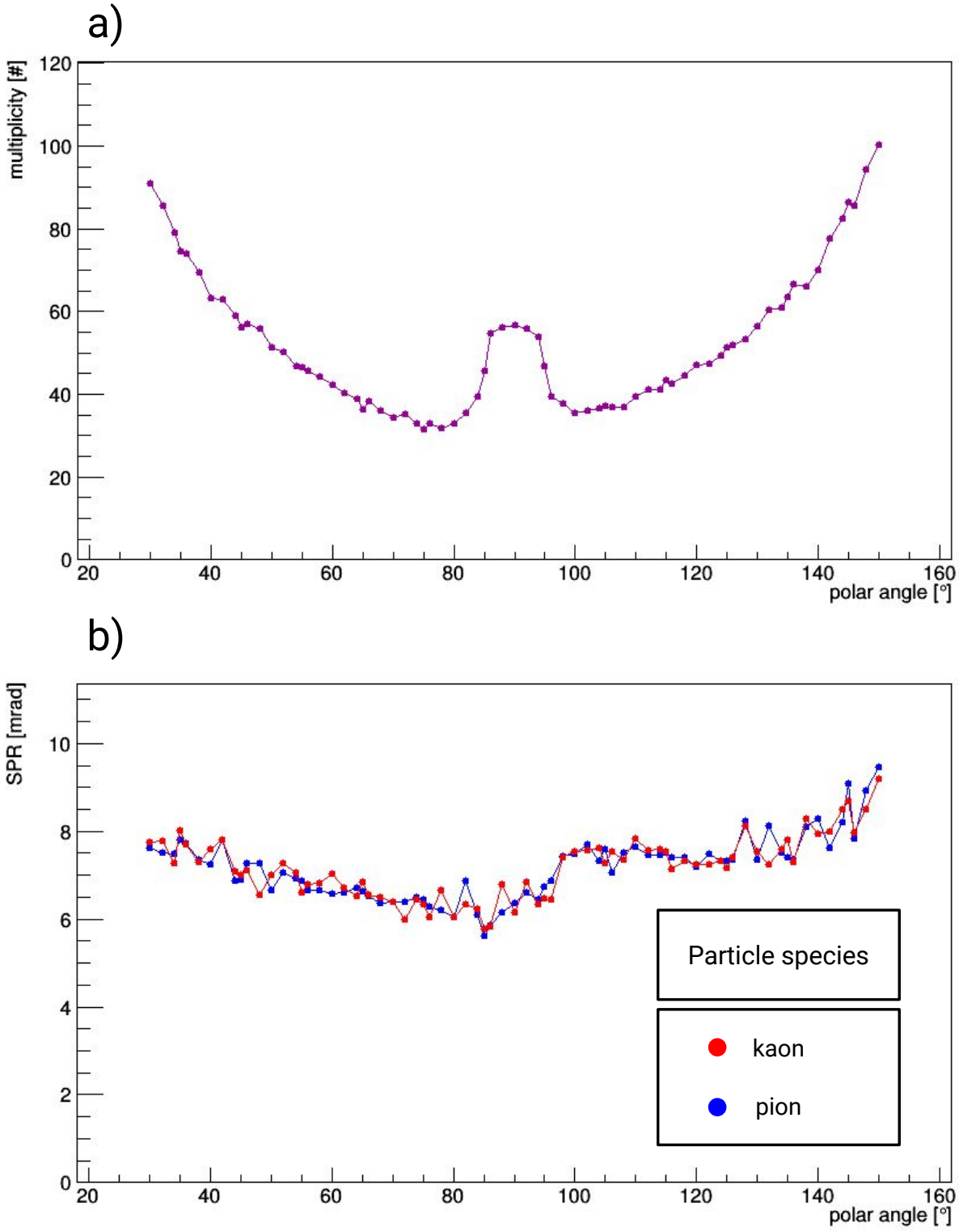

FIG. 29: The multiplicity (a) and SPR (b) performance per polar angle of the EIC DIRC baseline design. Plots were generated using fifty particles (kaons in red, pions in blue) at 6 GeV/c per polar angle.

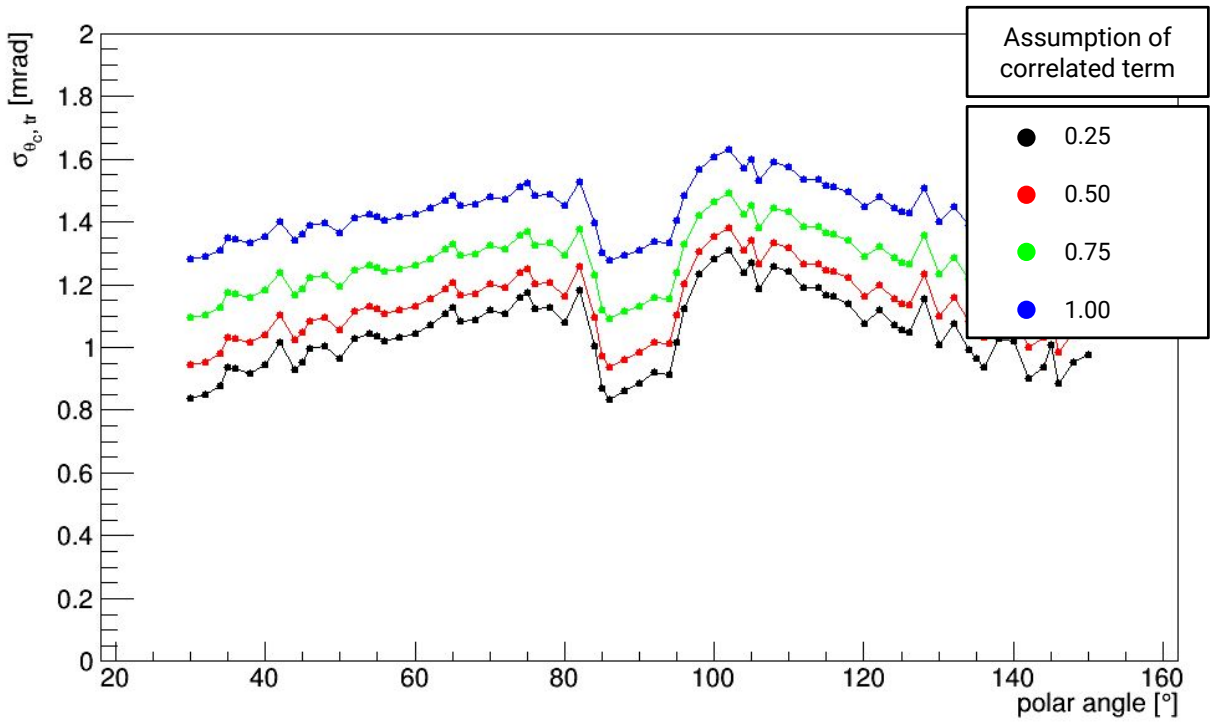

FIG. 30: The per track Cherenkov angle resolution of the EIC DIRC with different assumptions of the correlated term, $\sigma_{correlated}$: 0.25 mrad (black), 0.5 mrad (red), 0.75 (green), and 1 mrad (blue).

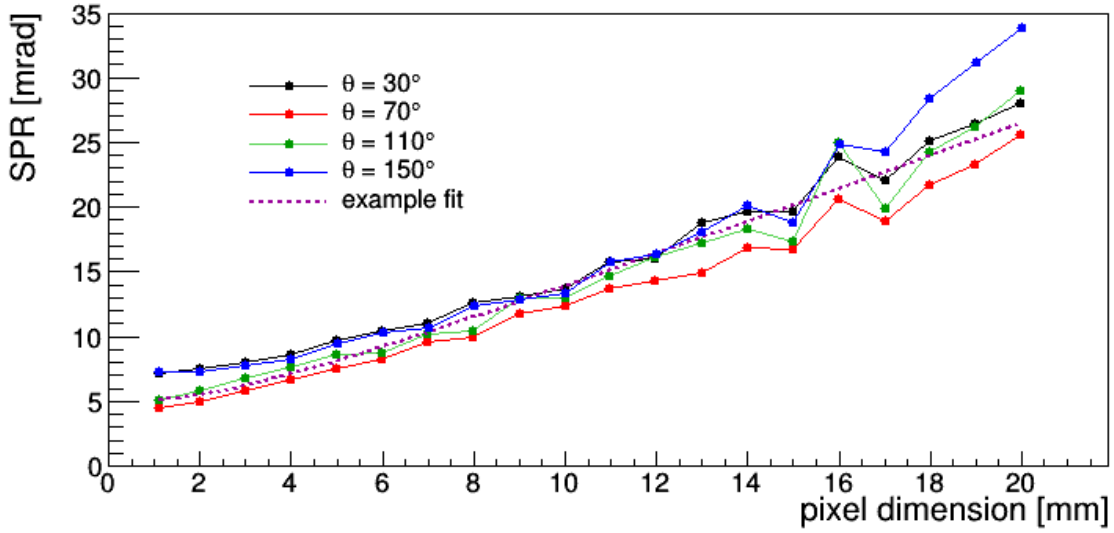

FIG. 31: Scaling of the SPR as a function of the MCP-PMT pixel dimension. Shown are 30° (black), 70° (red), 110° (green), and 150° (blue) polar angles along with an example fit (dashed purple) showing that the dependence of the performance scales roughly as $\sqrt{1+\frac{pixel^2}{a^2}}$.

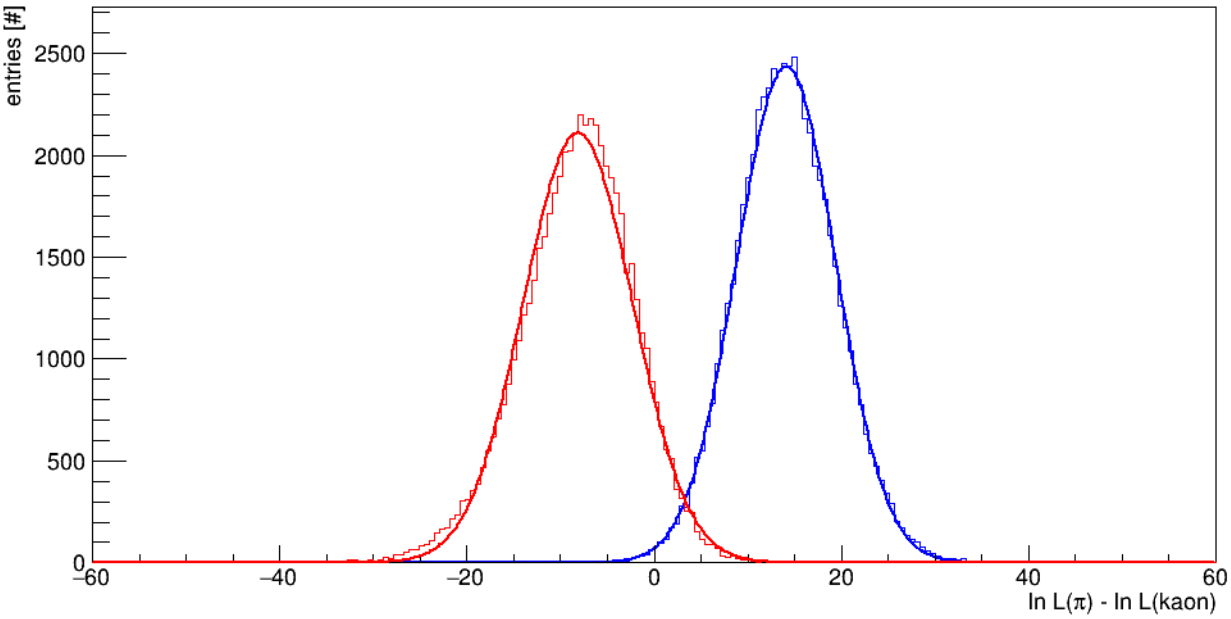

FIG. 32: Example of log-likelihood separation for pions (red) and kaons (blue) at 30° polar angle using time-based reconstruction.

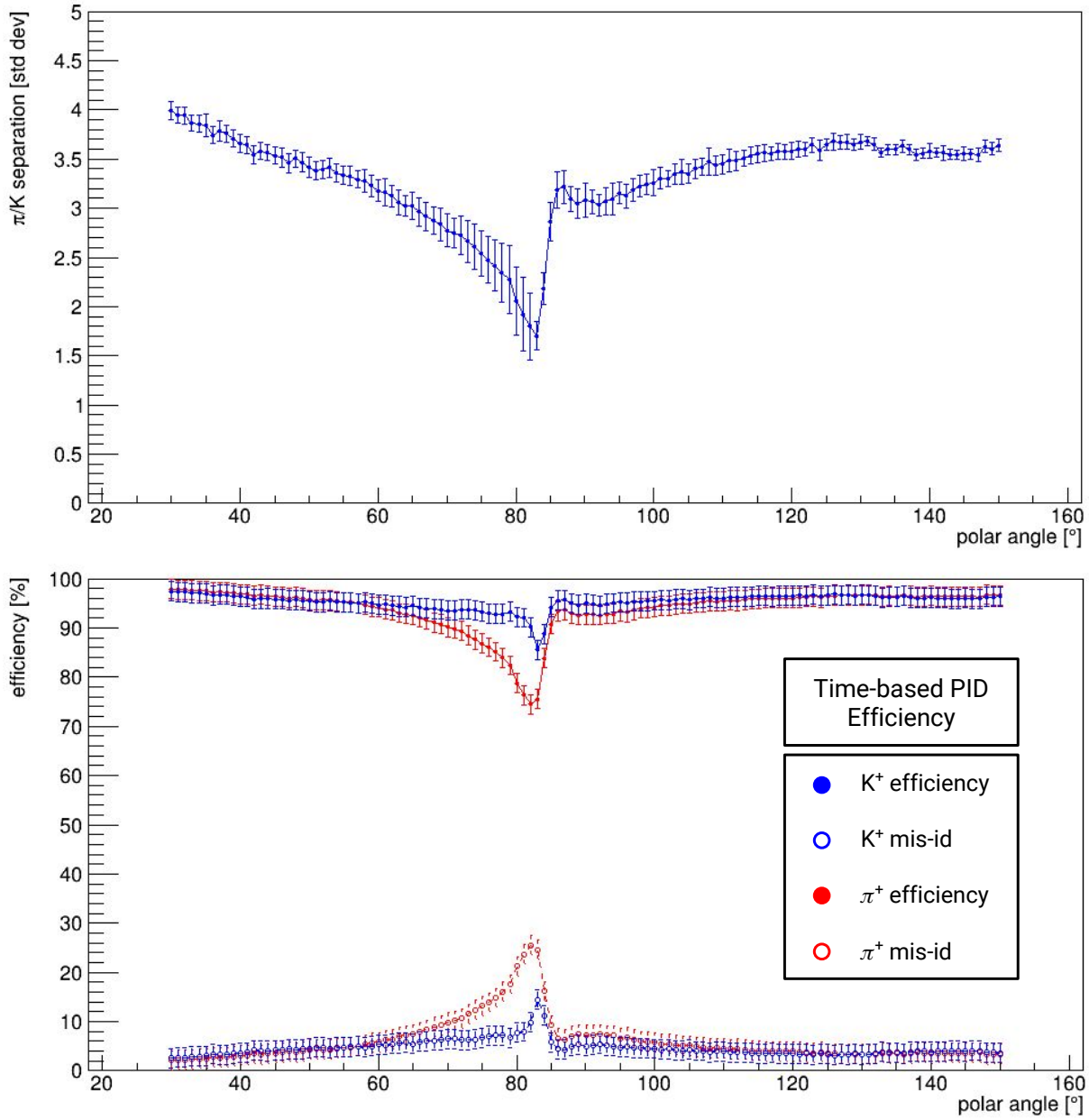

FIG. 33: Simulated performance of the DIRC at EIC baseline design. Top: Separation power as a function of polar angle for 6 GeV/c pions and kaons using time-based reconstruction. Bottom: Efficiency (solid circles) of PID as a function of polar angle for pions (red) and kaons (blue) along with the mis-identification rate (open circles).

CHAPTER 5

TESTING DIRC COMPONENTS

The validation of the key components of the DIRC for an EIC discussed in Chapter 4 is vital to show that the GEANT4 simulation package produces results expected for the real detector. However, due to budget restraints it was not possible to build or otherwise procure a full scale prototype of the envisioned EIC DIRC discussed in Chapter 4. As a conservative estimate of the cost of a simple prototype: one radiator bar is $20k, a prism expansion volume is $30k, a 3-layer lens is $10k, and an array of 24 (4x6) sensors is $200k. On top of this, the cost of a test beam run would be roughly $10k for travel and expenses. This roughly $300k expense for one prototype and test beam is highly impractical given that the budget for all detector work for the EIC R&D effort (RICH, Time-of-Flight, simulation studies, calorimetry, etc) is only $1M/year[1]. Instead a series of test bench measurements have been made to validate simulated performance of the new 3-layer lens design, study the radiation hardness of the NLaK33 material, and evaluate the performance of MCP-PMTs in high magnetic field environments. A synergistic test beam effort with the PANDA Barrel DIRC group was also performed at CERN in 2015, but will be discussed in greater detail in Chapter 6.

5.1 OPTICAL PROPERTIES OF 3-LAYER LENS

The purpose of the 3-layer lens design is to provide a mostly flat, uniform focal plane to follow the face of the detector plane. Doing so provides better resolution and hence better performance compared to standard focusing options, which typically have very curved, hyperbolic focal planes. A GEANT4 simulation of the nominal (top) and full 3D focal plane (bottom) of the lens are shown in Figure 34. The 3D plane has been limited to the size of the detector plane anticipated for the EIC DIRC, and the color scale indicates the angle at which photons intersected the front face of the lens. Because only the total focal length is of interest the depth of the expansion volume was limited so that no bounces occurred.

[1]It should be noted that once the Department of Energy approves the construction of an EIC, but before breaking ground on the facility, the budget for R&D will be expanded such that building a baseline-design EIC DIRC prototype will be viable

To measure the shape of the focal plane a setup was designed and built, shown in Figure 35, at Old Dominion University in which a laser shines through a 50/50 beam splitter and a mirror to make two parallel beams. Initially the beams were separated by 5 mm, but gradually the distance was reduced to 1 mm in order to attempt to avoid non-uniform aberrations due to small misalignments as much as possible. The beams then pass through a $30 \times 40 \times 60$ cm^3 glass container filled with Britol 9NF White Mineral Oil [30] with a refractive index similar to that of fused silica to simulate the behavior of light passing from bar to lens to expansion volume. The beams are focused through the 3-layer lens prototype, being held in a specially designed holder that allows the lens to be rotated in two planes (Figure 36). Finally the beams are focused onto a plastic screen inside the tank that is attached to a track and allowed to slide freely. Due to the relatively low resolution of the human eye and the finite size of the beams the exact point of focus was difficult to measure, so an averaging method was used in which the median of the two points where the beams seem to converge and diverge was taken to be the focal point (see Figure 40). This lead to much more accurate and reproducible results.

Measurements were initially taken with a 632 nm red helium-neon laser, but the beam spot was too large and very distorted. A 530 nm wavelength green laser with a 1 mm beam spot was then purchased as a replacement. Initial results with a 5 mm beam separation are shown in Figure 37. Obviously there is a large discrepancy in both position and shape of the measured and simulated focal plane. This was rectified by discovering that in the simulation it was assumed that the two beams were entering the lens at fixed points on the lens' face regardless of lens rotation, where as in the experiment the rotation of the lens about it's center causes the beams to shift with respect to the lens face. When rotating at the edge of the lens closest to the laser rather than through the center this difference is negligible, as illustrated in Figure 38.

A correction was implemented in the GEANT4 simulation to account for the shift of the beam spot during rotation, the results of which can be seen in Figure 39a. The beams have since been brought to a 2 mm separation to reduce effects of aberration and a second lens holder was 3D printed to allow for rotation about the edge of the lens. A new round of data was taken and results are shown in Figure 39b. This change vastly improved the results of both the simulation from the first measurement and the results of the second, showing that the simulation indeed reproduces very nicely the shape of the focal plane, although the position is still roughly 3 cm too long.

The absolute position of the focal plane can be explained in several ways: the second

curved surface of the 3-layer lens has a slightly smaller radius than was requested, the NLaK33 material has a slightly larger index of refraction than anticipated, the NLaK33 layer is slightly thicker than was requested, the laser beams in the experimental setup are not parallel, the index of refraction of the mineral oil is not equivalent to that of fused silica, or some small contribution from any and all of these effects. Unfortunately, measuring these quantities is currently not achievable. However, the GEANT4 simulation can manipulate them with high precision to study their effects on the focal plane.

Figure 41 shows by how much each of these parameters must be adjusted such that the point with 0° rotation and tilt angles agrees with the same point measured in the lab, along with the "perfect" simulation, which assumes all default parameters are correct, for comparison. A decrease in the index of refraction of the mineral oil of 0.15 (pink) is unrealistic due to the drastic change in the focal plane. Likewise, an increase in the index of refraction of the lanthanum crown glass by 0.03 (green) is not realistic due to the large difference between needed value for the simulation and the specifications sheet. A decrease in the radius of the second layer of the lens by 1.3 mm (blue), and a convergent angle of 0.15 mrad between the beams (black) do, however, seem reasonable in describing this systematic shift of the focal plane.

As it is impossible to measure the curvature of the second layer of the lens and detecting these small deviations from parallel in the beams, a second test was done to study the effects of the aberrations that occur when going through the lens off-center. A shift of 7 mm along the direction of a line between the two beams was made with the oil tank in the ODU setup and several measurements were taken. The same shift was implemented in the simulation for both the decreased second layer radius and non-parallel beam scenarios. Results of this off-center shift are shown in Figure 42. Clearly the modification of the radius corrects too much for the aberrations closer to the edge of the lens, while the assumption of non-parallelism gives a near-perfect description of the taken data.

After this systematic shift has been accounted for, both the shape and position of the focal plane agree very nicely between data and simulation, thus giving a good indication that the simulation for the EIC DIRC will yield reasonable results with the current simulation software. The prototype lens that was produced is not the finalized version of the lens to be used in the EIC, however, as the radii of the two curved surfaces must be optimized for the EIC design. There has also been discussion of building cylindrical 3-layer lens as a cost-saving measure without sacrificing on performance. Such a lens is currently planned for being included in a 2017 CERN test beam with the PANDA Barrel DIRC group.

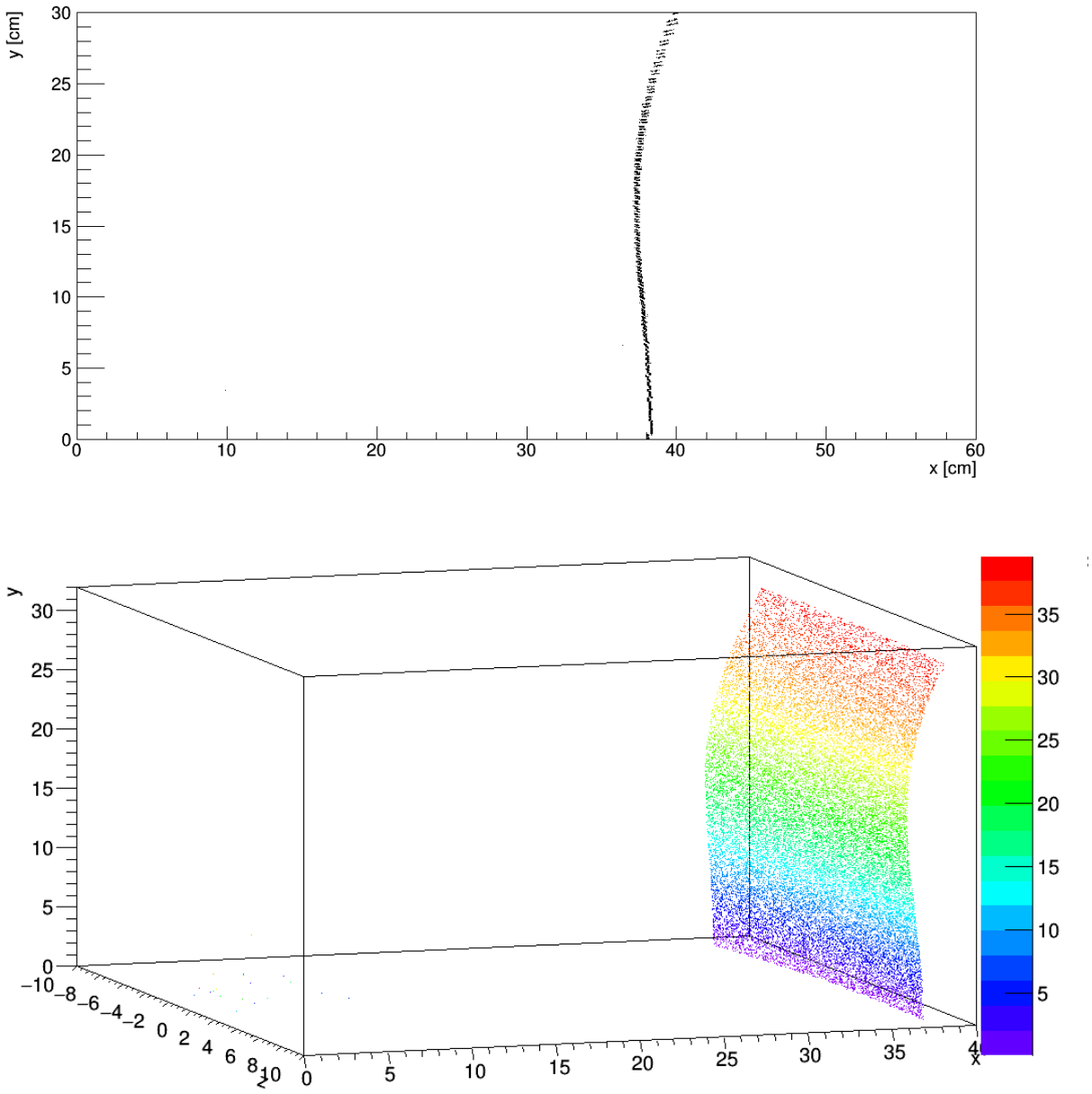

FIG. 34: Simulation of the 3-layer lens focal plane with all photons confined to a single plane (top) and the full 3D focal plane (bottom). The color scale corresponds to the initial angle (in degrees) between the laser beams and the lens face. The 3D plane has been constrained to the y/z dimensions of the current expansion volume for the EIC DIRC. The "beams" of photons in the simulation were centered around the center of the lens with a separation of 2 mm.

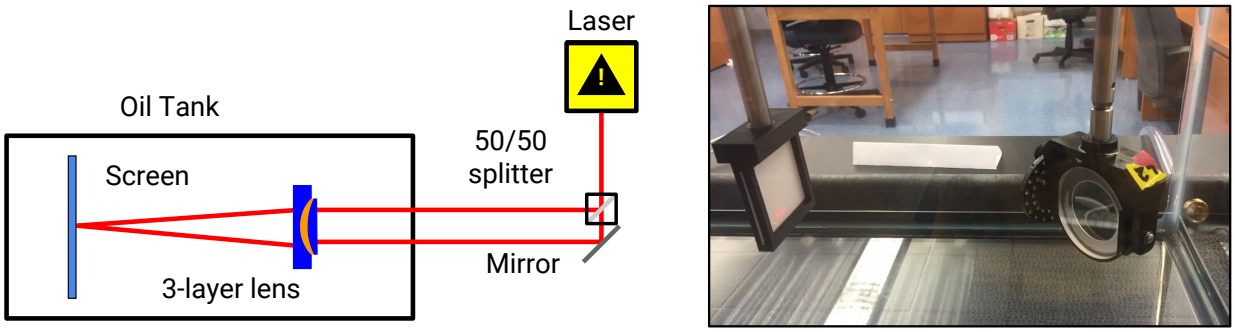

FIG. 35: Laser setup at Old Dominion University for testing the optical properties of the 3-layer lens design. A schematic drawing of the setup is shown on the left, and a closeup view of the lens and screen inside the actual setup is shown on the right. [29].

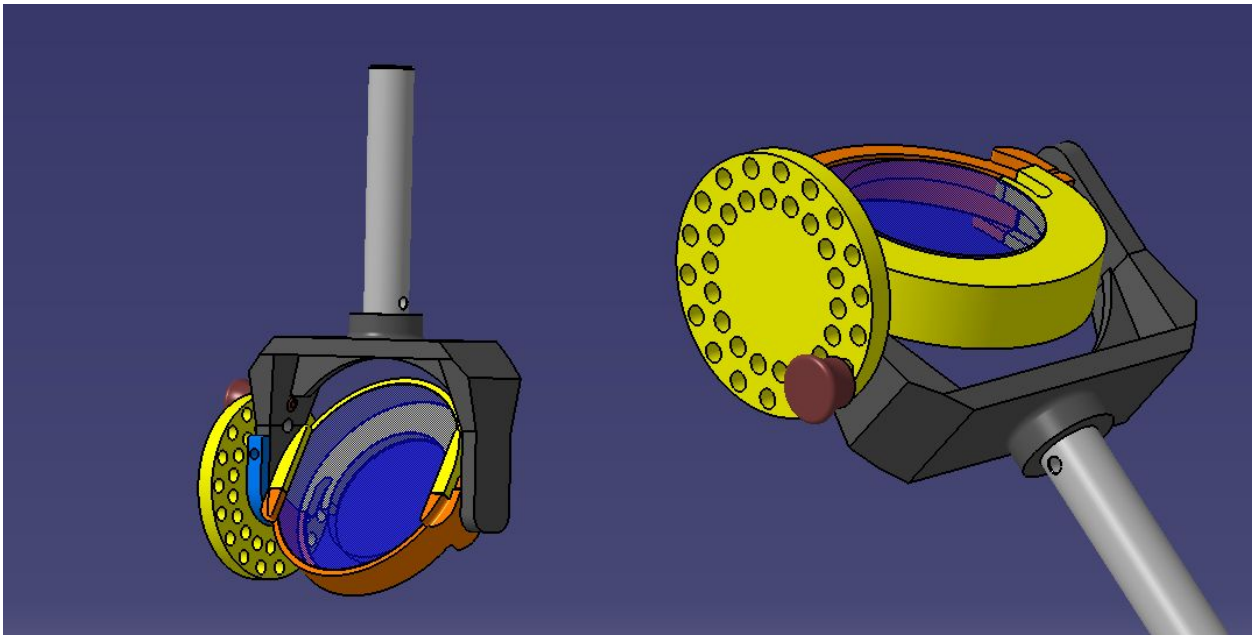

FIG. 36: CAD drawing of 3-layer lens holder which allows precision rotation in two orthogonal, allowing the full 3D focal plane to be mapped.

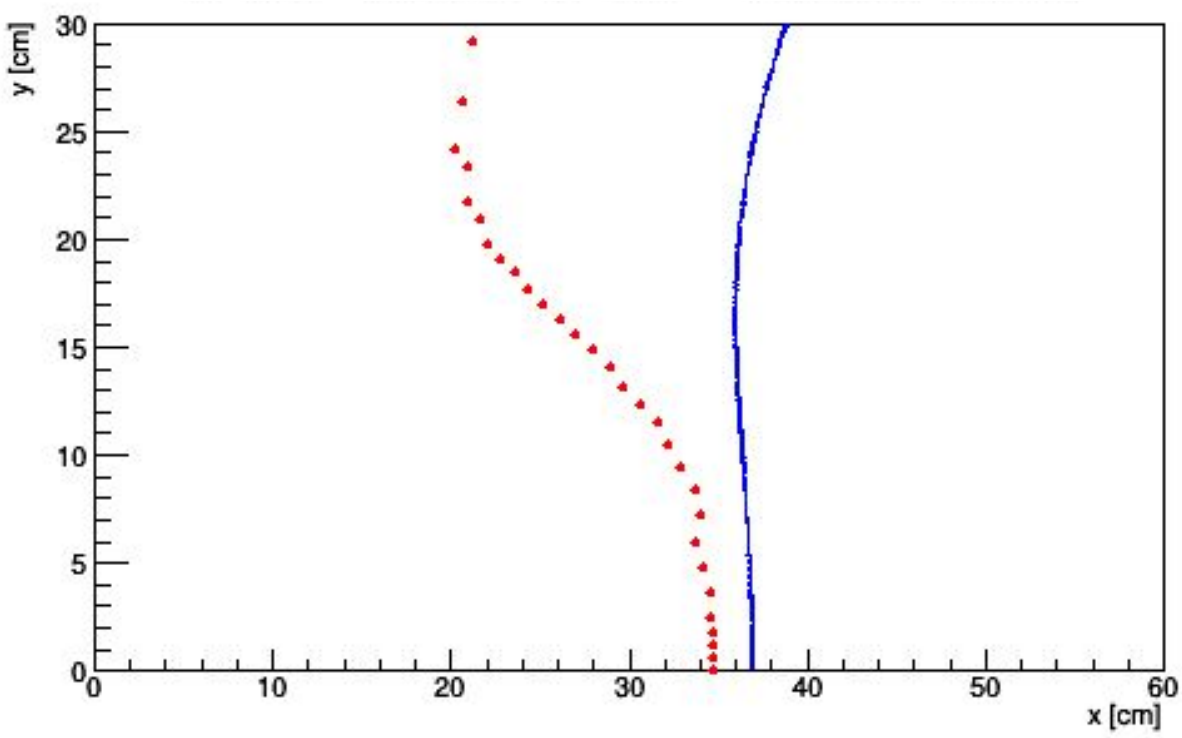

FIG. 37: Initial measurement of the 3-layer lens focal plane using the upgraded green laser (red dots) compared to simulation (blue line). Note that this figure is for illustrative purposes only. The measurement techniques used to measure the focal plane were changed to match the simulation, shown in Figure 39.

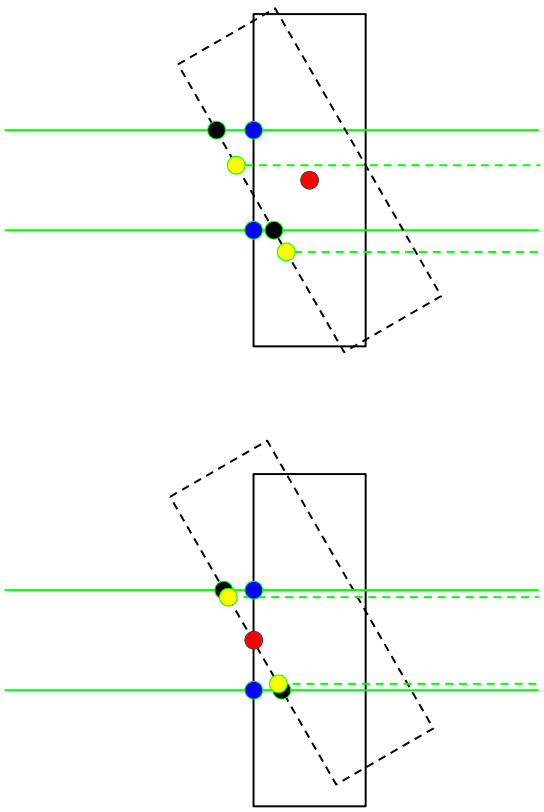

FIG. 38: Illustration of the discrepancy between beam positions in data (black) and simulation (yellow). The original beam positions (blue) for a given rotation point (red) at the center (top) of the lens, or at the edge (bottom) of the lens make the discrepancy clear.

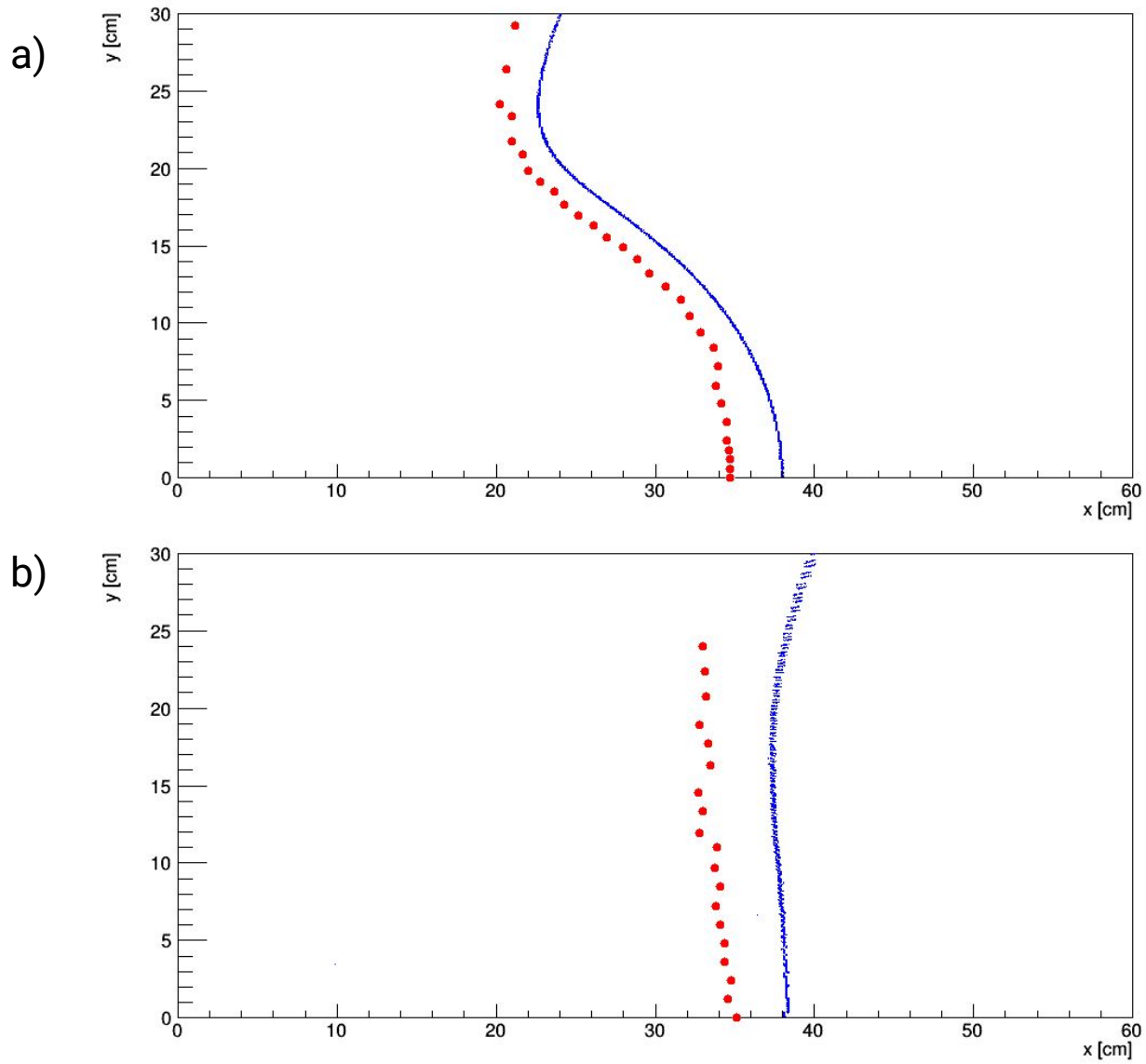

FIG. 39: Initial measurement of the 3-layer lens focal plane compared to a rotation corrected simulation (a), and a second measurement with a tighter (2 mm) beam configuration and a modified lens holder (b).

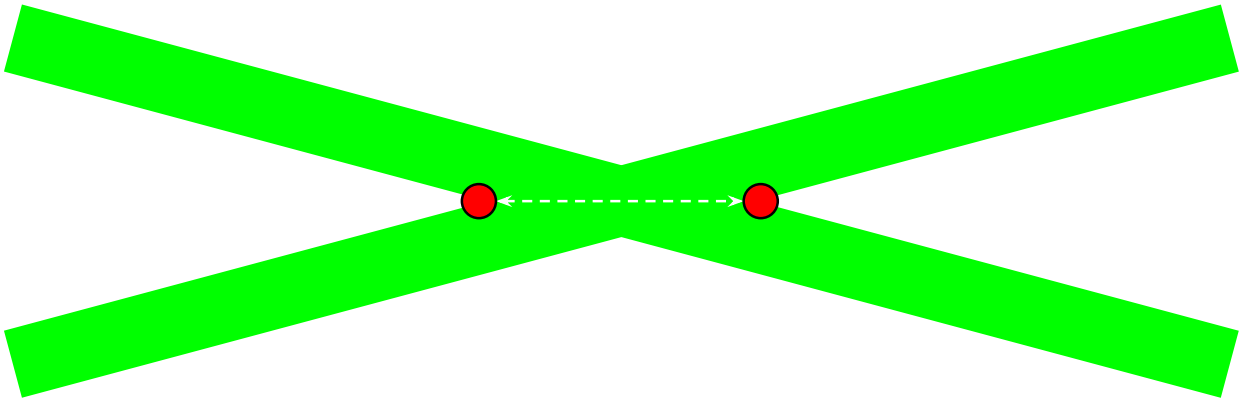

FIG. 40: Illustration of two crossing laser beams (green) with finite size. During measurements all the space between the two red circles was perceived as a single point. To counteract this effect the focal point was taken as the average point between where the beams first seem to come together and where they seem to again separate.

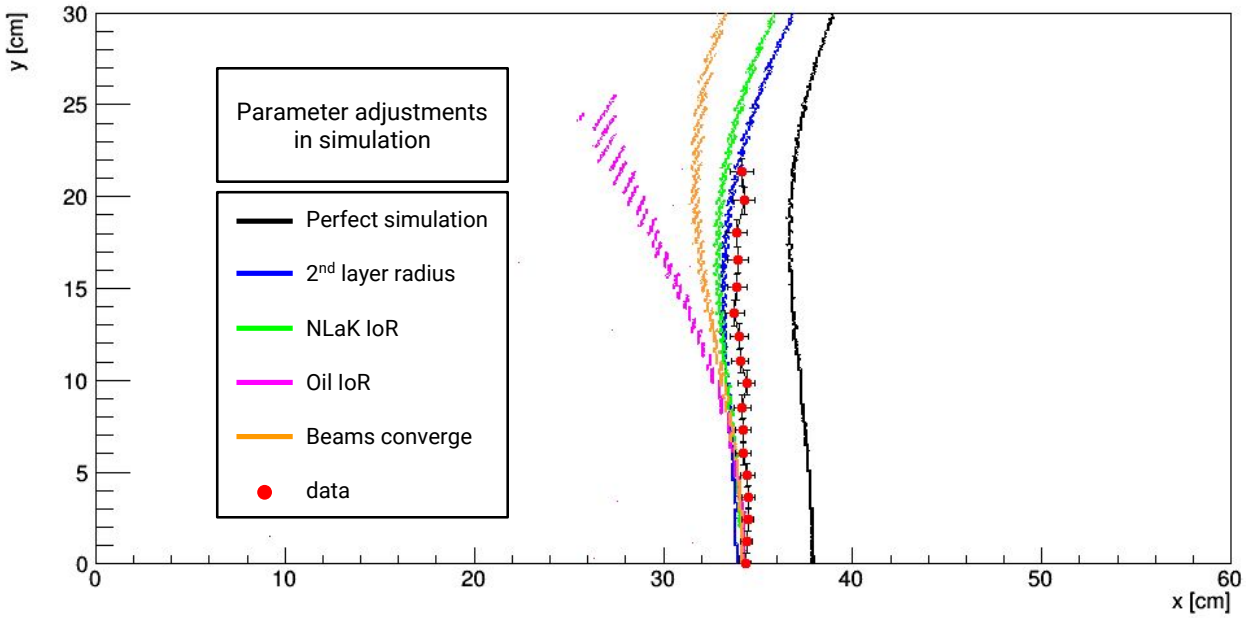

FIG. 41: Shifting the focal plane of the GEANT4 simulation. The simulated effects are a decrease in the radius of the second layer by 1.3 mm (blue), an increase of the refractive index of NLaK33 by 0.03 (green), a decrease of the index of refraction of the mineral oil by 0.15 (pink), and adding a converging angle of the laser beams of 0.15 mrad (black). Experimental data is shown in red and simulation with "perfect" parameters is shown in black.

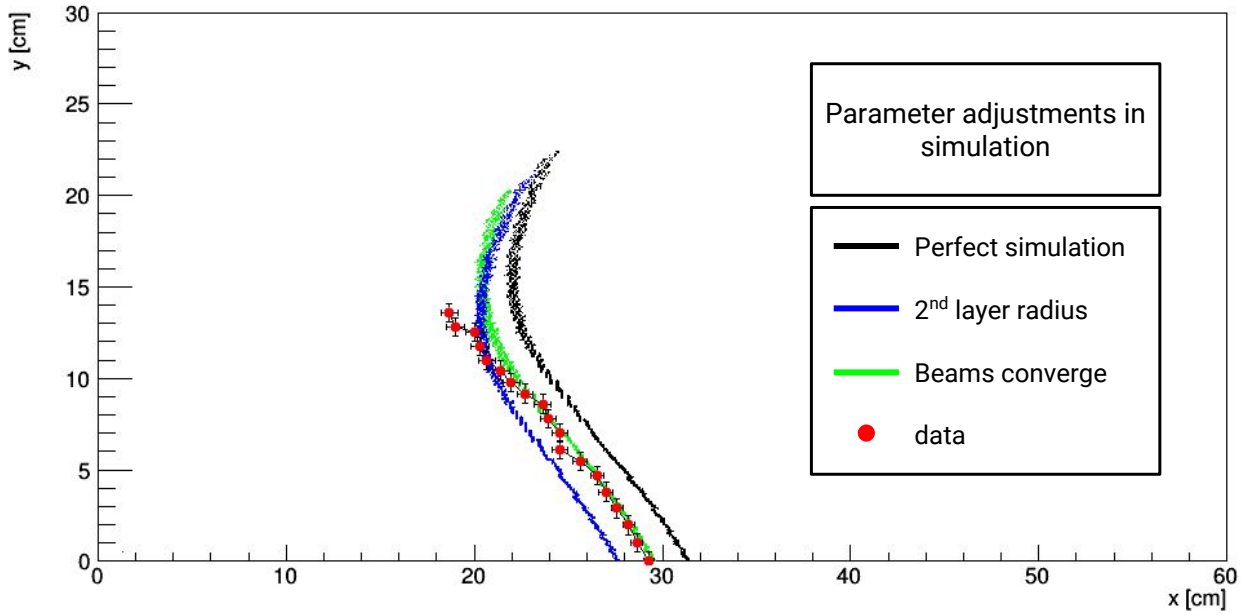

FIG. 42: Focal plane after implementing a 7 mm shift along a line connecting the two beams. Data and simulation assuming "perfect" parameters are shown in red and black respectively, while a reduction in the radius of the second curved surface is in blue, and a non-parallelism between the laser beams is in green. Clearly the modification of the radius overcompensates for the change in the position and shape of the focal plane while the non-parallelism assumption agrees very well.

5.2 RADIATION HARDNESS OF NLAK33

Fused silica, which is used for most of the optical components in all current DIRC designs, was already extensively tested in the BaBar and PANDA experiments [31] and has proven to be radiation hard up to several hundred krad with little to no loss of transmission. The determination of the radiation hardness of NLaK33 is an important study for the EIC R&D program.

The irradiation of a pure sample of NLaK33 material was performed at Catholic University of America (CUA) in a Faxitron CP-160 Cabinet X-Radiator System [32] (Figure 43a). The cabinet allows for a minimum of 6 second X-ray exposure. Photon energy was set to 160 keV with a 6.2 mA current for all exposures of the NLaK33 sample.

A RaySafe ThinX RAD dosimeter [33], shown sitting on the X-ray cabinet shelf in Figure 43b, was used to measure the radiation dose being delivered to the sample. Unfortunately the exposure time of the dosimeter is limited to less than 10 seconds, so the shortest time setting on the X-ray cabinet was used. This exposure time of 6 seconds was found to be closer to 7.5 seconds by the dosimeter due to rise and fall time of the source. This shortest exposure time consistently gave readings of 81.4 rad. The dosimeter has a circular active area of 706.9 mm^2 while the side of the NLaK33 sample that was exposed to the source has an area of 8×28 mm^2, so the dose delivered to the sample is approximately 25 rad.

To measure the transmission of the sample a LAMBDA 950 UV/Vis/NIR Spectrophotometer [34] (Figure 44a), referred to from here on as a monochromator, was used. The monochromator has a dynamic range between 175 - 3,300 nm wavelength in 1 nm steps. The sample of NLaK33 was held in place using an optics stand (Figure 44b) to make sure measurements were consistent and reproducible. Measurements of the transmission of the sample were taken between each set of radiation exposures. The transmission of sample of fused silica was also tested between each radiation exposure of the NLaK33 sample, but was only used as a control sample and was found to be stable.

Because it was not clear exactly what percentage of the total dose read by the dosimeter was from the warm up and cool down of the cabinet it was decided that the best approach for exposure of the sample was to do multiple steps of the 6 second exposure time and record the accumulated dose in this manner. The first exposure was 4 intervals for a total of 100 rad. After this measurement it was noticed that there was already a roughly 2% drop in the transmission of the sample at 420 nm wavelength [2], so steps of 50 rad were taken for

[2] 420 nm wavelength was chosen because it is near the peak of the quantum efficiency of the multi-channel plate photomultiplier tubes discussed later in this chapter and used in the analysis presented in Chapter 6

the next several measurements. After 700 rad of dose it was clear that there was a linear correlation between accumulated dose and loss in transmission, so it was decided that 100 rad steps could again be taken.

Results for the radiation hardness tests of the NLaK33 sample are shown in Figure 45. The transmission loss below roughly 350 nm wavelength and above 700 nm wavelength seems to be negligible. However, in the range of 350-700 nm there is a clear dip in transmission. At 420 nm wavelength, corresponding to the peak in the quantum efficiency of the photodetectors used in the DIRC, sees a 1.3% drop in transmission per 50 rad of dose. While it is not yet clear what the expected integrated dose will be in the area of the DIRC at the EIC it is assumed that this loss is too great over the lifetime of the detector. Other materials known to be radiation hard, such as lead fluoride, are being investigated as possible alternatives.

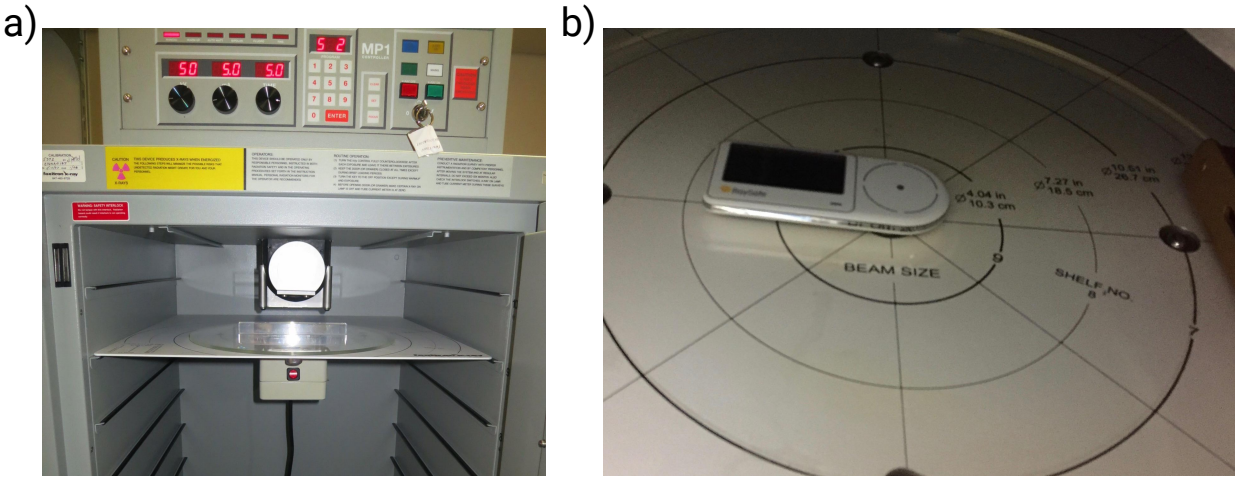

FIG. 43: Components used for testing the radiation hardness at CUA. The Faxitron CP-160 Cabinet X-Radiator System (a) used to irradiate the NLaK33 sample with 160 keV photons at 6.2 mA current for 6 second intervals, and the RaySafe ThinX RAD Dosimeter (b) sitting on one of the X-ray cabinet shelves.

a)

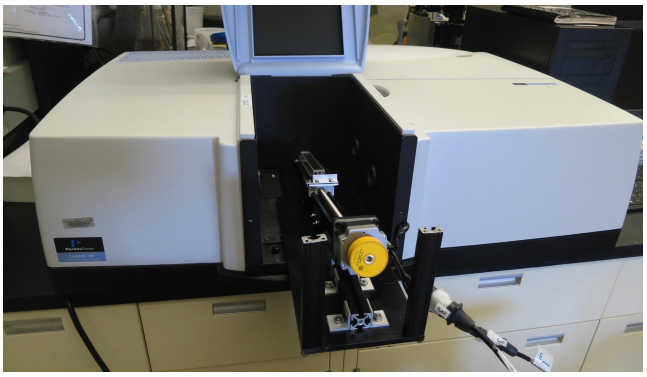

b)

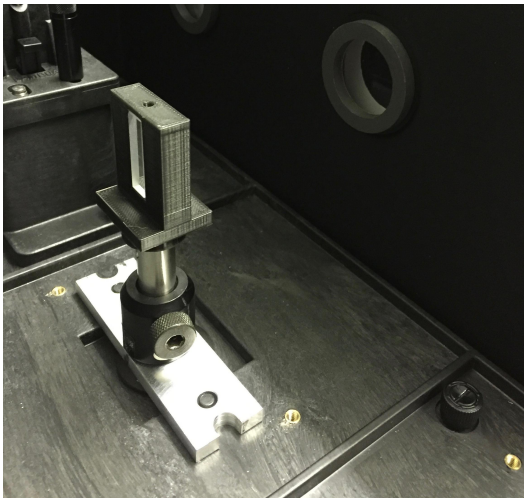

FIG. 44: The LAMBDA 950 UV/Vis/NIR Spectrophotometer (a) and a closeup view of the NLaK33 sample being held in position by the optics stand (b).

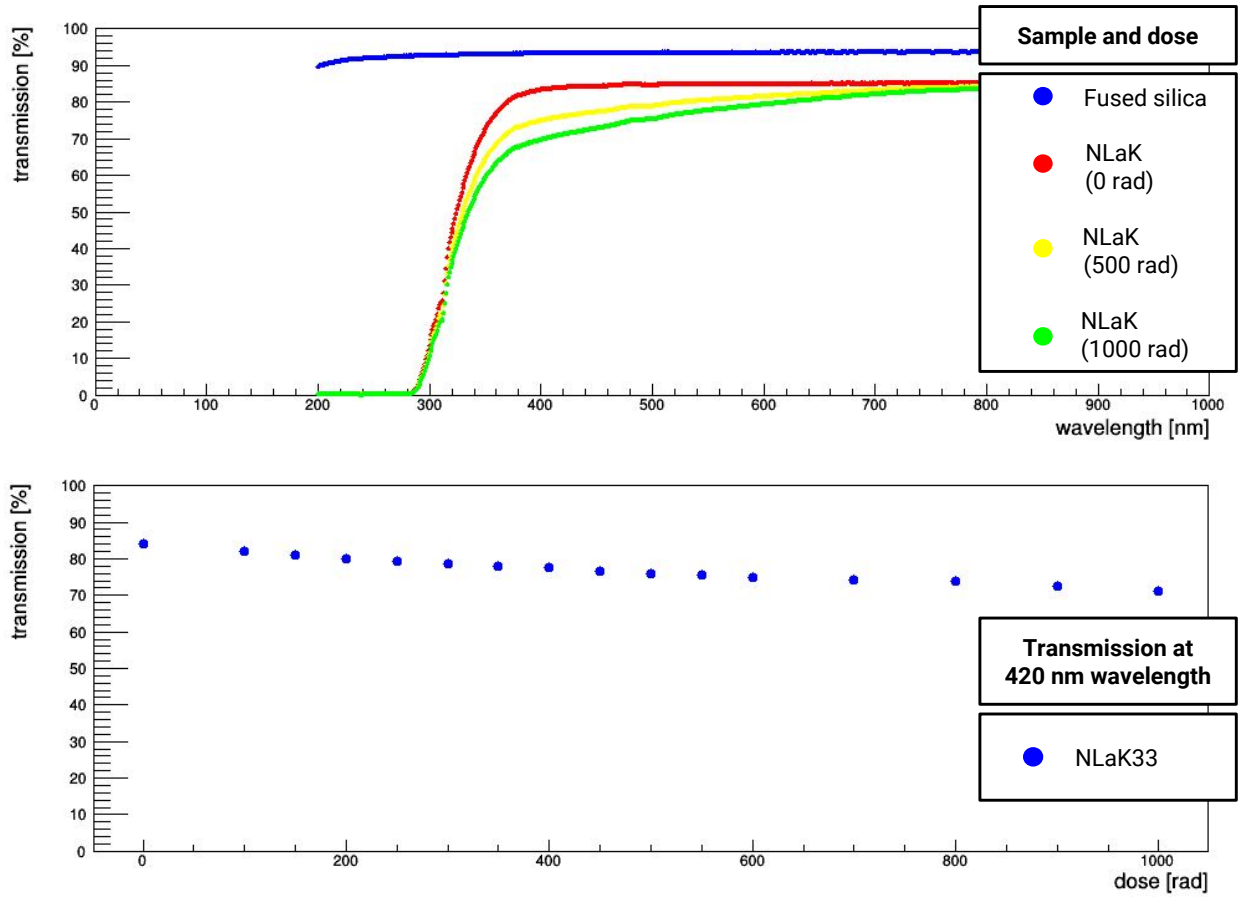

FIG. 45: Radiation hardness results for the NLaK33 sample. The top plot shows the transmission of the control sample of fused silica (blue) and the transmission of the NLaK33 sample after 0 (red), 500 (yellow), and 1000 (green) rad dose across a range of 200-800 nm wavelength. The bottom plot shows the transmission of the NLaK33 sample at 420 nm wavelength as a function of the dosage. After the first 700 rad of dose it was clear that there was a linear relationship between dose and transmission loss, so 100 rad steps were used afterwards.

5.3 PERFORMANCE OF MCP-PMTS IN HIGH MAGNETIC FIELD

The limiting space requirements of the EIC DIRC design, as mentioned in Chapter 4, places a unique set of requirements on the DIRC readout sensors. In order to achieve the desired single photon resolution while maintaining a sufficiently sized expansion volume the sensors, and therefore the pixels, must be compact. Furthermore, due to the positioning of the readout plane inside the large field of the solenoid magnet (see Figure 4) these sensors must also have a high tolerance to magnetic fields, both in magnitude (up to 3 T or higher), non-uniformity, and orientation. Ordinary photomultiplier tubes (PMTs) are not an option due to their susceptibility to magnetic fields, being affected by fields as small as 0.5 Gauss [35]. Silicon photomultipliers (SiPMs) are attractive due to their very compact size and their resistance to magnetic fields up to 4 T [36]. However, the inherent background, or dark count, of SiPMs is very large, on the order of MHz per pixel [36] [37]. Because a DIRC detector only expects 100 photons per event at most spread over 100 ns, this level of background is far too large for usability. The dark noise can be mitigated by cooling, with a decrease by a factor of approximately 2 per 5° C, but the large amount of cooling required around the SiPMs in the EIC detector would be costly both in space and finance. With these requirements in mind the best option for an EIC DIRC detector is the use of micro-channel plate photomultiplier tubes (MCP-PMTs) (Figure 46). The dark count of MCP-PMTs is on the order of kHz [38], which is much more acceptable compared to SiPMs. MCP-PMTs also have a much higher resistance to external magnetic fields than traditional PMTs due to the small pore size, with studies being done up to 2 T [39], [40], [41], [42], [43], [44]. The tests described below are the first to study the effects of fields as large as 5 T on MCP-PMTs.

5.3.1 EXPERIMENTAL SETUP

In the fall of 2014 two single-anode MCP-PMTs were tested at Jefferson Lab [45], a PHOTONIS PP0365G (6μm pore size and a 18.2 mm active area) [46] and a Photek PMT210 (3μm pore size and a 10 mm active area) [47], shown in Figure 47 at the top and bottom right respectively. The FROST superconducting solenoidal magnet, with a field tunable up to 5 T with a cylindrical bore diameter of 12.7 cm and a length of 76.2 cm, was used for testing [48]. The central field of the magnet, while quite large, is also very homogeneous, with an inhomogeneity of less than 5×10^{-5} over a cylindrical volume with a diameter of 1.5 cm and a length of 5 cm. The sensors were held in place at the center of the magnet using a custom-built, non-magnetic, light-tight cylindrical dark box, as shown in Figure 47.

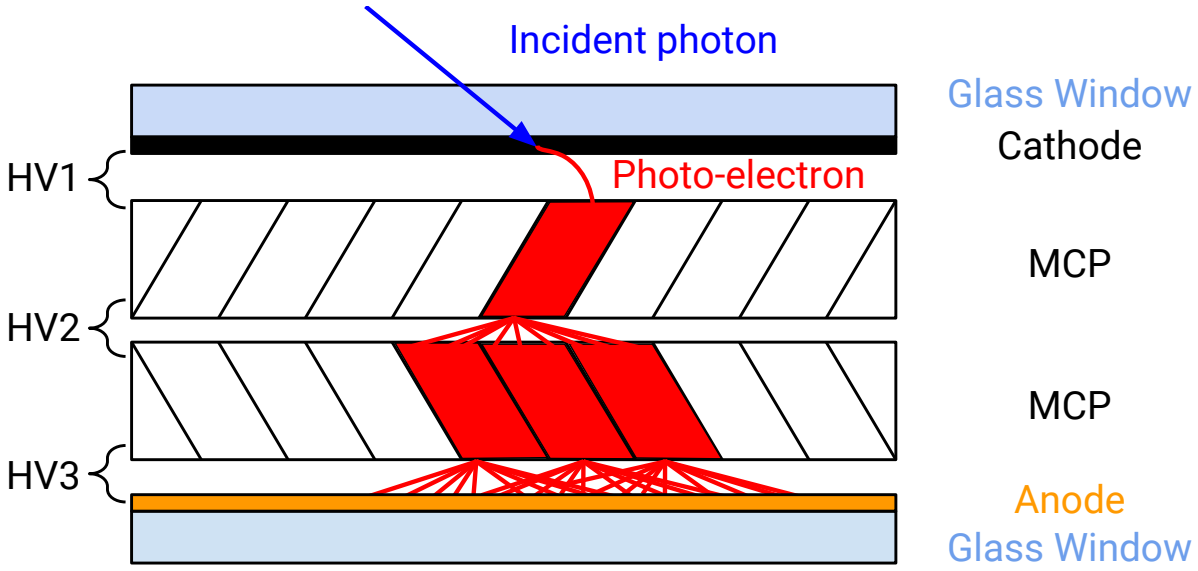

FIG. 46: Schematic of the Micro-channel Plate photo-multiplier tube (MCP-PMT) concept. A cathode and anode sandwich two conducting plates with micrometer-sized channels (MCP), and a high-voltage (HV) difference (HV1, HV2, HV3) between every two components. The channels, or pores, of the two MCPs are aligned in a chevron pattern. An incident photon (blue) strikes the cathode, producing a photo-electron (red). That electron is accelerated through the potential difference between the cathode and first MCP (HV1) before striking the inside of one channel. This creates the same effect as an electron striking the dynode of a typical PMT, resulting in an avalanche of photo-electrons that emerge out of the other side of the first MCP. These electrons are again accelerated through a second potential difference (HV2) before repeating the process in the second MCP. Finally, the copious photo-electrons exit the second MCP, are accelerated through a final potential difference (HV3), and are collected on the anode. This design is both much more compact, more resistant to magnetic fields compared to traditional PMTs, and has less timing jitter.

Inside the dark box the sensor was held in place by a turn table that allowed for rotation around a vertical axis as well as a horizontal axis (the Y(Y') and Z(Z') axes in Figure 48 respectively). The range of the polar angle θ was dependent on the size of the sensor being measured as well as the signal and HV cables connected to the back of the sensor. A cart allowed the sensor to move relative to the dark box for precise positioning at the center of the magnet. The gain of both sensors were scanned for various angles of θ, ϕ, and a range of magnetic field from 0 to 5 T.

A pulser-driven LED was used to illuminate the MCP-PMTs with 470 nm photons. An optical fiber was used to transmit the photons to the dark box and a diffuser installed inside the dark box cap was used to illuminate the entire face of the sensor with nearly constant

intensity and 10 ns wide pulses at 30 kHz. The sensor signal output was then amplified using a 200-times preamplifier and used as input to a 250 MHz flash analog-to-digital converter (fADC) with 4096 sample depth provided by the JLab Electronics Group. The fADC was then read out by our data acquisition system (DAQ).The pulser was also used as the trigger signal for the fADC, as shown in the chart in Figure 48 (right).

My contribution to these studies was assisting in the experimental setup, data monitoring and collection, restructuring and updating the signal reconstruction software, and operating the FROST magnet and electronics both during and between runs. The analysis of the data was done by Dr. Yordanka Ilieva from the University of South Carolina, who's results are shown below and taken, with permission, from [45].

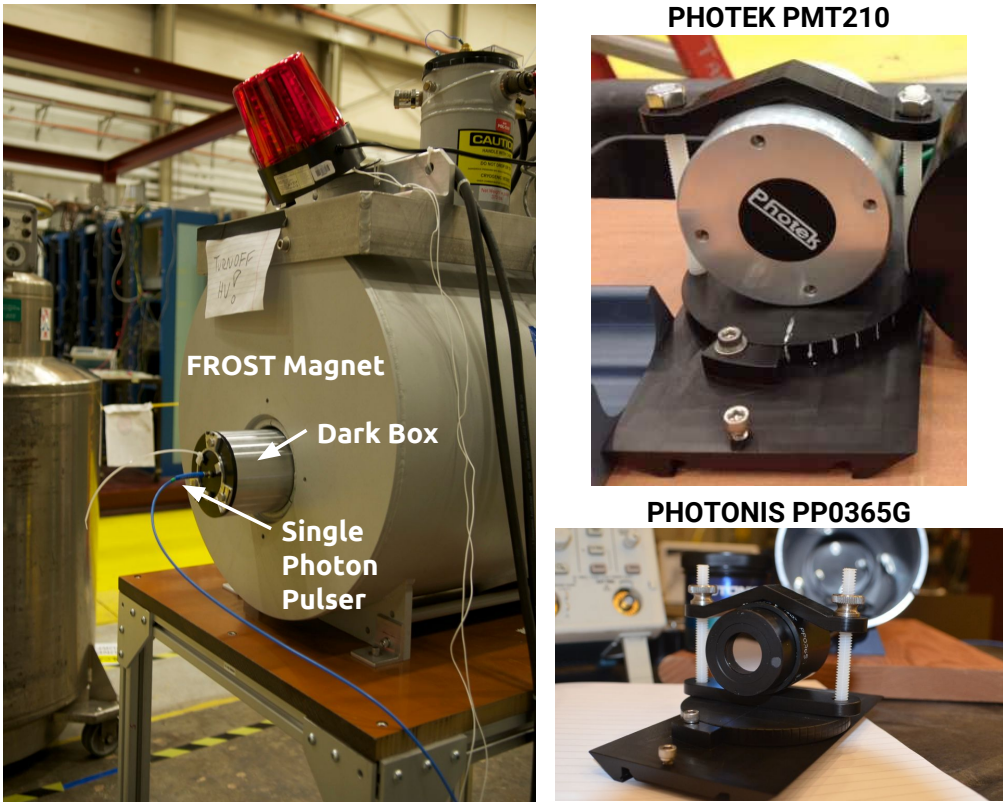

FIG. 47: The FROST superconducting magnet (left) with the dark box placed in the bore, and the Photek PMT210 (top right) and PHOTONIS PP0365G (bottom right) MCP-PMTs used for testing at JLab [45].

5.3.2 RESULTS

The gain of the sensors is proportional to the average charge per pulse collected on the sensor anode, and thus the performance can be measured in terms of the average charge

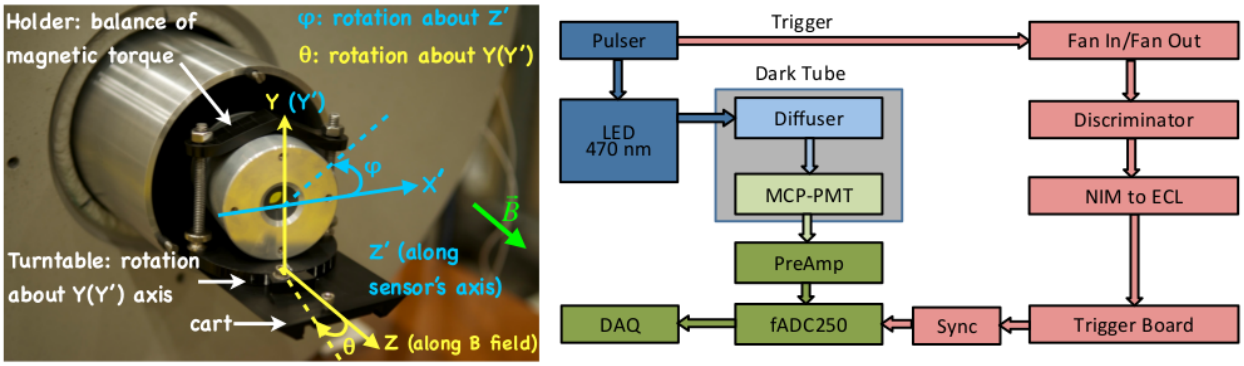

FIG. 48: High magnetic field testing setup at JLab. Left: A closeup of the dark box showing the Photek PMT210 being held in place by the turn table. This setup allows the MCP-PMT to be rotated around both the horizontal Z(Z') axis as well as the vertical Y(Y') axis (with respect to the floor). The rotation about the Y(Y') and Z(Z') axes are described by the polar angle θ and azimuthal angle ϕ respectively. The magnetic field is parallel to the central axis of the dark box. Right: A flowchart of the readout used for testing. The photocathode is exposed to single 470 nm photons to produce photoelectrons, with a large voltage difference between the anode and cathode used to create an avalanche. The total charge is collected on the anode, amplified by a preamplifier, and digitized by an fADC and read out by a DAQ [45].

collected on the fADC. This is calculated by taking the integral of the fADC signal. The fADC samples the signal every 4 ns in a 1μs window. For each event, i, the average pedestal was determined from the fADC using the first 20 bins, and the waveform is integrated over 9 bins around the peak. The integral of the pedestal is subtracted, resulting in a value, $Q_{9,i}$, that is proportional to the total charge collected on the anode for that event. The average values of $Q_{9,i}$ for each setting of field, θ, and ϕ are used in the results presented. Figure 49 (left) shows an example of a waveform from the PP0365G sensor. Another strategy used for calculating the collected charge was to integrate the entire pedestal-subtracted average waveform (Figure 49 right). This yielded results consistent with the event-by-event analysis.

Figure 50 shows the performance of both sensors at the nominal ($\theta = \phi = 0°$) position for magnetic fields up to 5 T. Data were taken for HV settings of 93% (black) and 97% (red) of the maximum manufacturer-recommended HV value. The PP0365G sensor shows a smooth, nearly linear decrease in charge as the field increases, being able to operate at up to 3 T with a factor of 15 loss in collected charge. By increasing the HV the operational range was extended to 3.5 T. The PMT210 has an increase in the collected charge up to 0.5 T with a smooth decrease thereafter as the magnitude of the field increases, staying operational until 4 T with only a factor of 6 decrease in collected charge. Increasing the HV allowed signal to

be collected up to 5 T. An uncertainty of 5%, shown in the error bars of each data point, was the dominant source of error, with the systematic uncertainty giving less of a contribution. The latter was estimated as the standard deviation of the sample of repeated outcomes of the average collected charge at the same setting (mainly the nominal angle setting at a 0 T field) from runs taken randomly throughout the measuring period. The standard deviation acccounts for the variations of the light intensity on the photocathode and of the positioning of the sensor in the dark box.

Figure 51 shows the response of the sensors at various θ angles up to 30°. As one can see, the two sensors have very different responses. The magnetic field dependence of the collected charge for the PP0365G shows a maximum below 1 T for $\theta = 20°$, 25°, and 30°, while $\theta = 0°$ and 10° show a smooth decrease as magnetic field increases. There is also a much more rapid decrease in collected charge at fields above 1 T for higher angles. The PMT210, however, shows a more uniform characteristic for all θ angles. For both sensors, as the θ angle increases the field range in which the sensor can reliably operate becomes more narrow.

The effect of changing the ϕ angle of the PP0365G sensor for different magnetic field strengths and θ angles of 10° and 20° can be seen in Figure 52. Because the outer casing of the sensor is cylindrical and there is no apparent orientation, a $\phi = 0°$ position was chosen randomly and marked on the front of the casing for consistency. The rotation was done counterclockwise about the sensor's axis when looking from the front. The data shows that at a fixed θ angle the collected charge has a ϕ dependence, and this dependence is strongly correlated to the θ angle. The larger θ angle shows a much faster decrease in collected charge as the ϕ angle increases.

5.3.3 CONCLUSIONS

Overall the data at $\theta = 0°$ suggests that a smaller pore-size sensor (PMT210) has a higher resistance to the effects of high magnetic fields as it was able to operate up to 5 T fields and had a slower decrease in collected charge with increasing field than the PP0365G sensor. The smaller pore-size sensor as showed an higher increase in collected charge with increased HV. When increasing the θ angle, however, the PMT210 showed a much more rapid decrease in performance compared to the PP0365G. At 0° the PMT210 can be operated up to 5 T, while rotating to 5° there is a dramatic decrease in maximum field to 2 T. The PP0365G sensor, however, was more stable with rotations in θ, dropping from 3 T at 0° to 2 T at larger angles.

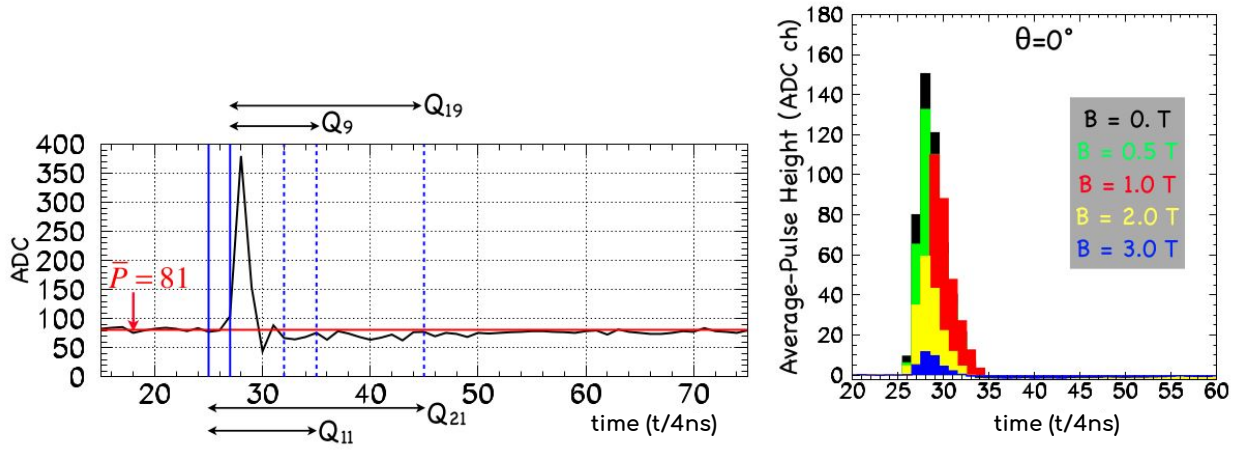

FIG. 49: Observed waveforms during high magnetic field testing of the MCP-PMTs. Left: an example waveform measured for the PP0365G sensor. Each bin of the x-axis corresponds to a 4 ns interval. The y-axis is the fADC value (ranging from 0 to 4096). The solid red line shows the calculated pedestal position for the event. The ranges Q_9, Q_{11}, Q_{19}, and Q_{21} denote the positions of integration ranges over 9, 11, 19, and 21 bins respectively for calculation of the total anode charge for that event. The limits and width of the integration range were varied for systematic purposes. Right: the average waveforms of the PP0365G sensor at $\theta = 0°$ and varying magnetic field strengths. There is a clear negative correlation between the signal amplitude and field magnitude [45].

While the data for the two sensors allow to make general conclusions about the effect of pore size on performance, more detailed conclusions cannot be made with certainty as the orientation of the MCPs inside the sensors are not necessarily the same. While the definition of the θ angle is consistent for both sensors in this testing, the azimuthal orientation of the channels relative to the central axis may differ greatly. No details are given by the manufacturer about the absolute azimuthal orientation of the channels for each sensor as this information has not as of yet been necessary for applications of MCP-PMTs. These data, however, suggest that this will be important for optimization of the sensor design and operational parameters for operations in areas of non-homogeneous, high-strength magnetic fields, such as for the EIC DIRC.

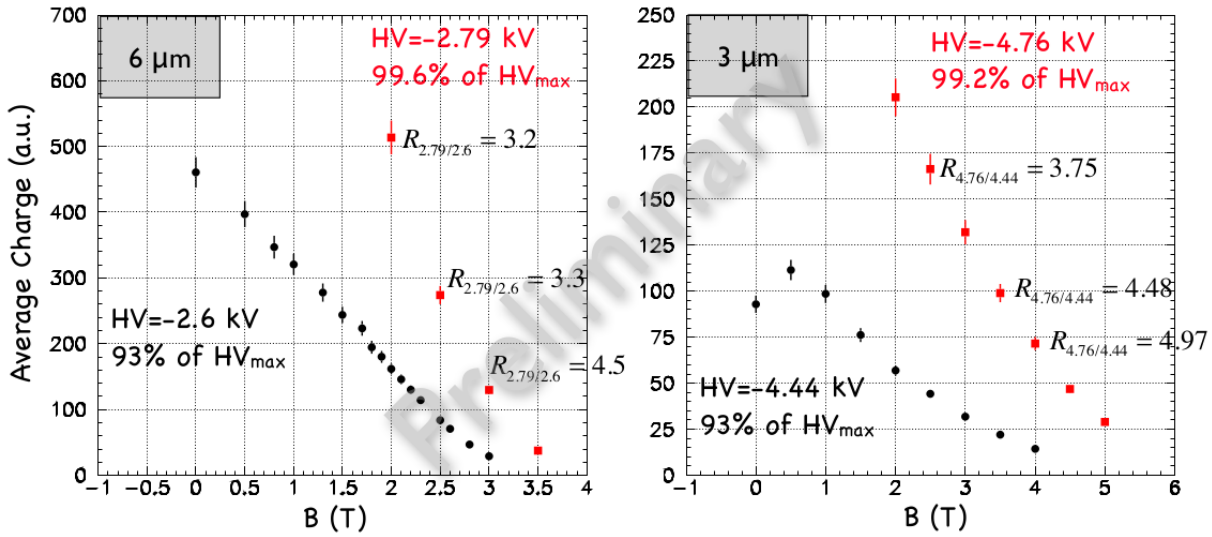

FIG. 50: The gain performance of the PP0365G and PMT210 sensors (left and right) at $\theta = 0°$ and two HV settings [45]. The black and red points were measured using 93% and 99% of the maximum manufacturer recommended HV (HV_{max}) settings respectively. For the PP0365G at 93% (95%) of HV_{max} a reasonable signal can be obtained up to a 3 (3.5) T field, though the total collected charge decreased by a factor of 15 when going from 0 T to 3 T. The PMT210 was able to produce a signal at fields up to 4 (5) T, and the collected anode charge decreased only by a factor of 6 when going from 0 to 4 T. The error bars on all points include both statistical and 5% systematic uncertainties, with the latter being the dominate contribution.

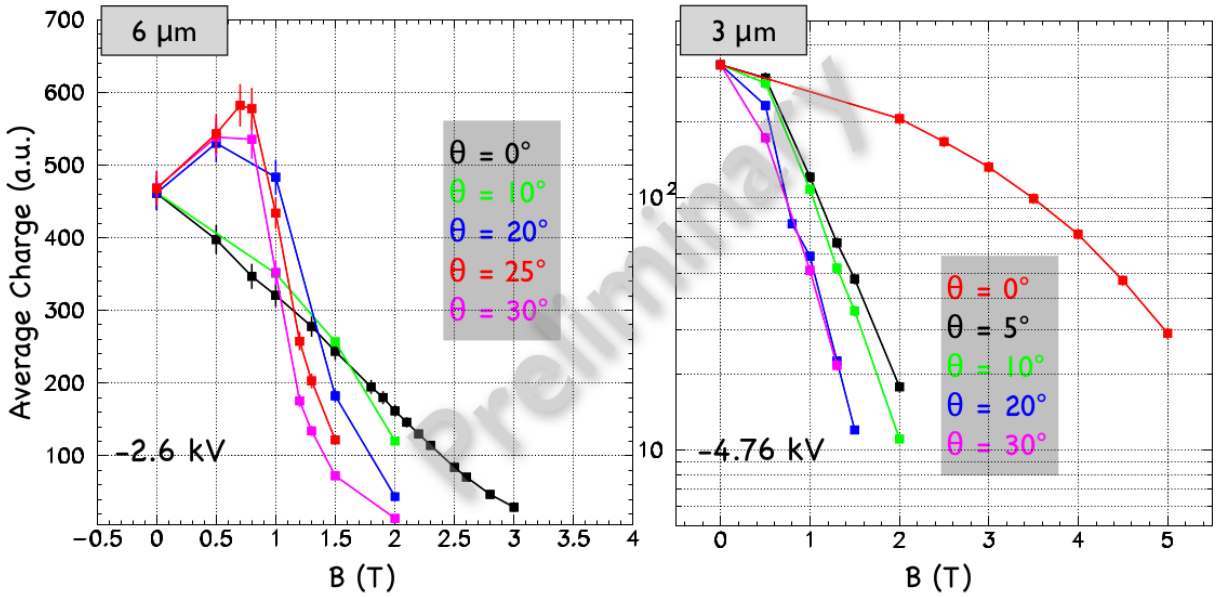

FIG. 51: The average collected anode charge as a function of magnetic field strength at various θ rotation angles for the PPP0365G (left) and PMT210 (right) sensors [45].

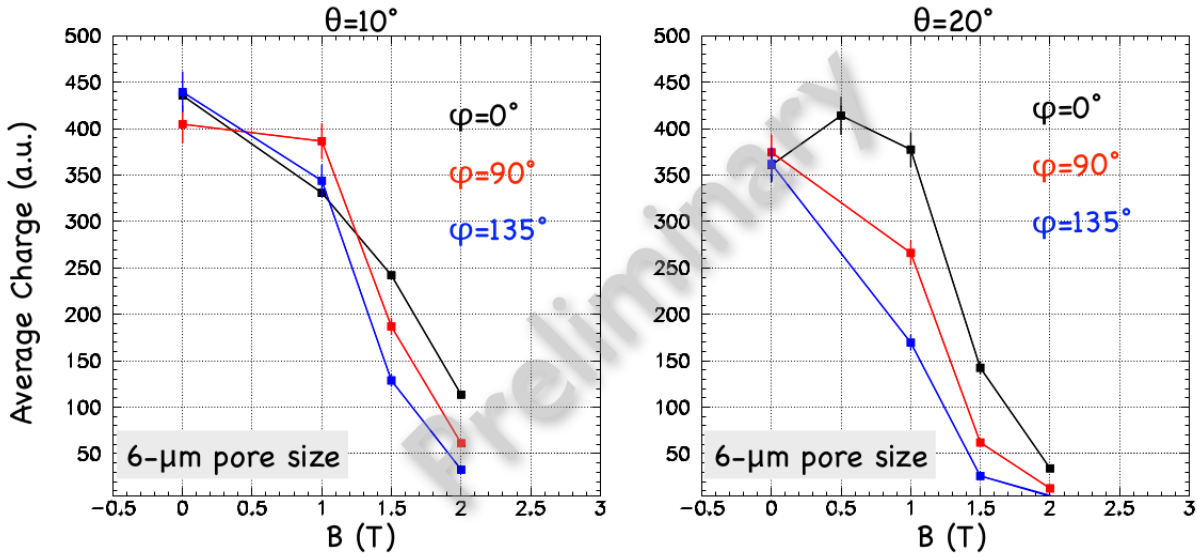

FIG. 52: The average collected anode charge as a function of magnetic field strength at various ϕ rotation angles for the PP0365G at fixed θ angles of 10° (left) and 20° (right) [45].

CHAPTER 6

3-LAYER LENS PERFORMANCE IN A PARTICLE BEAM

Along with determining the focal plane and radiation hardness of the 3-layer lens design, another crucial step towards solidifying an EIC DIRC design was to test the new lens in a prototype DIRC with a real particle beam. Because not all of the components of the high-performance DIRC baseline design for an EIC are currently available it is necessary to validate the simulation package currently used to design and optimize the system. In June and July of 2015 the PANDA Barrel DIRC group along with myself and Dr. Grzegorz Kalicy from CUA conducted a test beam at the European Organization for Nuclear Research (CERN) with a prototype DIRC for the PANDA experiment. This was used as an opportunity to evaluate the performance of the 3-layer lens in a real particle beam. The beam was a hadron-rich beam with momentum tunable from 1 - 10 GeV/c. A standalone GEANT4 simulation package developed for the PANDA DIRC prototype (and later modified for the EIC DIRC geometry) was used for look-up table (LUT) generation, data monitoring, and comparison to data. The two most important quantities measured during this test beam were the photon yield per track and the Single Photon Resolution (SPR). Verifying these measurements with simulation gives a good indication that the performance shown in Chapter 4 is what should be reasonably expected from a real EIC DIRC detector.

6.1 2015 TEST BEAM PROTOTYPE SETUP

The PANDA prototype was situated in the CERN Proton Synchrotron (PS) T9 experimental hall [49]. A 200 mm thick aluminum target upstream of the T9 hall was used to produce a hadron-rich beam comprised mostly of protons, pions, muons, and electrons with a very small amount of kaons. A series of dipole and quadrupole magnets allowed for steering and focusing of the beam, as well as selecting specific particle momenta in the range of 1 to 10 GeV/c for data taking. A scintillator monitored the intensity of the beam and a wire chamber monitored the x/y profile at the exit of the beam pipe.

A CAD drawing of the experimental setup in the T9 hall can be seen in Figure 53. The DIRC prototype was situated between two time-of-flight (TOF) detectors that were spaced 29 m apart to tag protons and pions. Figure 54 shows the time-based separation of different

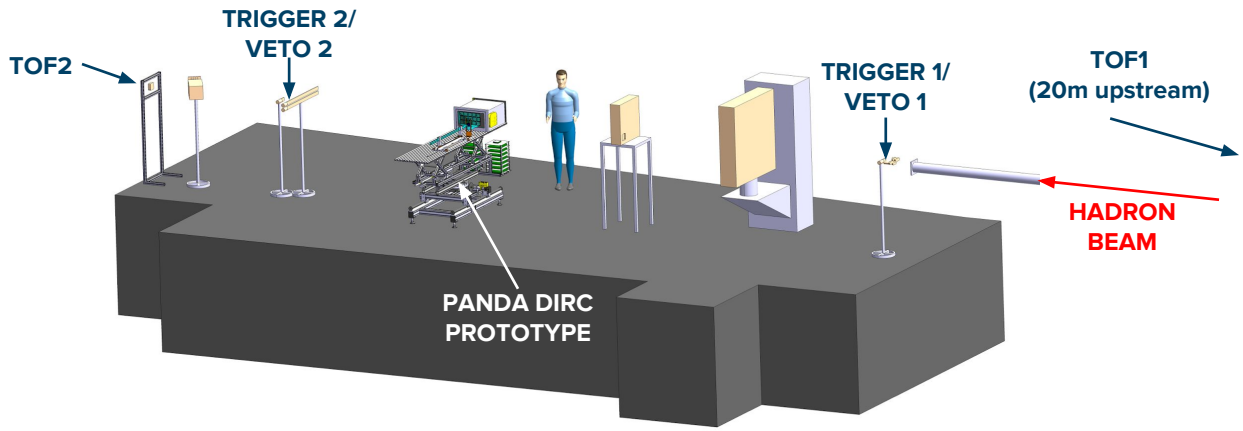

FIG. 53: CAD drawing of the T9 experimental hall with the PANDA DIRC prototype setup [21]. Two time-of-flight (TOF) detectors were separated by 29 m and used for proton/pion separation. Two trigger systems were used for the start and stop times of the readout electronics.

particle species for 4 different beam momenta. Two scintillator counters (named Trigger 1 and Trigger 2) were placed in front of and behind the prototype. A coincidence of the trigger signals was used as the DAQ event recording trigger. Two veto counters were also set up between the two TOF detectors to reject background particles that strayed significantly from the beam path.

Figure 55 shows a CAD drawing of the prototype setup. The prototype was held in place by a custom-built aluminum support structure with rails and a rotating table that allow the detector to be translated and rotated relative to the beam. The rotation of the prototype was verified using a remotely operated motor and camera. The radiator was carefully held in place by two aluminum braces equipped with three micrometer screws which allowed for fine adjustments in the position of the bar. Alignment of all components in the beam line were done with a GLL2-80 Dual Plane Leveling and Alignment Laser by Bosch [51], which provides both vertical and horizontal self-leveled planes. An example of alignment of a radiator plate is shown in Figure 56.

The optical component is attached to one end of the bar and a mirror is attached to the other. A compact prism expansion volume with dimensions $50 \times 170 \times 300$ mm^3 and an opening angle of 30° (shown in Figure 57) was attached to the optical component (except in the case of an air-gap lens). A 3×5 array of PHOTONIS Planacon XP85102 MCP-PMTs with a total of 960 pixels (6×6 mm^2 each) were held in place by a support structure and coupled to the expansion volume. The MCP-PMTs were read out by a DAQ system

based on the trigger and readout board (TRB3) and the PADIWA discriminator card [52]. Couplings between the bar/lens, lens/prism, and prism/MCP-PMTs were done using Eljen EJ-550 optical grease [53]. The mirror was not coupled directly to the bar, but held in place flat against the bar in order to prevent slight variations in grease thickness from effecting the angle of reflection.

The discriminating threshold signals for each MCP-PMT was adjusted and the difference between the discriminator and trigger signals were recorded by the TRB system. Noise events such as photons from delta electrons in the radiator bar and dark noise from the detectors were cut out using this timing information. Some channels had a very large background count rate and were masked. Calibration of the timing resolution of each channel was done using a 405 nm Picosecond Injection Laser (PiLas) PiL040SM by Advanced Laser Diode Systems [54] and a 660 nm Picosecond Pulsed Diode Laser (PDL 800-D) by PicoQuant [55]. The laser pulses were connected to an opal glass diffuser to illuminate the entire MCP-PMT plane. Calibrations were performed both daily and any time the geometric configuration was changed.

Data were taken for approximately 30 days, accumulating roughly 500 million triggers. Both bar and plate radiator geometries were tested with several optical components. Scans in polar angle between 20° and 150° were taken for many configurations. Scans in momentum up to 10 GeV/c were taken for select angles and geometries. As this was an opportunistic run for the EIC group, data taking was based on the needs of the PANDA DIRC group. They require separation power information for pion/kaon at 3.5 GeV/c, but since the T9 beam had a very small amount of kaons it was decided to instead study pion/proton separation at 7 GeV/c as the difference in Cherenkov angle for both cases is roughly 8 mrad. The results presented below will be from data taken with a bar radiator, 3-layer spherical lens, 7 GeV/c hadron-rich beam, and polar angles from 20° - 150°.

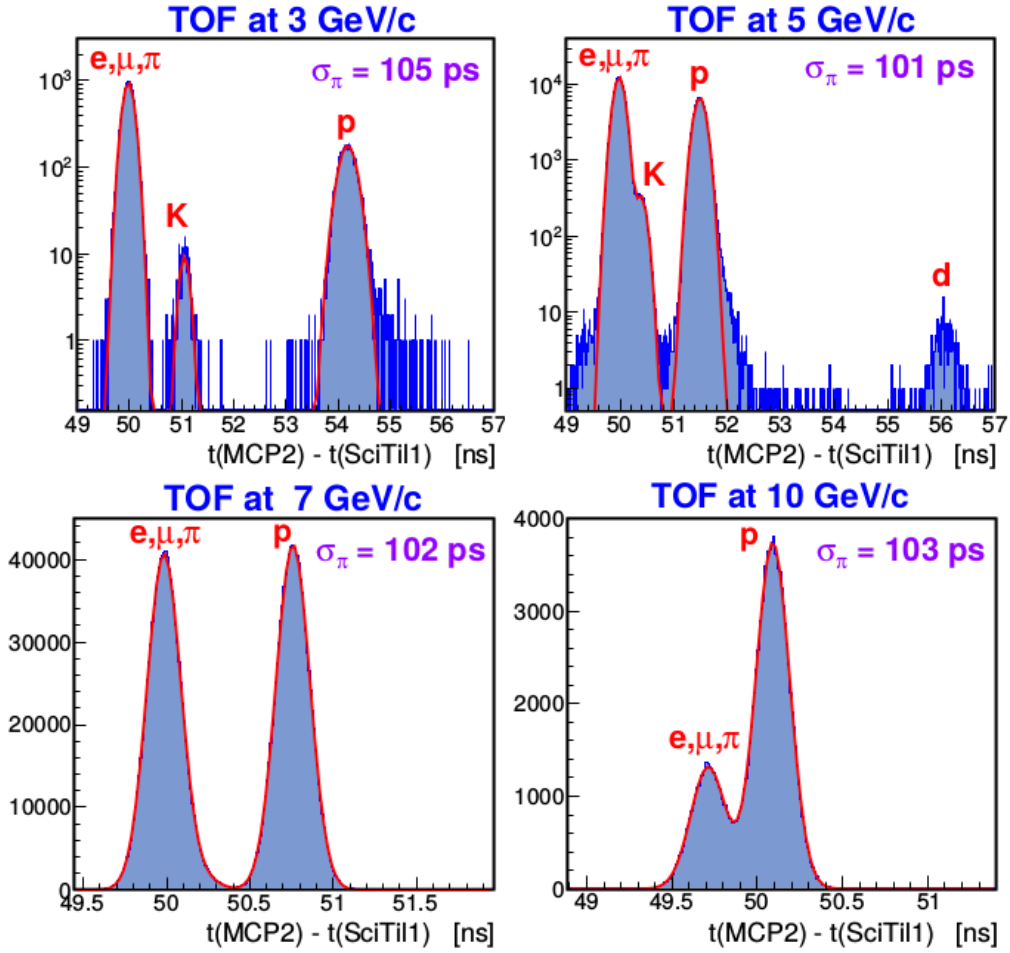

FIG. 54: Time-of-flight (TOF) particle tagging for 3, 5, 7, and 10 GeV/c beam momentum with a 29 m separation between TOF stations (MCP2 and SciTil1) each with between 50-80 ps time resolution. As a side note: it is immediately obvious that a simple TOF system as a solution to PID in the limited space of the barrel region of an EIC is infeasible as even at 5 GeV/c momentum the signal between pions and kaons are difficult to separate, and at 10 GeV/c it is neigh-impossible even with a 29 m separation between stations.

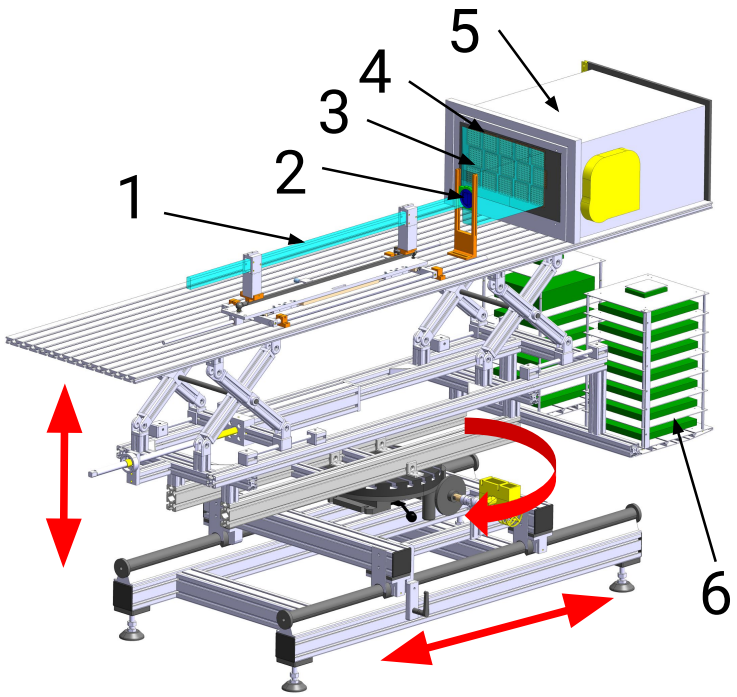

FIG. 55: CAD drawing of the 2015 PANDA DIRC prototype setup [50]. The radiator (1), optics (2), expansion volume (3), 3×5 array of MCP-PMTs (4), readout (5), and TRB units (6) are supported by an aluminum frame that can move in two directions and rotate, as indicated by the red arrows.

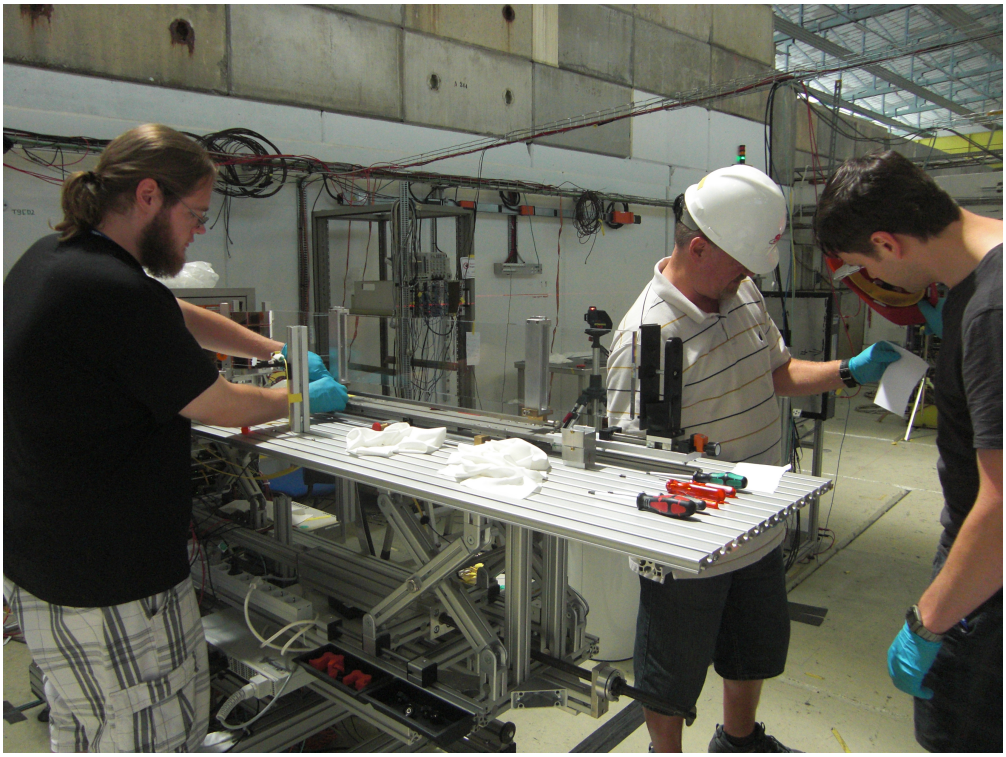

FIG. 56: Plate radiator being adjusted by micrometer screws using the Bosch Dual Plane Laser as a guide. When the light reflected off of the radiator lined up with the incoming beam from the laser on the white paper in both the horizontal and vertical directions the radiator was aligned with the beam line. Photo taken by, and used with permission from Dr. Grzegorz Kalicy.

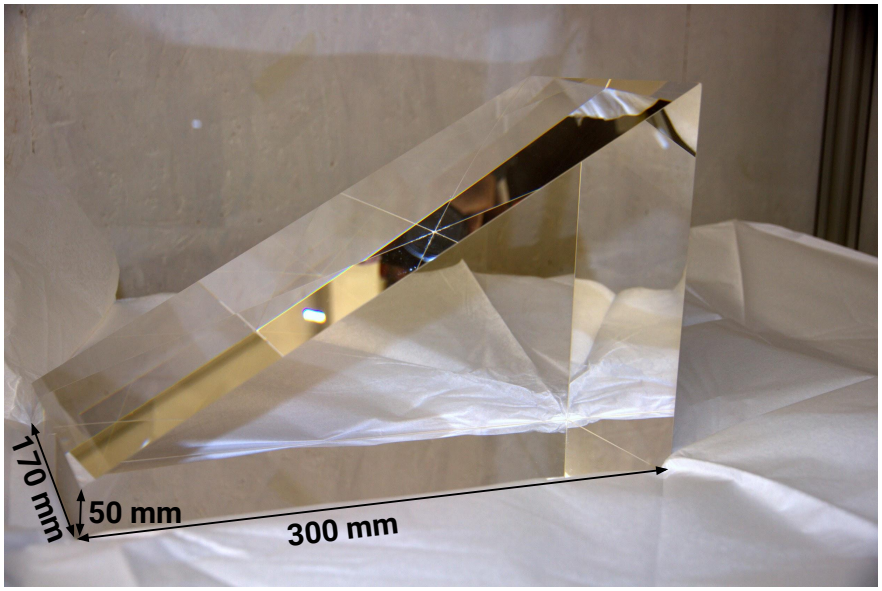

FIG. 57: Picture of the 30° prism expansion volume used in the 2015 test beam [50].

6.2 PROTOTYPE SIMULATION

The accurate recreation of a DIRC detector in simulation is crucial for data analysis as it allows for the generation of the look-up-tables (LUTs) for geometric reconstruction, as well as a reference for the hit patterns [1] of the real-time monitoring system in the case of the 2015 CERN test beam campaign. A standalone GEANT4 simulation package was used for the CERN test beam, from which the EIC DIRC simulation in Chapter 4 was produced. Material properties for fused silica, NLaK33, the mirror, the optical grease, and the MCP-PMTs were included. The timing resolution of the simulation was based on findings of the laser calibration data and set to be 200 ps. For each configuration of the prototype the geometry for each element (e.g. relative positioning for the bar to the lens and prism) were adjusted to the values carefully measured while changing configurations.

Also included in the simulation is the quantum efficiency (QE) of the MCP-PMTs. Each MCP-PMT was scanned for QE and gain uniformity with a 372 nm laser pulser at Erlangen University. The mappings of QE were normalized to MCP-PMT 10 (when counting from bottom to top and left to right, starting at 0) and used as relative QE maps in the simulation (Figure 58 top). To get the absolute QE for each pixel a scan was done of the QE as a function of photon wavelength (Figure 58 bottom). The QE in the simulation was calculated by multiplying the relative QE of each pixel by the QE corresponding to the wavelength of the photon being detected by the pixel in the simulation.

Figure 59a shows an example of one simulated proton track with 7 GeV/c momentum (red) at a polar angle of 125° traversing a bar radiator with the 3-layer lens focusing, and producing Cherenkov photons (yellow). Figure 59b is the accumulated hit pattern on the MCP-PMTs of 10,000 identical protons with the same configuration as in (a). Figure 59c is the accumulated hit pattern of 10,000 tagged proton events in the test beam data with 7 GeV/c beam momentum, 125° polar angle, and the bar radiator and 3-layer lens configuration. The simulation very nicely reproduces the test beam hit pattern, giving a good indication that the simulation has the proper positioning of all the components.

[1] For the purposes of this document a "hit" or "photon" refers to a signal from a single pixel in an MCP-PMT. However because of an irreducible background it cannot be said for certain which signals are from true Cherenkov photons. What is truely measured are photo-electrons.

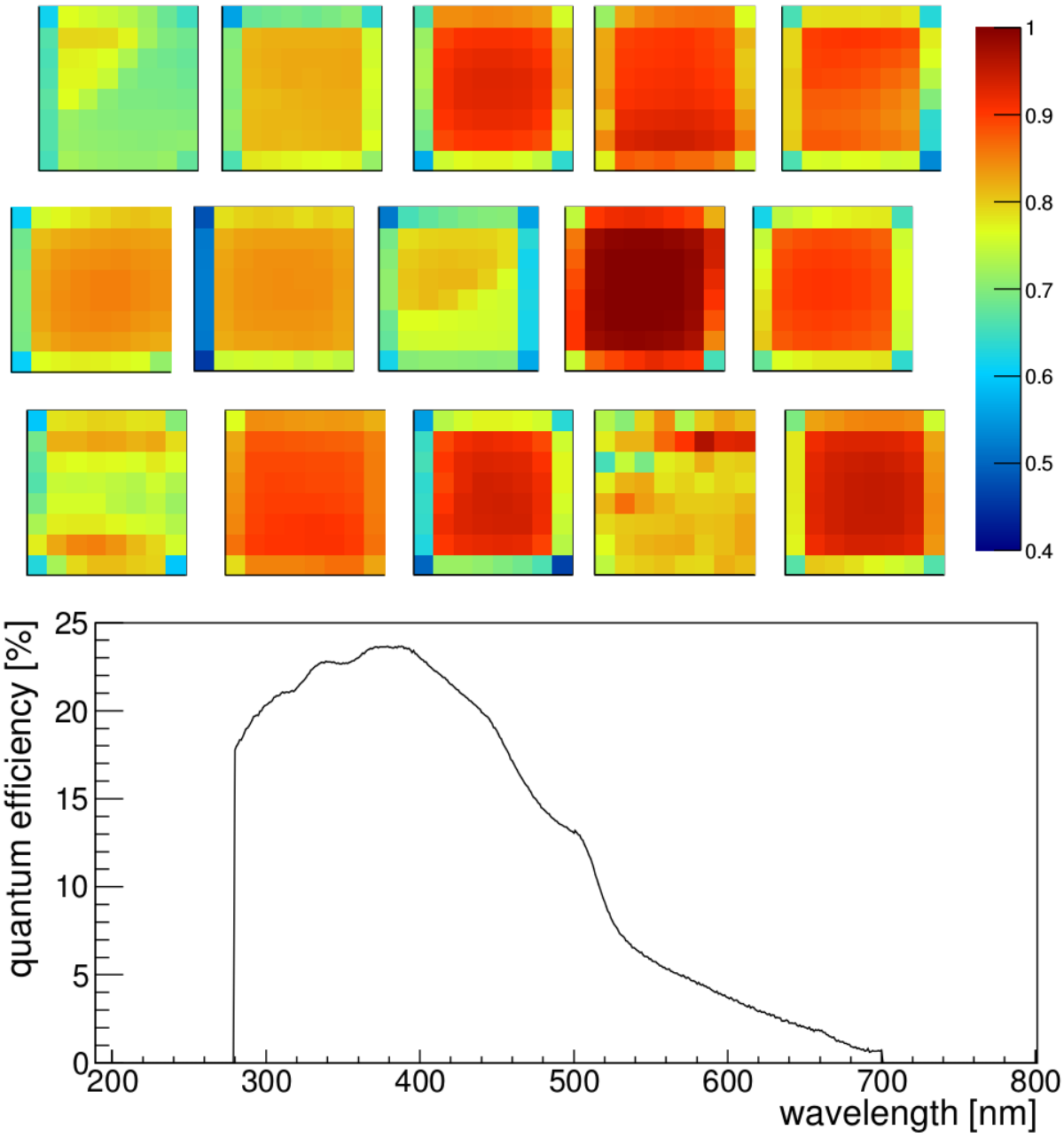

FIG. 58: The absolute and relative quantum efficiency of each MCP-PMT pixel. Channel-by-channel map of the relative quantum efficiency (QE) of each 6×6 mm^2 pixel of each MCP-PMT (64 pixels per MCP-PMT) used in the simulation of the 2015 test beam prototype (top). Absolute QE values in the simulation are the product of the channel-by-channel values with the wavelength dependent QE of a Planacon XP85012 MCP-PMT (bottom).

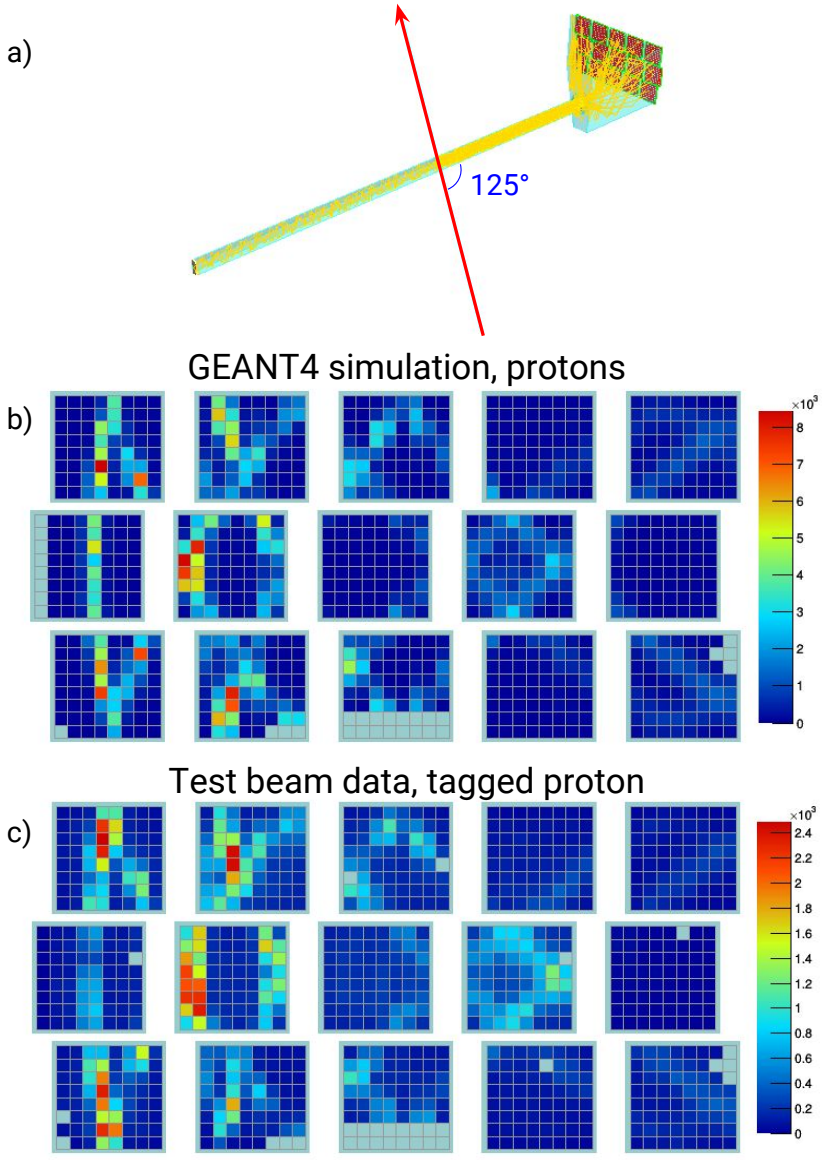

FIG. 59: Comparison of prototype data and GEANT4 simulation. a) Shows a visualization of the GEANT4 simulation of a single 7 GeV/c proton (red) traveling through the 2015 prototype with a bar radiator at a polar angle of 125°, b) is the accumulated hit pattern of 10,000 identical protons from simulation, and c) is the accumulated hit pattern of 10,000 tagged proton tracks from test beam data at 7 GeV/c beam and 125° polar angle. The roughly half pixel discrepancy in the position of the two hit patterns can be explained by the uncertainty in the absolute value of the polar angle during the test beam measurements.

6.3 DATA ANALYSIS

Several studies were done during the CERN 2015 test beam campaign using both a radiator bar and plate, five different focusing configurations, and a range of momentum. Some studies were used as test runs for calibration and debugging. Information on the main data studies are shown in Table 1.

Two studies were chosen for the analysis in this thesis based on geometric configuration (bar and 3-layer lens) and momentum (7 GeV/c): 151 and 158. Study 151 is the primary data set because of its larger range in polar angle, while study 158 is used for comparison and error evaluation. Each data set represents approximately 1 day of beam.

6.3.1 EVENT SELECTION

The prototype data taken were stored in the list mode data format of the HADES DAQ system prototcol [56] and converted offline into the CERN ROOT data format [57] for analysis. The DAQ was started by a signal from Trigger 1, and events were required to have signals in Trigger 1, Trigger 2, and both TOF counters to ensure a well-defined beam spot and valid π/p tagging from the TOF system. The veto counters were also required in event selection, but later found to be unnecessary for constraining the beam spot.

Hits were selected in a time window of ± 40 ns relative to the Trigger 1 time. Channels with large electronics noise above 1 MHz and one defective PADIWA card were masked, with the same masking scheme applied to the simulation. Events with 5 or fewer MCP-PMT hits were also excluded from reconstruction due to lack of statistics for the reconstruction. It is also worth noting that, though the QE of the MCP-PMTs is more or less uniform, MCP-PMTs 12, 13, and 14 had poor performance during the test run due to electronics issues.

As mentioned previously the timing difference between the two TOF stations allowed for tagging an event as either pion or proton. Figure 60 shows the TOF time distributions for 5 GeV/c (top) and 7 GeV/c (bottom) beam momenta. These distributions were fitted with Gaussian functions near the proton and pion peaks and a $\pm 2\sigma$ window around the peaks was used for selection (dashed lines).

The timing of the hits in the MCP-PMTs were also constrained. Based on the orientation of the detector in the beam the time for the photon to propagate can be calculated based

on the total bar path traveled (Z), using Figure 61a and

$$Z = \begin{cases} z_0 + \Delta z & \text{direct photons} \\ 2L - z_0 - \Delta z & \text{reflected photons} \end{cases} \tag{8}$$
$$\Delta z = -\cot(\alpha) \times \left[D_2 + D_1 \times \cot\left(135 - \frac{\alpha}{2}\right) \right]$$

where L is the total length of the radiator, z_0 is the nominal perpendicular distance between the particle beam and the end of the radiator, D_1 is the distance from the pivot point of the radiator to the particle beam, D_2 is the distance from the pivot point to the radiator, and α is the polar angle. Comparing the difference between the calculated expected arrival time and the actual arrival time of the photons gives a time difference distribution, shown in Figure 61b. In simulation it is to possible to exclude times associated with incorrect reconstructed paths from the LUT. Using this time distribution from only correct simulated paths it was determined that a time difference cut of ± 1 ns was sufficient across all polar angles for geometric reconstruction.

6.3.2 GEOMETRIC RECONSTRUCTION

The geometric reconstruction for the CERN 2015 test beam data was done in much the same manner as that described in Chapter 4, however, three corrections were applied to the test beam data to improve resolution and overall performance: a correction to account for charge sharing between pixels in the MCP-PMTs, a per-MCP-PMT correction to the reconstructed mean θ_C for each polar angle, and a subtraction of the simulated path ambiguity background from beam data. Evaluation of the statistical and systematic uncertainties was also done for both simulation and beam data. Fitting of the main peak of the reconstructed Cherenkov angle was done in the same manner for both test beam data and simulation. Detailed information about the fitting for both protons and pions can be seen in Table 2 of Appendix A. Results for photon yield, SPR, and reconstructed mean θ_C are presented below.

Charge Sharing Correction

It was discovered that many events in the prototype data showed multiple adjacent MCP-PMT pixels firing in a single event. It is difficult to say with certainty if neighboring firing pixels, such as the example shown in Figure 62a, fired independently or if charge sharing between the pixels occurred, effectively spreading the pixel's signal across multiple pixels.

Because the width of each pixel corresponds to roughly a 20 mrad spread in Cherenkov angle the results of reconstructing these clustered pixels with the standard averaged LUT resulted in wider than expected reconstructed Cherenkov angle distributions for the prototype data.

The solution was to modify the LUT to reconstruct the position of the photon not from the center of each pixel, but towards an edge, weighted by the position of neighboring firing pixels. Each pixel is subdivided into 9 sections in the LUT, as in Figure 62b. The reconstruction algorithm first determines if and where adjacent firing pixels are located for each hit and then reconstructs the Cherenkov angle at the center of the section most heavily weighted. Figure 63 shows the effect of this charge sharing correction for simulation (top) and experimental data (bottom) at 90° polar angle. As was expected, the simulation, which does not include charge sharing, was largely unaffected. In the prototype data, however, the correction served to narrow the reconstructed Cherenkov angle peak and reduce background contributions.

Per-MCP-PMT θ_C Correction

The fitted mean of the reconstructed Cherenkov angle from geometric reconstruction showed a non-constant value across the prototype polar angle range for both simulation and experimental data. To correct for this non-constant shift a per-MCP-PMT θ_C correction was implemented in the reconstruction. For a given polar angle and particle species the reconstructed Cherenkov angle for each MCP-PMT is fitted in the same manner as the full data set and a value for the Cherenkov angle is extracted (see Figure 64). The difference between the extracted value and the true value define a shift that is then used to adjust the Cherenkov angle spectrum for each individual MCP-PMT. After corrections the mean Cherenkov angle is much more accurately reproduced, and even improves the SPR at the some polar angles. Figure 65 shows the results of the correction for the full range of polar angles.

Simulated Background Subtraction

Because the majority of the background signal for the reconstructed Cherenkov angle comes from irreducible photon path ambiguities it would stand to reason that the ambiguity background simulated in GEANT4 would reasonably describe the PANDA prototype background seen in the experimental data, assuming the geometry has been correctly recreated in GEANT4. Figure 66a shows a simulation of 1000 protons at 7 GeV/c and 125° polar angle along with the ambiguity background (i.e. the reconstructed Cherenkov angle coming from

incorrect prism ambiguities) and the reconstructed angles coming from true prism paths. Figure 66b shows the prototype data with the same configuration along with the simulated background and the background-subtracted data. Because of the nice description of the background from simulation, the background-subtracted prototype data shows a clear peak and minimal background. This method could prove to be very useful for and EIC DIRC as the already minimal geometric background (see Figure 28 as an example) could be nearly eliminated.

Evaluation of Uncertainties

Many factors were considered for both the statistical and systematic uncertainties associated with the geometric reconstruction method: internal file consistency [2], varying the fitting function and fit range found to be optimal for each polar angle, varying histogram binning, varying the timing cuts, and checking the stability of a given geometric configuration between studies 151 and 158. For each contribution to the error, multiple samples were taken and the RMS of the distribution for photon yield (where applicable), SPR, and mean θ_C were taken to be the associated error. Derived errors for tagged protons in both experimental data and simulation are shown in Tables 3 and 4 of Appendix B respectively.

Select polar angles were reconstructed for both studies 151 and 158 and compared (see Figures 67, 68, and 69). The difference in photon yield, SPR, and mean θ_C were all found to be very small compared to the contributions coming from other systematics (thus confirming that the CERN setup was very stable) and were not included in the final error bars, but are shown in Table 3 for completeness.

Results

Figure 70 shows the extracted photon yield for the CERN 2015 test beam data. The enhancement of the photon yield at 90 degrees for simulation compared to beam data can be understood by recalling that the MCP-PMTs at the base of the expansion volume (12, 13, and 14) had poor performance during the test beam and these sensors are where nearly 100% of the produced Cherenkov photons end up from a 90° polar angle track.

Figures 71 - 74 show the final results for the reconstructed mean θ_C of the CERN 2015 beam data and simulation for protons and pions both with and without per-MCP-PMT corrections and path ambiguity background subtraction. As per the design, the per-MCP-PMT correction gives a much cleaner separation between protons and pions while also shifting

[2]Taking 100 sets of 100 events and running the reconstruction analysis for each set as normal.

the simulation and beam data such that they are in good agreement both with each other and with the expected Cherenkov angle. The path ambiguity background subtraction, however, does not significantly improve the performance of the reconstructed θ_C in either case. This is to be expected in both cases as the distribution of the background under the simulated peak is typically flat. It should, however, show some improvement for the SPR.

Figures 75, 76, 77, 78, 79, 80, 81, and 82 show the final results for the SPR of the CERN 2015 beam data and simulation for protons and pions both with and without per-MCP-PMT corrections and path ambiguity background subtraction. Unlike the reconstructed Cherenkov angle, here the per-MCP-PMT correction has little effect on the extraction of the SPR. This result is somewhat counterintuitive as one would expect that shifting each MCP-PMT's θ_C spectrum separately to the correct value would naturally narrow the signal peak. This, however, does not seem to be the case for most polar angles. Utilizing the path ambiguity background subtraction, on the other hand, shows a significant improvement of the SPR for most polar angles. Overall the beam data and GEANT4 simulation are in fairly good agreement for most polar angles, and within an acceptable value for PID performance.

Figure 83 shows the proton/pion log-likelihood separation for both simulation and beam data for geometric reconstruction. The simulated separation power meets the 3σ performance expected by the PANDA DIRC group for a majority of the polar angle range. However, the beam data shows a much worse performance, dropping to around 1σ for near perpendicular angles. This can most

Figure 84 shows the PID and misidentification (MisID) probability for protons (e.g. the MisID for protons shows the probability of a proton to be misidentified as a pion) as a function of polar angle for geometric reconstruction. MisID is calculated by taking the integral of the Gaussian fit from the crossing of the two curves (shown with the red circle) out to the tail of the distribution and dividing by the total integral of the curve. The PID probability is then 1-MisID.

TABLE 1: Studies made during the 2015 CERN test beam campaign, including geometric configuration, momentum, and number of data points taken.

Study ID	Radiator	Lens	Momentum (GeV/c)	Data points
150	bar	2-layer spherical	7	34
151	bar	3-layer spherical	7	46
152	plate	no lens	7	28
153	plate	2-layer cylindrical	7	29
154	bar	1-layer air gap	7	44
155	bar	1-layer air gap	7	17
157	bar	2-layer cylindrical	7	43
158	bar	3-layer spherical	7	15
159	bar	no lens	7	28
160	bar	3-layer spherical	5	47
161	plate	no lens	5	29
162	plate	2-layer cylindrical	5	29
170	bar	3-layer spherical	momentum scan	9
171	plate	no lens	momentum scan	8
173	plate	2-layer cylindrical	momentum scan	8
174	bar	1-layer air gap	momentum scan	8
179	bar	no lens	momentum scan	9

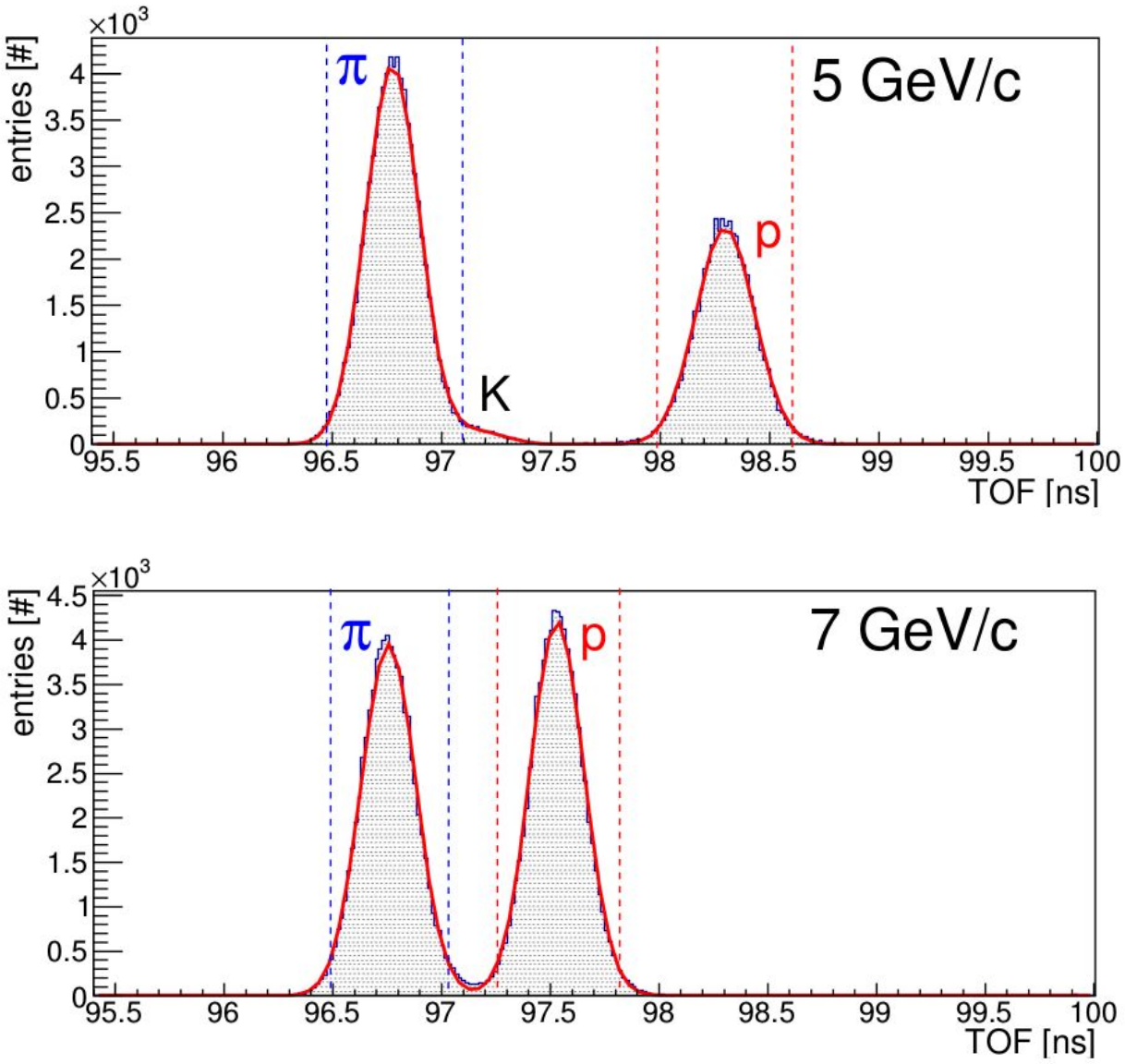

FIG. 60: Time difference between the two TOF stations for beam momenta of 5 GeV/c (top) and 7 GeV/c (bottom). The peaks were fitted and a $\pm 2\sigma$ selection window was taken (dashed lines).

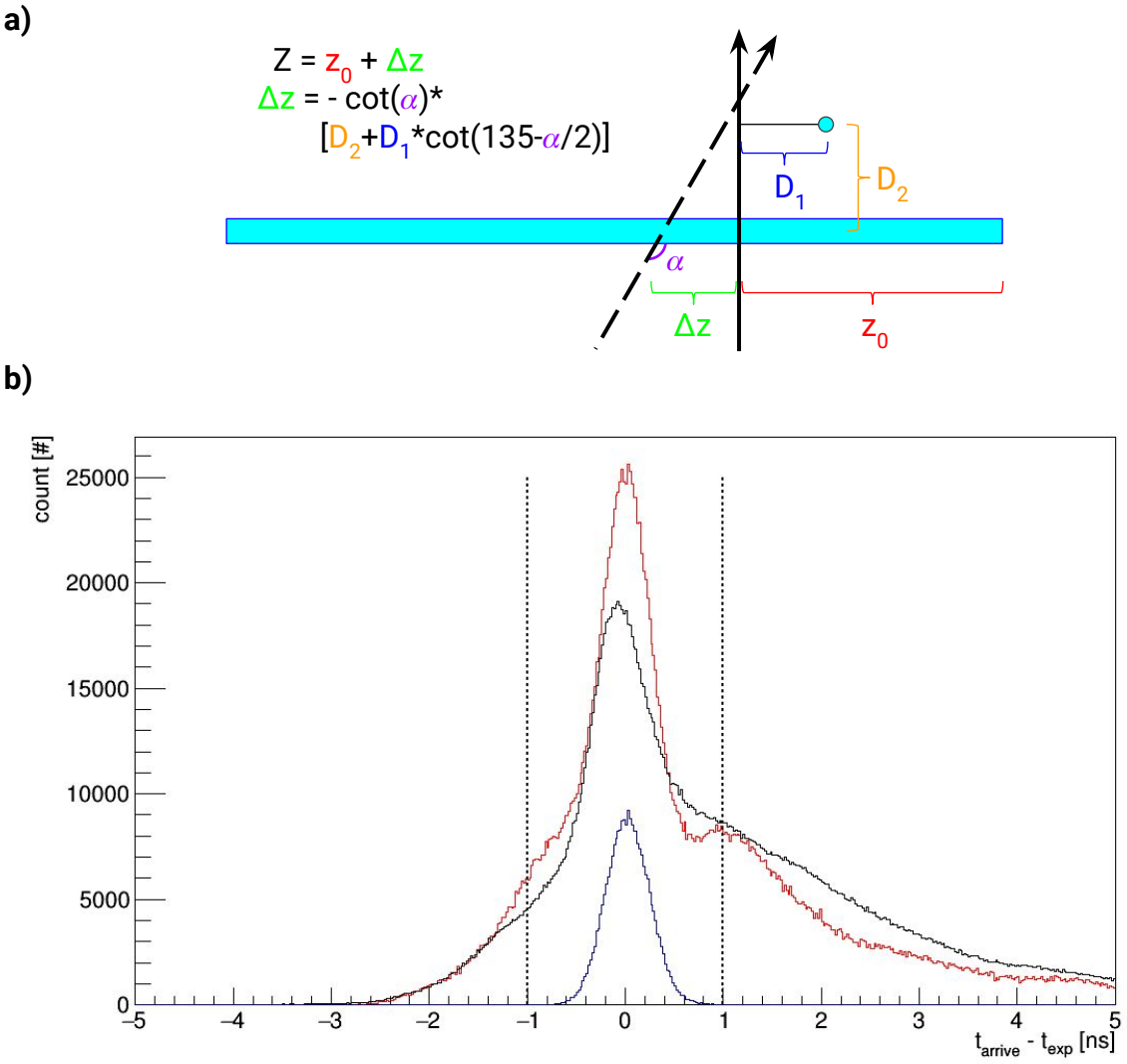

FIG. 61: A visualization of the timing difference used for data analysis. a) Illustration showing how total bar path length (Z) is calculated for the expected arrival time of photons based on distances from the pivot point (cyan circle) and particle beam (D_1),the pivot point to the radiator (D_2), nominal perpendicular distance between the beam and the end of the bar (z_0), and the polar angle (α). Note that in the case of b) Example time difference distribution of experimental data (black), full simulation (red), and simulation including only correct prism paths from the LUT (blue) for 125° polar angle. The dashed lines indicate the ±1 ns cut taken during analysis.

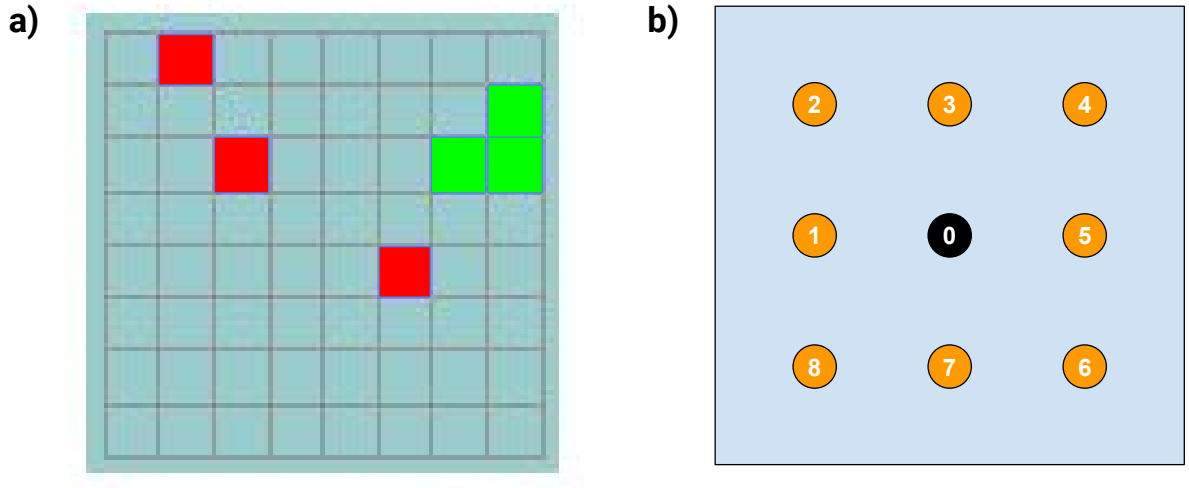

FIG. 62: A visualization of the charge sharing correction used during data analysis. a) A zoomed in view of a single MCP-PMT showing an example hit pattern from a single particle track. The 3 isolated pixels (red) have no neighboring hits. The 3 clustered hits (green), however, are adjacent to other firing pixels and thus it is hard to determine with timing alone if these are the result of a single photon from the bottom right pixel that resulted in charge sharing, 3 independent photons hitting all 3 pixels, or some combination of 2 photons hitting 2 of the pixels that resulted in charge sharing. To compensate for this uncertainty each pixel is subdivided, as in (b), into 9 regions such that the LUT will reconstruct the photon angle from different areas of the pixel. For the case of (a) the top pixel in the cluster would be reconstructed from point 7, the bottom left pixel from point 5, and the bottom right pixel from point 2, while the 3 isolated pixels would all be reconstructed from point 0.

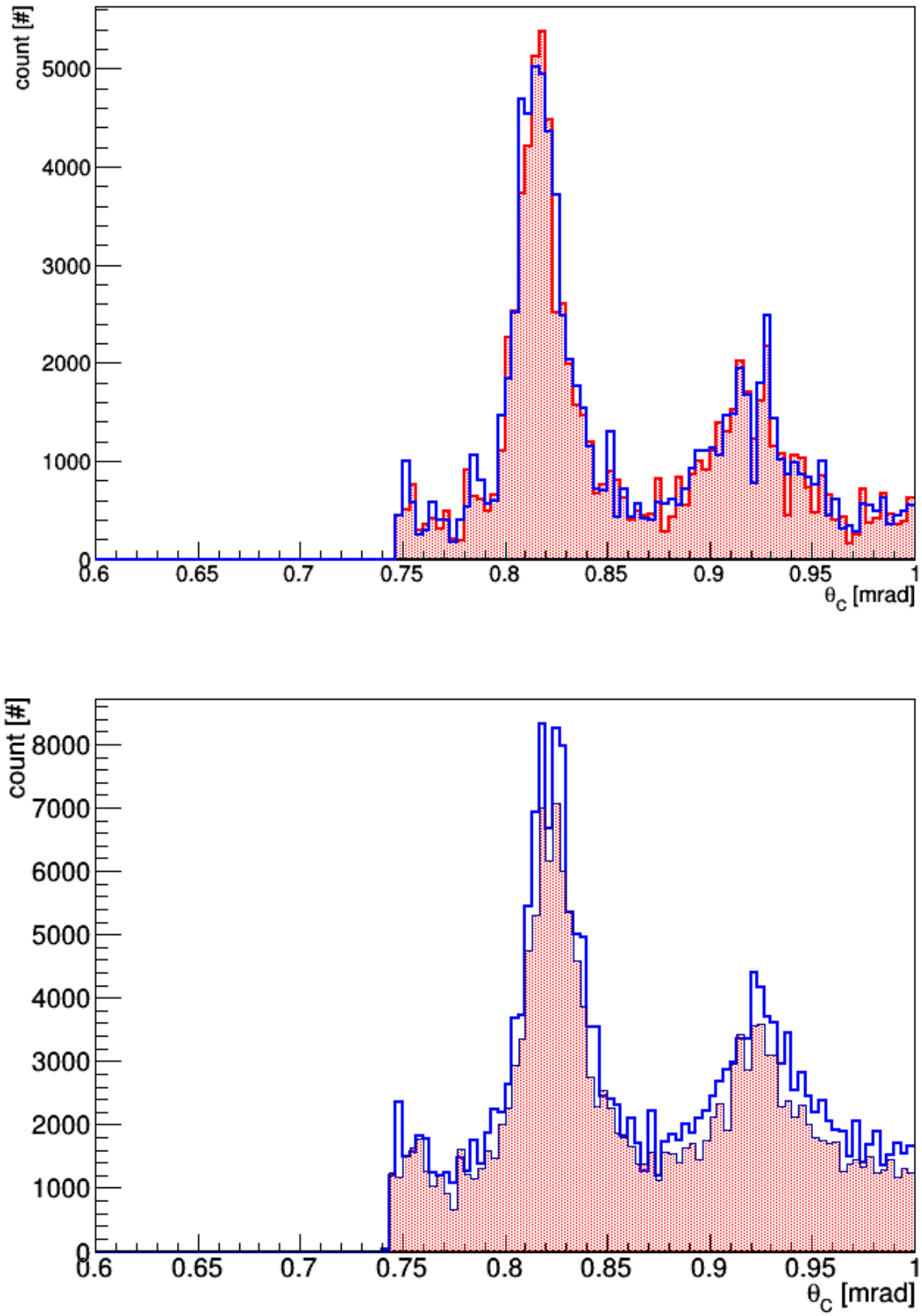

FIG. 63: Reconstructed Cherenkov angle of 7 GeV/c protons for simulation (top) and prototype data (bottom) for 90° polar angle using the standard LUT (blue) and the charge-sharing-corrected LUT (red). The simulation is largely unaffected, while in the data the peak has been narrowed and the background reduced.

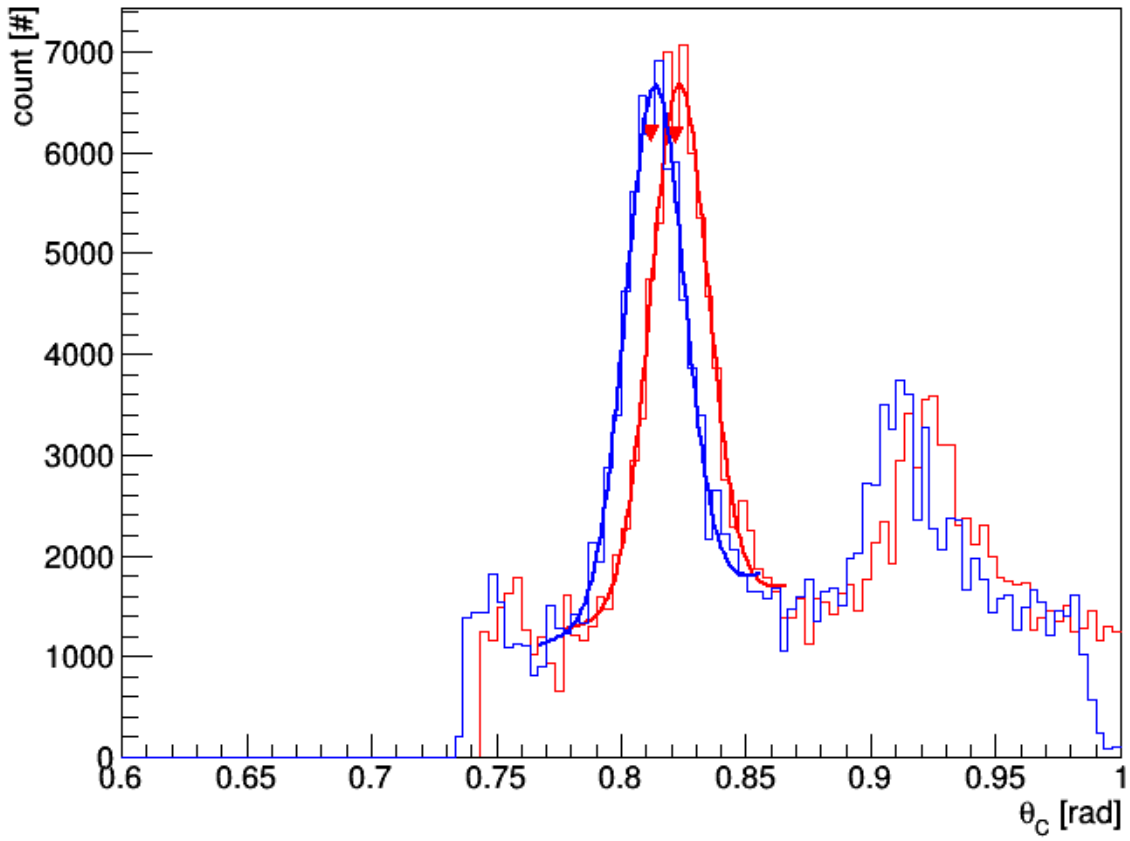

FIG. 64: Reconstructed θ_C at 90° polar angle before (red) and after (blue) per-MCP-PMT corrections. The uncorrected distribution has an SPR (the σ of the gaussian) of 10.9 mrad and a mean θ_C of 823.1 mrad, or 6.3 mrad away from the true value of 816.8 mrad for a 7 GeV/c proton. The corrected distribution has a steady SPR of 10.9 mrad and a mean of 813.4 mrad, which is only 3.4 mrad away from the true value.

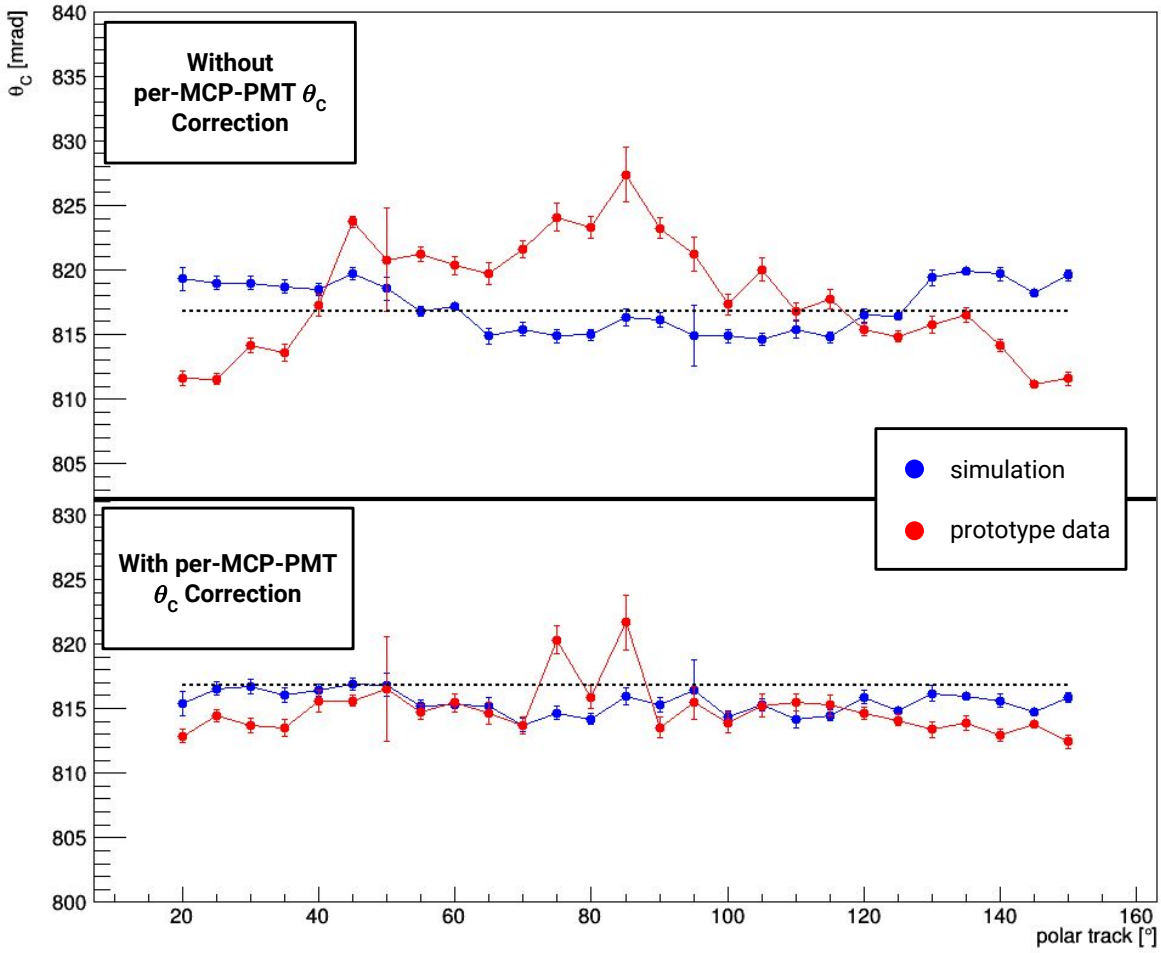

FIG. 65: The reconstructed mean θ_C from the PANDA prototype and simulation. Top: Reconstructed mean θ_C before applying per-MCP-PMT corrections for simulation (blue) and prototype data (red) for 7 GeV/c protons. The dashed line indicates the true Cherenkov angle for a 7 GeV/c proton of 816 mrad. Bottom: Reconstructed θ_C after applying corrections.

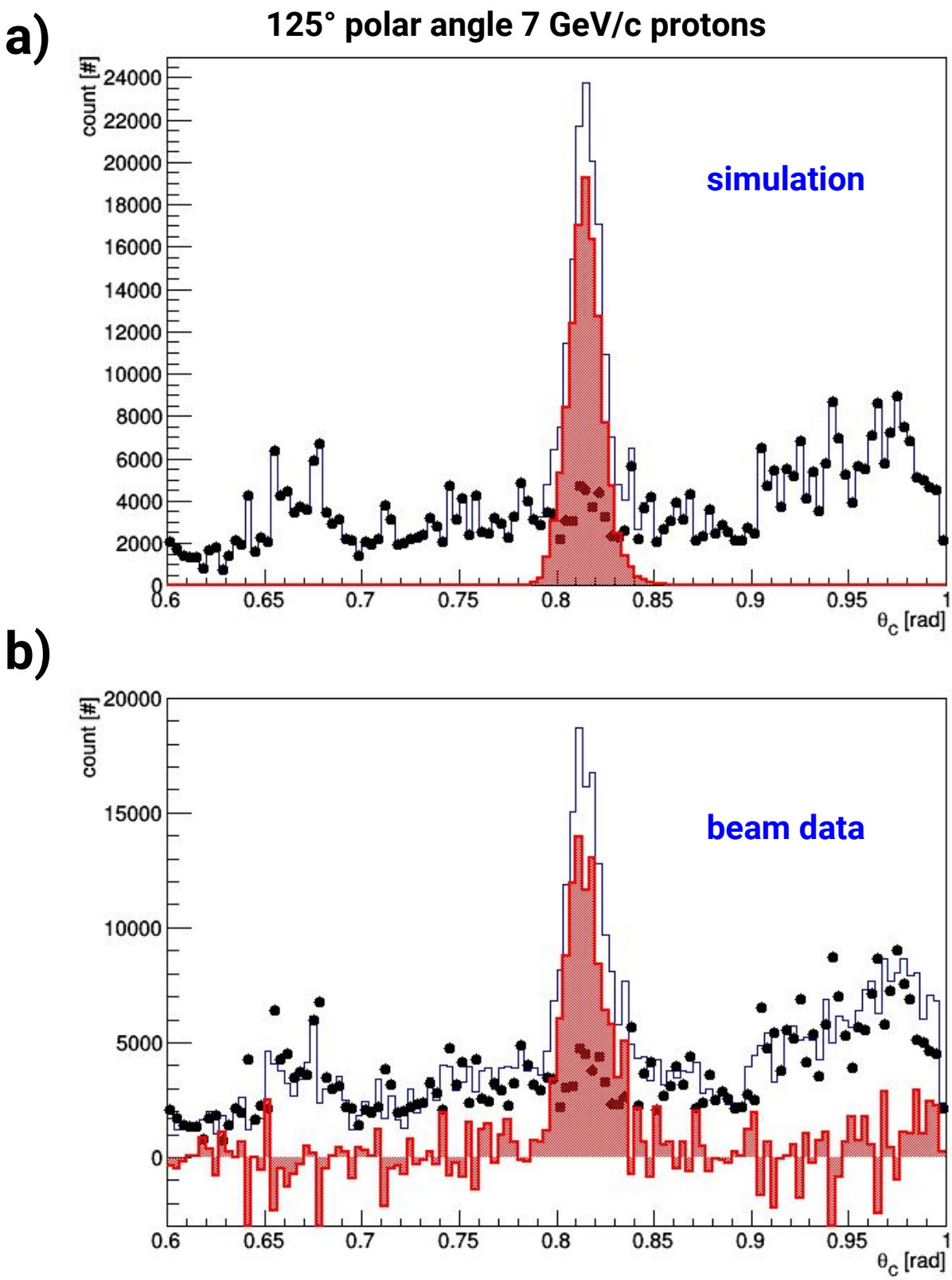

FIG. 66: An example of the background subtraction technique used during data analysis. a) The full reconstructed Cherenkov angle (blue line), reconstructed angle with only incorrect prism path ambiguities (black circles), and the reconstructed angle assuming only true prism paths (red histogram) for 125° polar angle protons from simulation. b) Beam data (blue line) with path ambiguity background from simulation (black circles, same as (a)). The red histogram is the difference between blue and black.

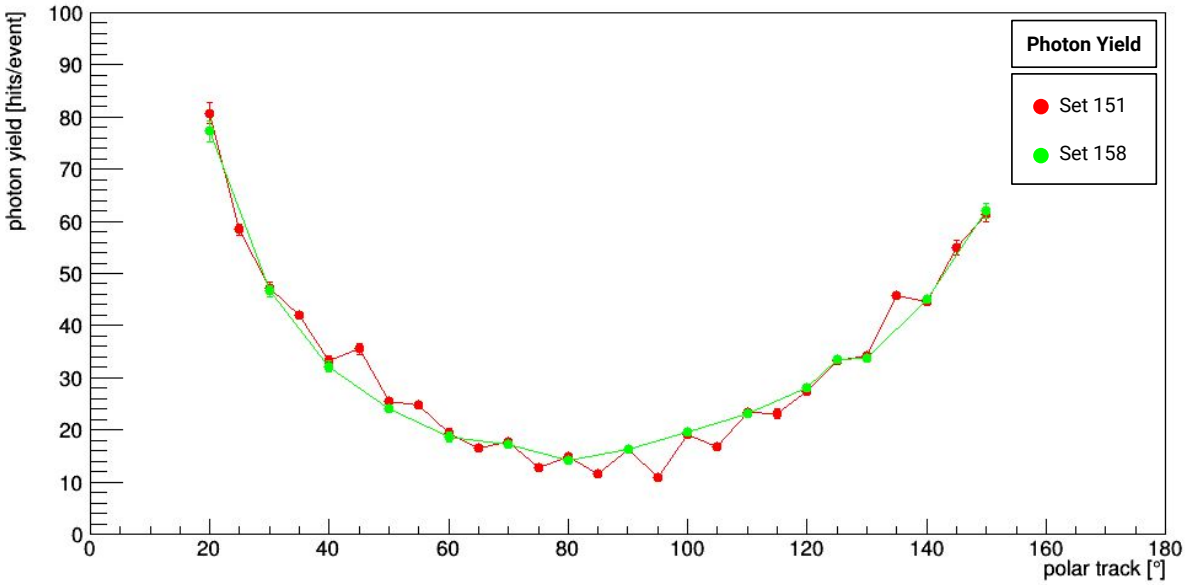

FIG. 67: Comparison of the extracted photon yield of studies 151 (red) and 158 (green). All common polar angles agree nicely.

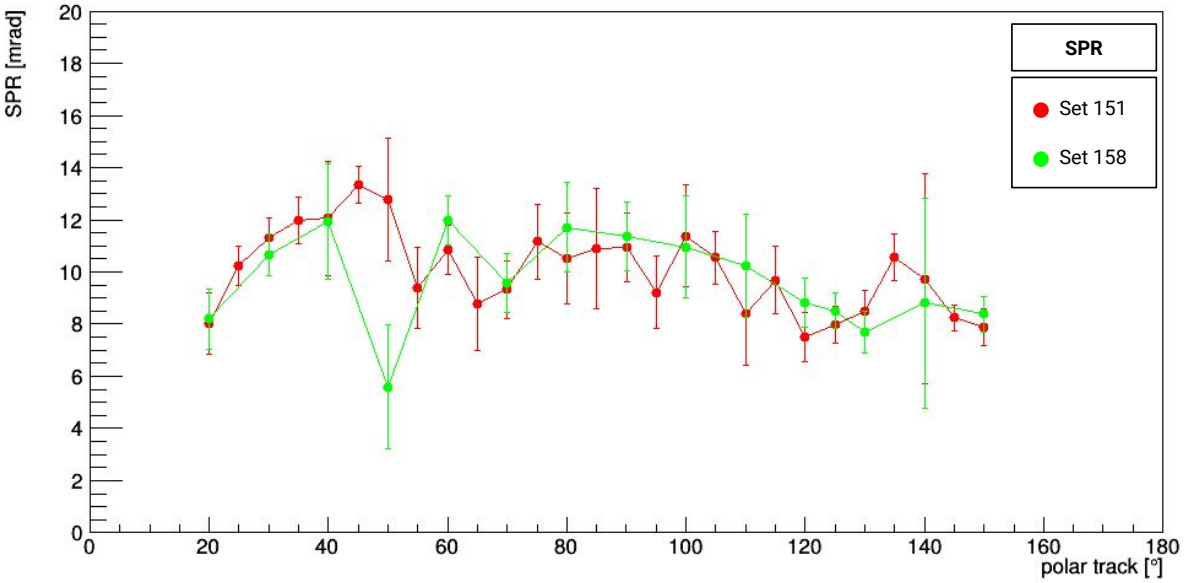

FIG. 68: Comparison of the extracted SPR of studies 151 (red) and 158 (green). All common polar angles other than 50° agree.

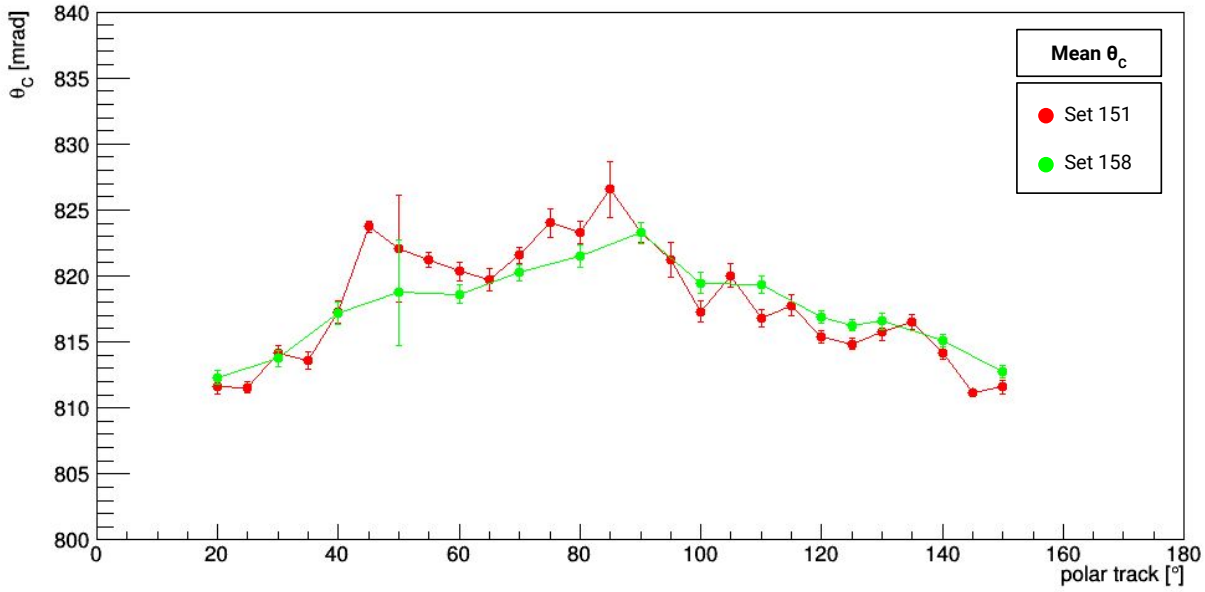

FIG. 69: Comparison of the reconstructed mean θ_C of studies 151 (red) and 158 (green). All common polar angles other than 50° agree.

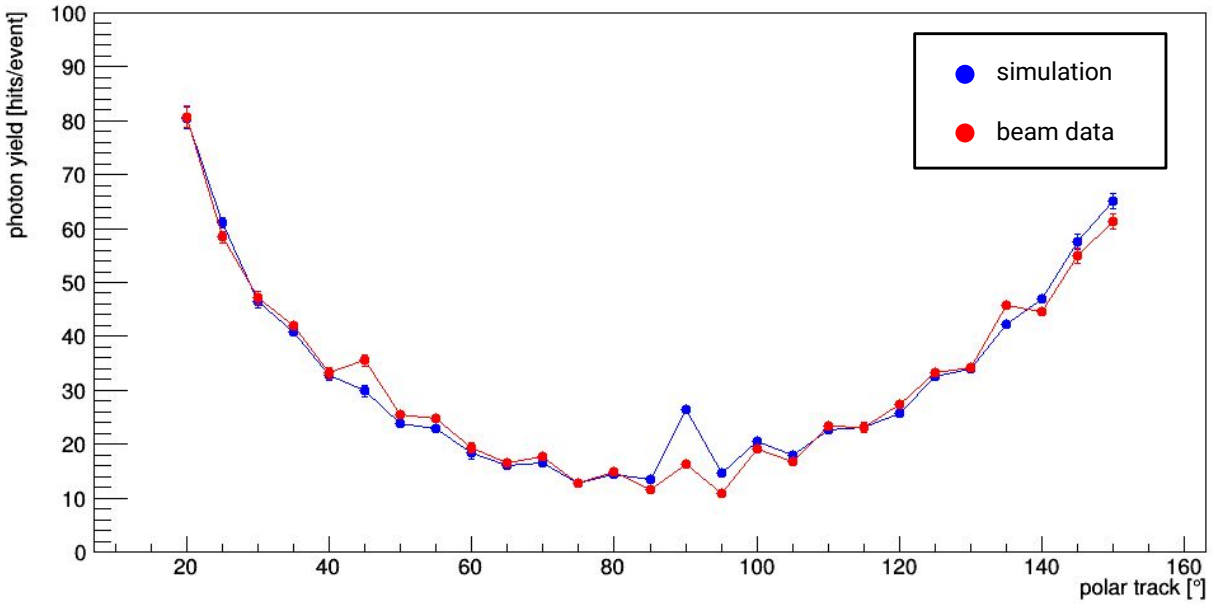

FIG. 70: Extracted photon yield from GEANT4 simulation (blue) and study 151 of the 2015 CERN test beam data.

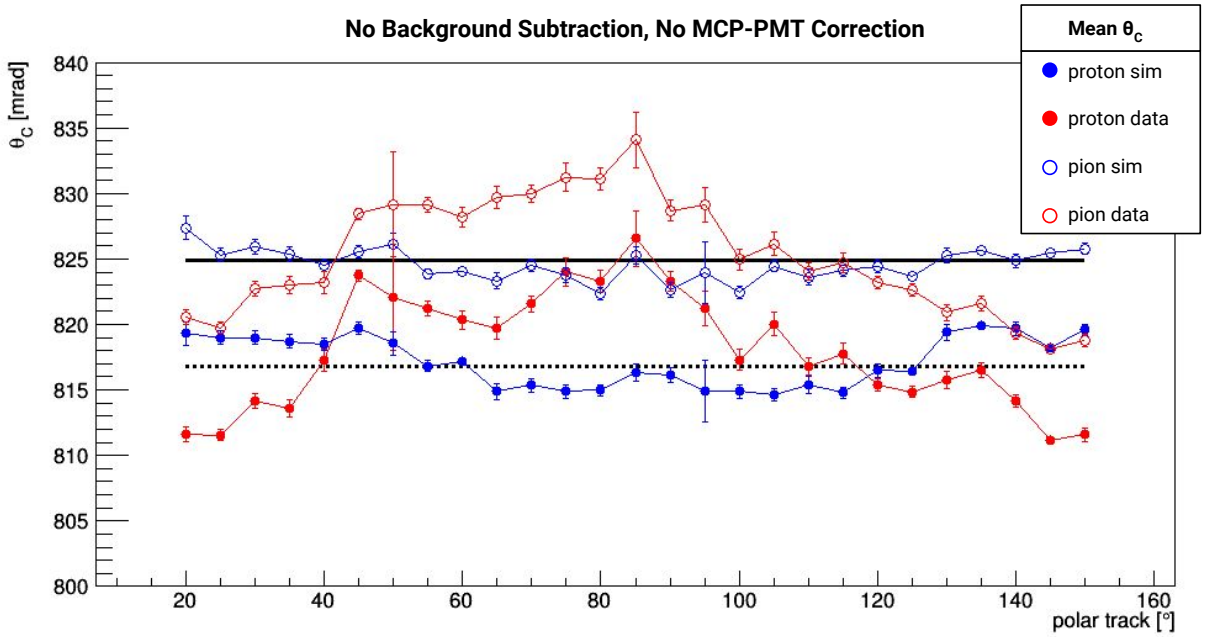

FIG. 71: Reconstructed mean θ_C with no background subtraction and no per-MCP-PMT correction from GEANT4 simulation (blue) and study 151 of the 2015 CERN test beam data (red) for protons (filled circles) and pions (open circles). The solid and dashed lines indicate the true Cherenkov angle for 7 GeV/c pions and protons respectively.

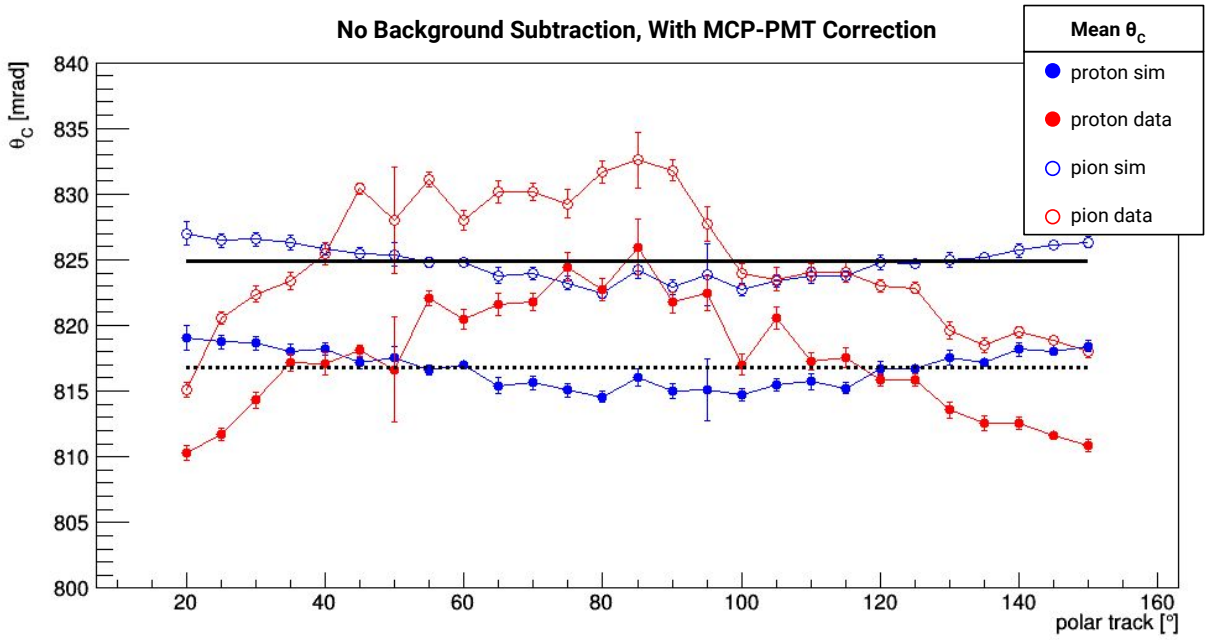

FIG. 72: Reconstructed mean θ_C with simulated background subtraction but no per-MCP-PMT correction from GEANT4 simulation (blue) and study 151 of the 2015 CERN test beam data (red) for protons (filled circles) and pions (open circles). The solid and dashed lines indicate the true Cherenkov angle for 7 GeV/c pions and protons respectively.

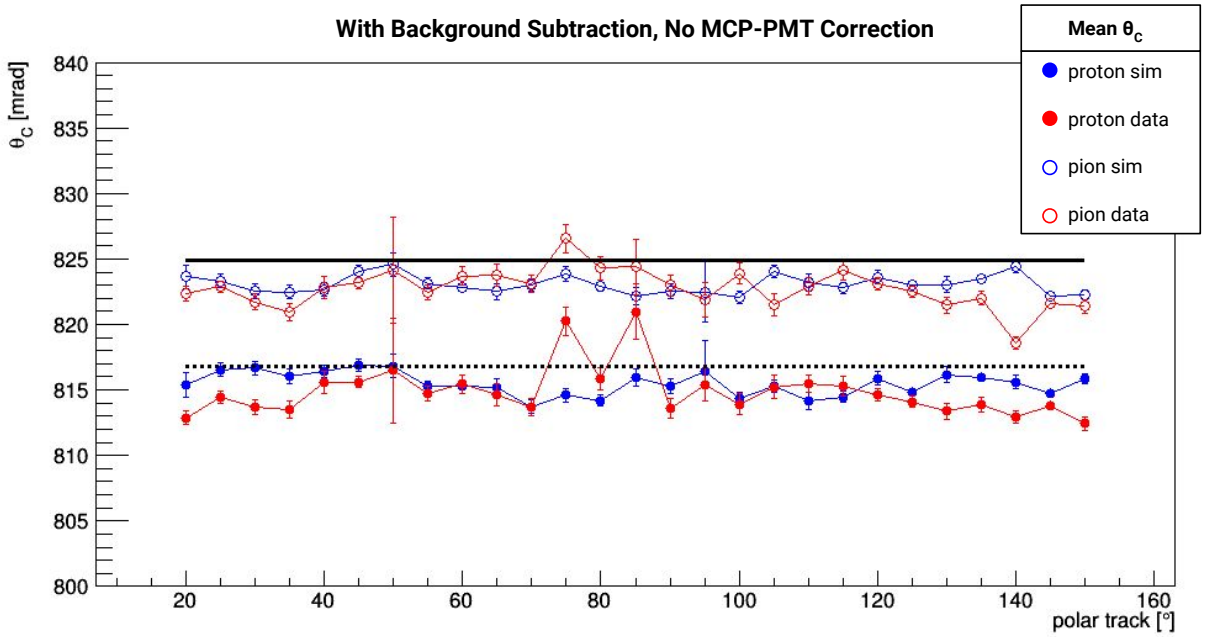

FIG. 73: Reconstructed mean θ_C with no background subtraction but using a per-MCP-PMT correction from GEANT4 simulation (blue) and study 151 of the 2015 CERN test beam data (red) for protons (filled circles) and pions (open circles). The solid and dashed lines indicate the true Cherenkov angle for 7 GeV/c pions and protons respectively.

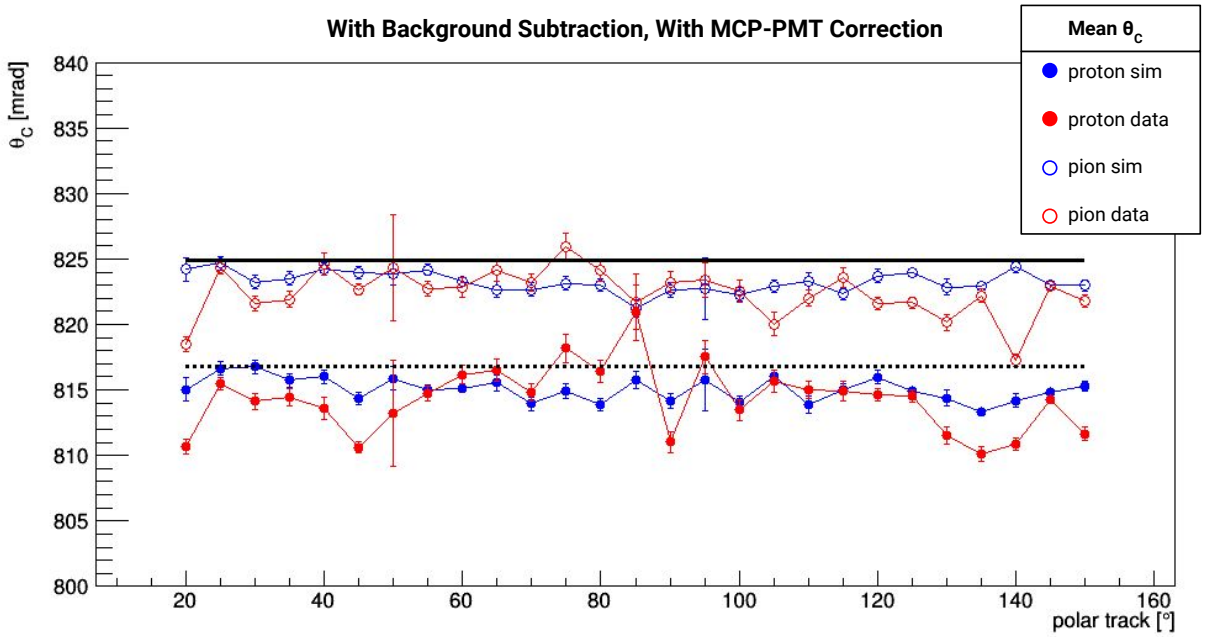

FIG. 74: Reconstructed mean θ_C with simulated background subtraction and using a per-MCP-PMT correction from GEANT4 simulation (blue) and study 151 of the 2015 CERN test beam data (red) for protons (filled circles) and pions (open circles). The solid and dashed lines indicate the true Cherenkov angle for 7 GeV/c pions and protons respectively.

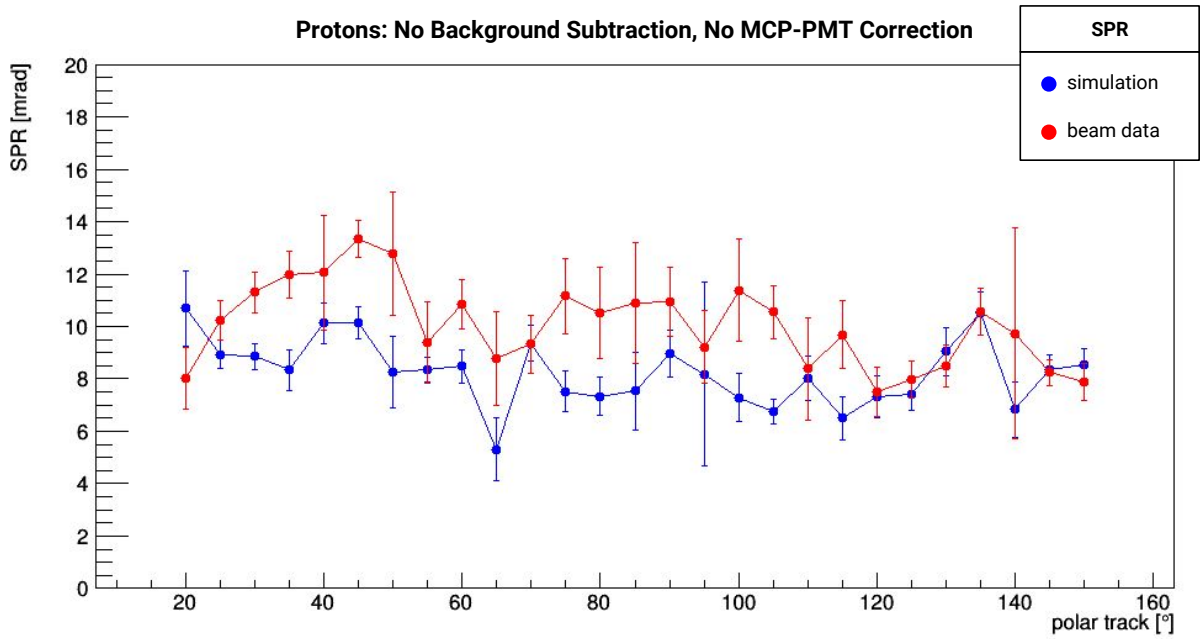

FIG. 75: Fitted SPR for proton-tagged events of study 151 of the CERN 2015 test beam data (red) and GEANT4 simulation (blue) without background subtraction or a per-MCP-PMT correction.

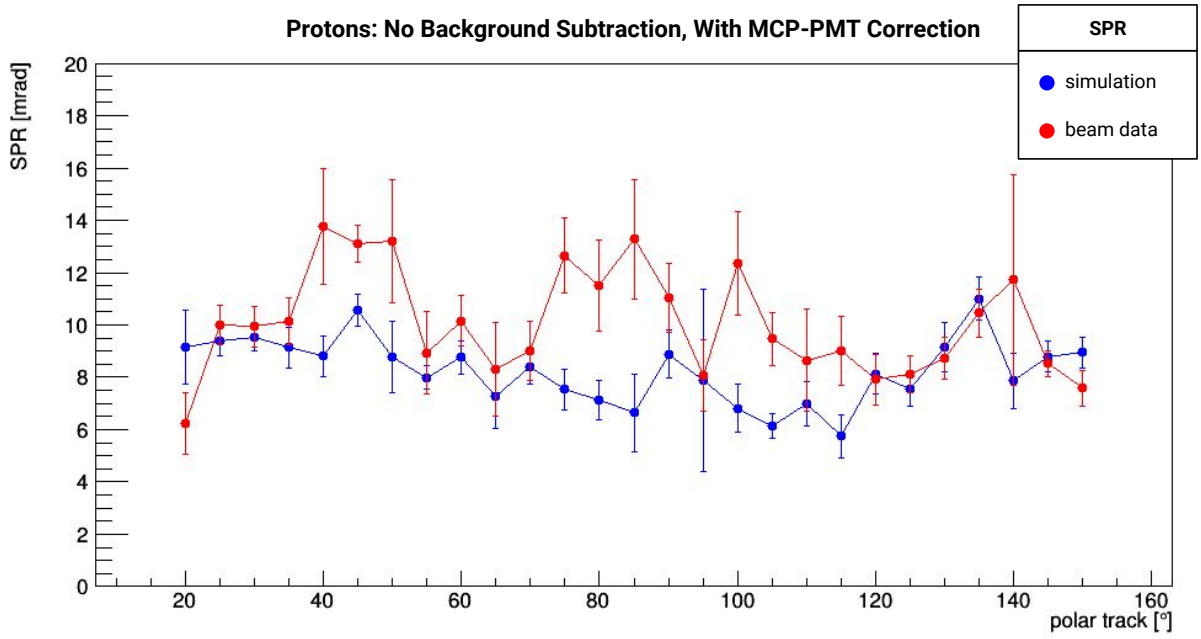

FIG. 76: Fitted SPR for proton-tagged events of study 151 of the CERN 2015 test beam data (red) and GEANT4 simulation (blue) without background subtraction and using a per-MCP-PMT correction.

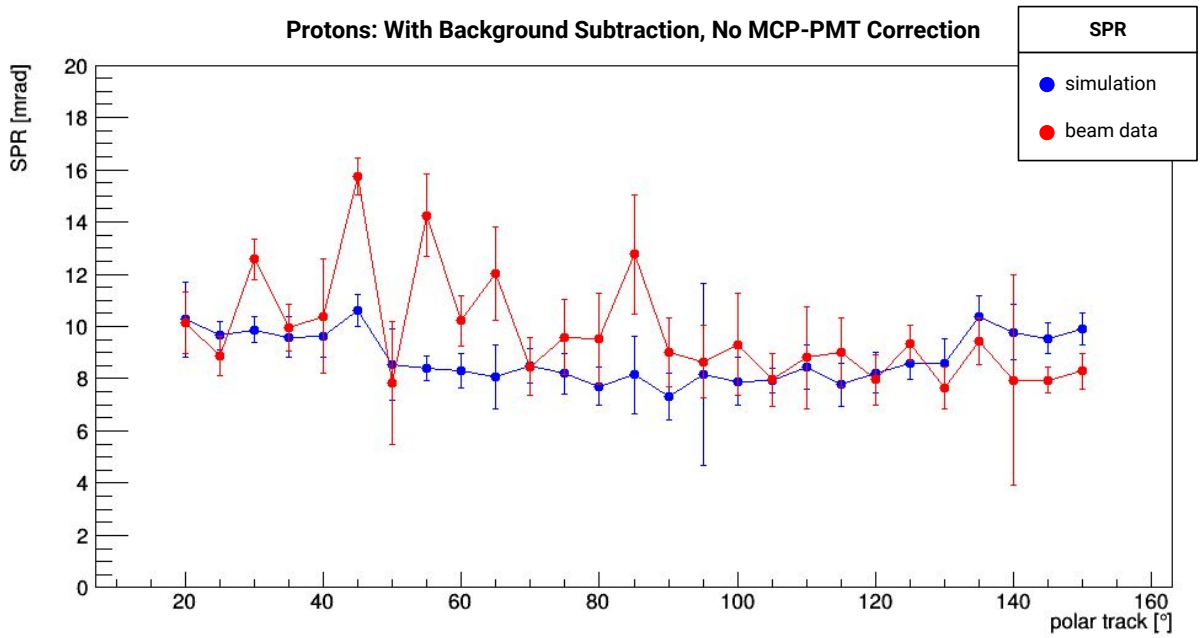

FIG. 77: Fitted SPR for proton-tagged events of study 151 of the CERN 2015 test beam data (red) and GEANT4 simulation (blue) using simulated background subtraction but no per-MCP-PMT correction.

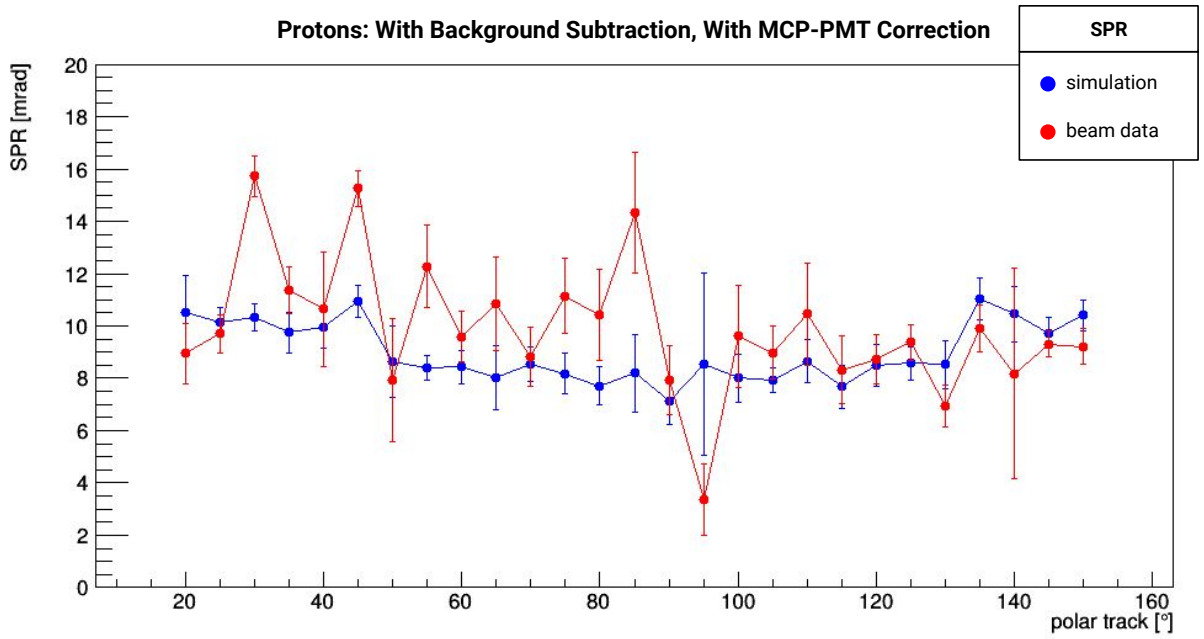

FIG. 78: Fitted SPR for proton-tagged events of study 151 of the CERN 2015 test beam data (red) and GEANT4 simulation (blue) using both simulated background subtraction and a per-MCP-PMT correction.

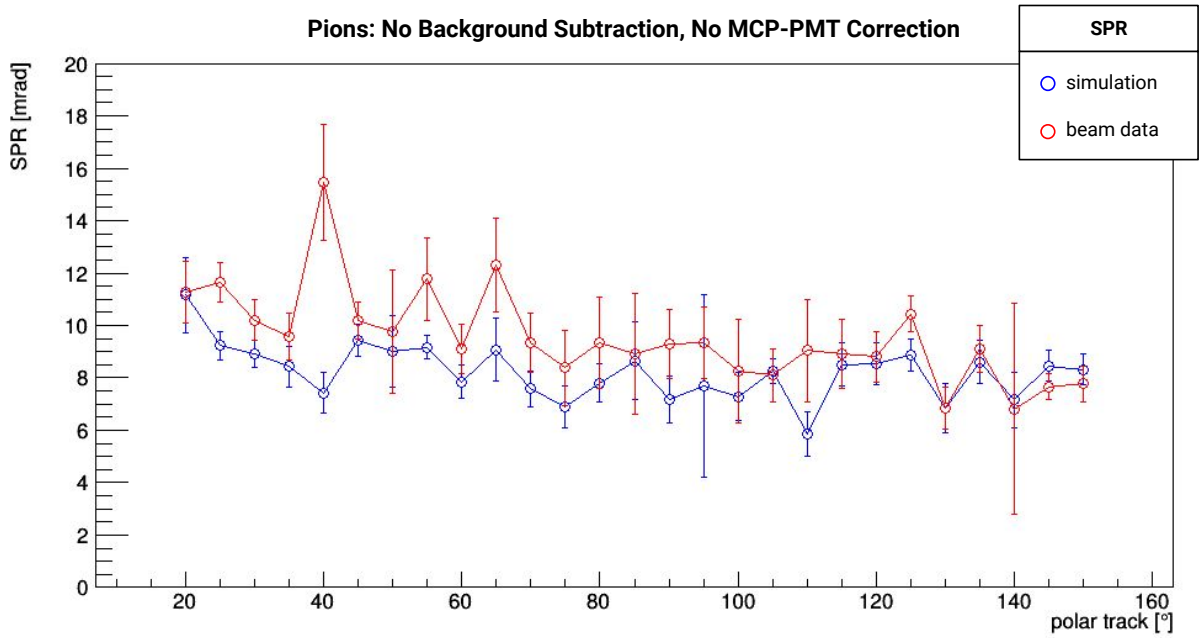

FIG. 79: Fitted SPR for pion-tagged events of study 151 of the CERN 2015 test beam data (red) and GEANT4 simulation (blue) without background subtraction or a per-MCP-PMT correction.

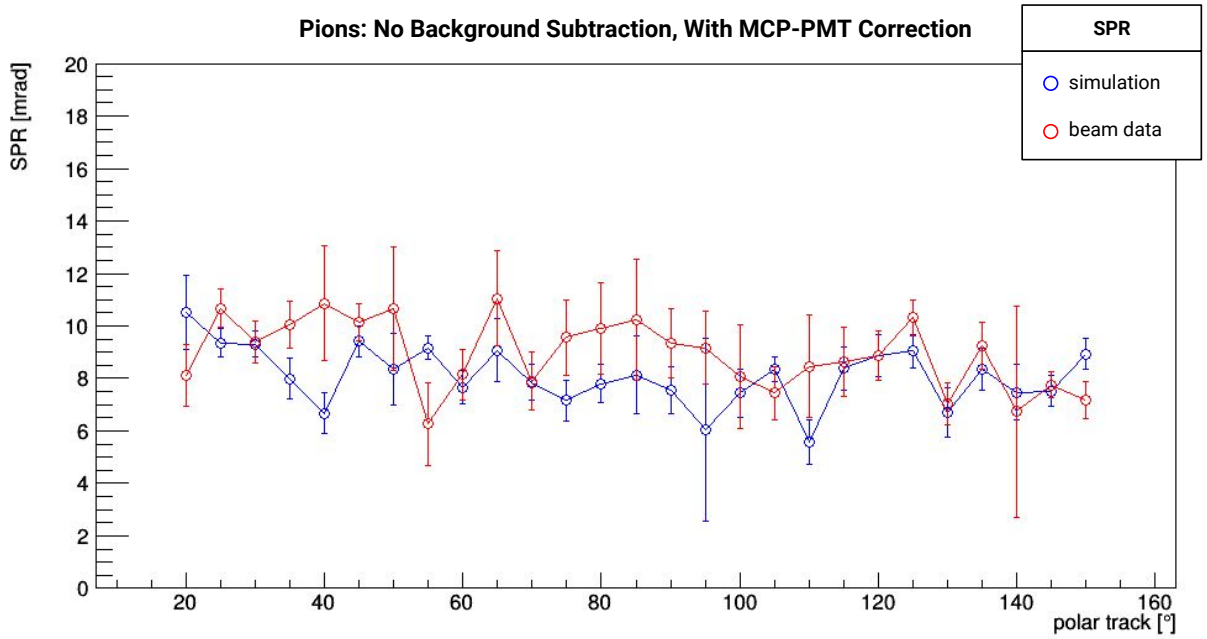

FIG. 80: Fitted SPR for pion-tagged events of study 151 of the CERN 2015 test beam data (red) and GEANT4 simulation (blue) without background subtraction and using a per-MCP-PMT correction.

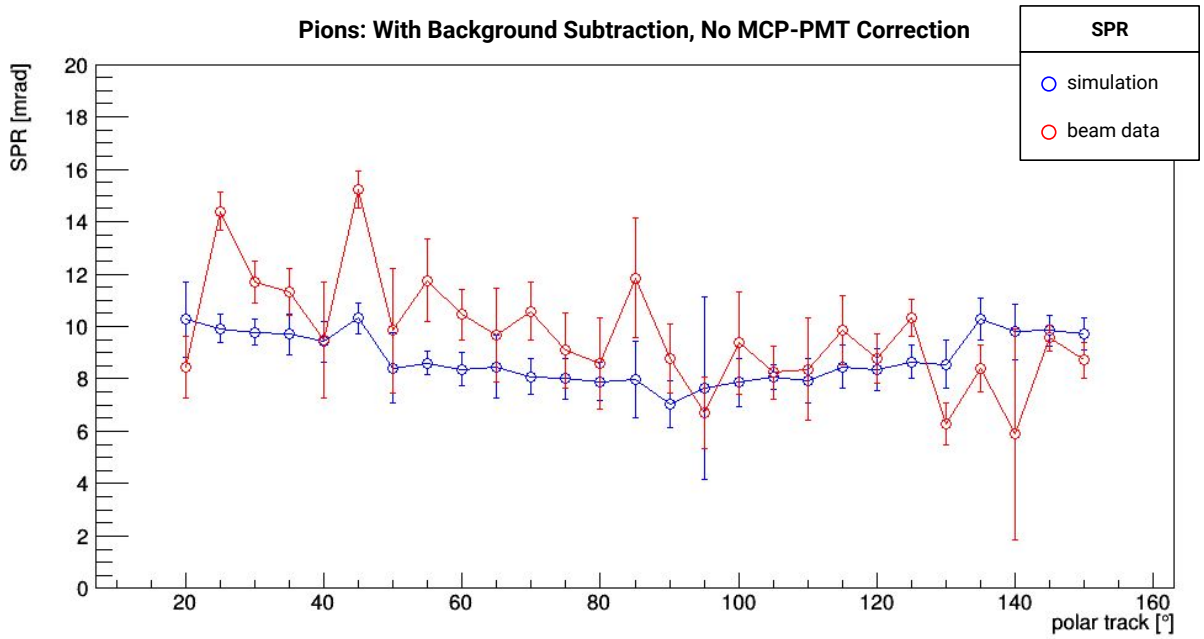

FIG. 81: Fitted SPR for pion-tagged events of study 151 of the CERN 2015 test beam data (red) and GEANT4 simulation (blue) using simulated background subtraction but no per-MCP-PMT correction.

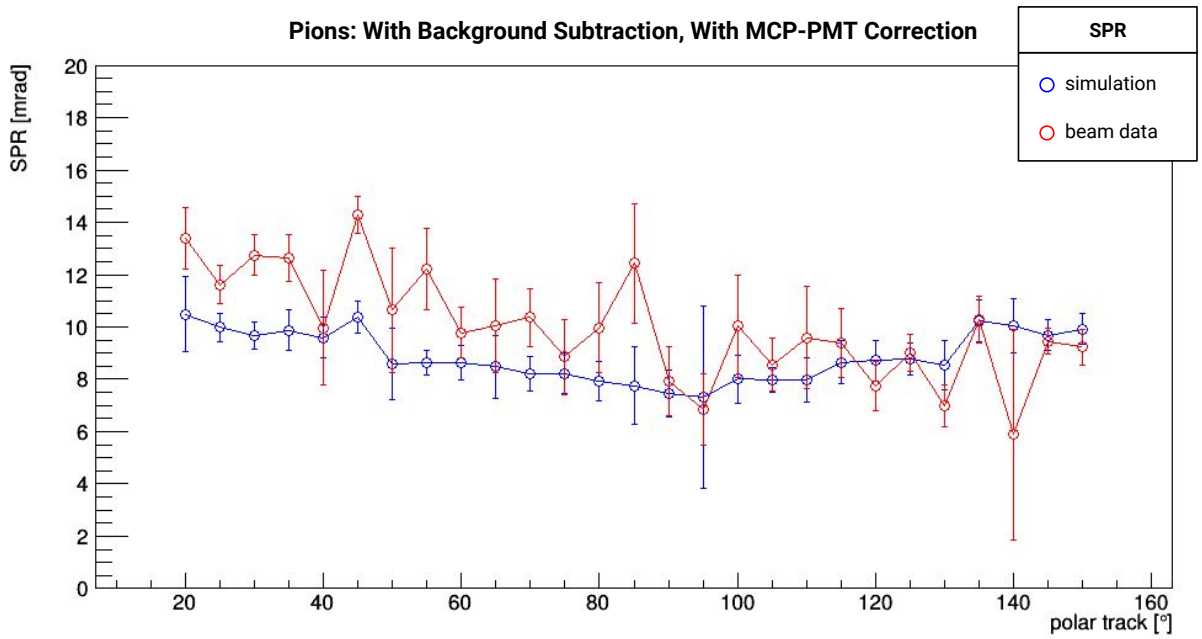

FIG. 82: Fitted SPR for pion-tagged events of study 151 of the CERN 2015 test beam data (red) and GEANT4 simulation (blue) using both simulated background subtraction and a per-MCP-PMT correction.

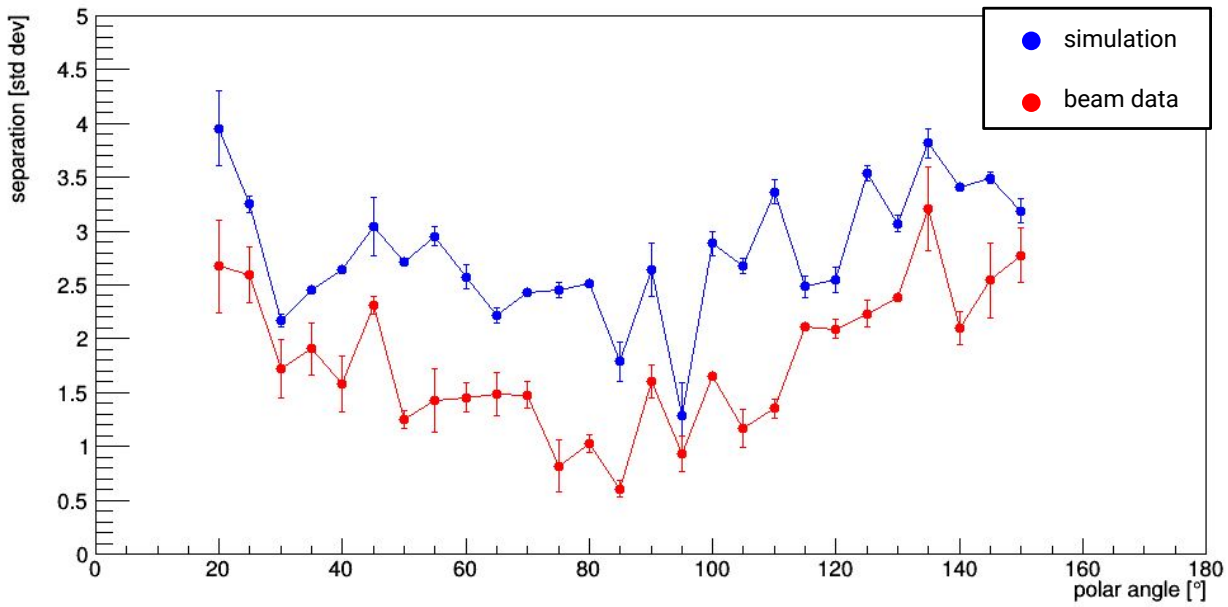

FIG. 83: Proton/pion log-likelihood separation using geometric reconstruction for simulation (blue) and beam data (red) using a 3-layer lens, radiator bar, and 7 GeV/c beam momentum.

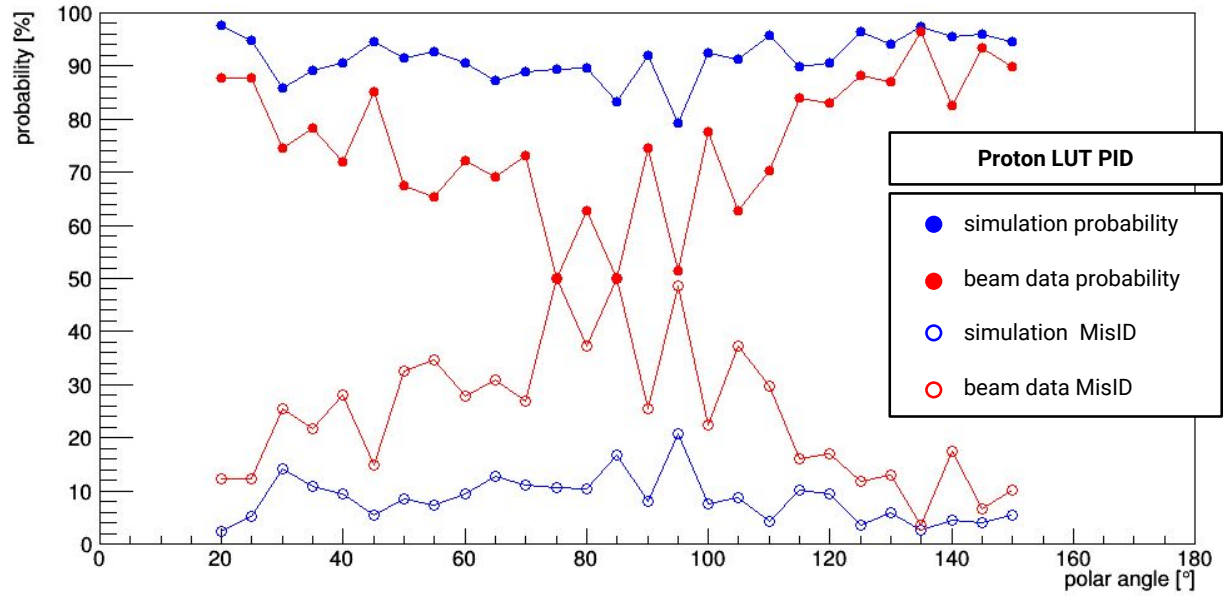

FIG. 84: PID (closed circles) and MisID (open circles) probabilities for simulated protons (blue) and tagged proton events in beam data (red). Results for pions are similar for both simulation and beam data.

6.3.3 TIME-BASED RECONSTRUCTION

The time-based reconstruction of the 2015 CERN data was done in the same manner as the time-based reconstruction of the EIC simulation described in Chapter 4. PDFs for the beam data were created by using every other event in a data file for both pions and protons. The reconstruction of the data was done with the other half of the data file to ensure no "cross talk" was occurring that would give an inaccurate result. Figure 85 shows the log-likelihood separation for 90° and 25° polar angles along with the separation power, given in unites of standard deviations (std dev) and calculated by dividing the distance between the two peaks of the distributions by their average standard deviations.

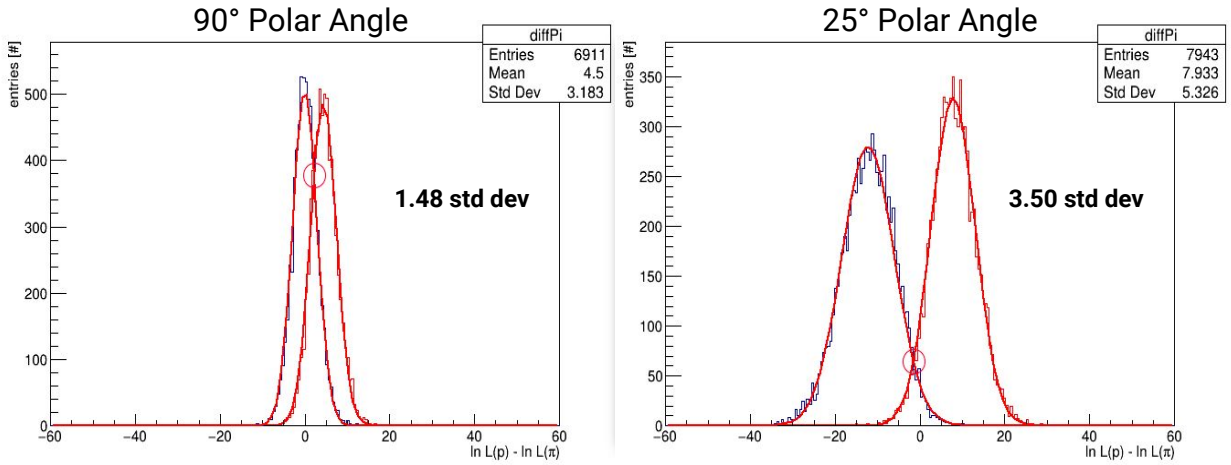

FIG. 85: Log-likelihood separation for 90° (left) and 25° (right) polar angles for pions (blue) and protons (red). Particles identified as protons will tend towards the right side of the zero point, while particles identified as pions will tend towards the left side of the zero point. The calculated separation power for each distribution are 1.48 and 3.5 standard deviations (std dev) respectively. The overlap of one curve under another will give the misidentification (MisID) of that species as being identified as the other.

Results

Figure 86 shows the separation power for the radiator bar with the 3-layer lens and 7 GeV/c beam momentum as a function of polar angle for simulation and beam data. Clearly the beam data was not able to reach the desired 3σ separation. This is caused in part by the timing resolution, which for the prototype was a factor of 2-3 worse than expected. Another factor contributing to the discrepancy is the photon detection efficiency loss of the lower quality MCP-PMTs at the base of the expansion volume, as is evident by the lack of a rise

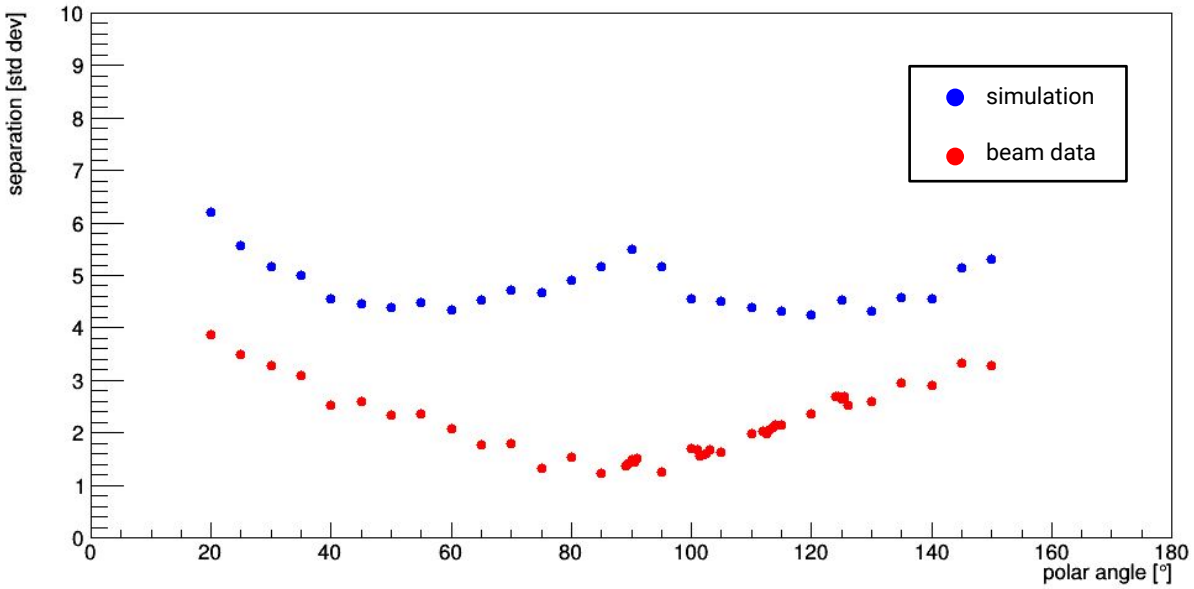

FIG. 86: Proton/pion log-likelihood separation using time-based imaging for simulation (blue) and beam data (red) using 3-layer lens, radiator bar, and 7 GeV/c beam momentum.

in the separation power near 90° polar angle in the beam data compared to simulation.

Figure 87 shows the PID and MisID probability for protons as a function of polar angle Results for pion PID and MisID probability are similar to that of the proton. Again, due to the worse timing resolution than expected, the MisID is much worse for the beam data than the simulation.

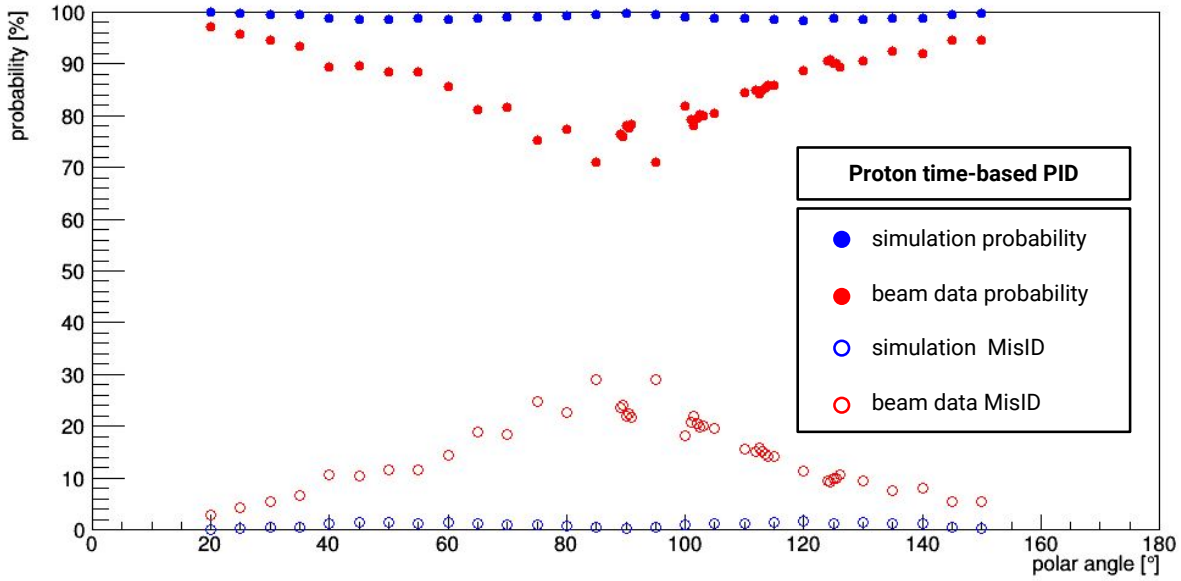

FIG. 87: PID (closed circles) and MisID (open circles) probabilities for simulated protons (blue) and tagged proton events in beam data (red). Results for pions are similar for both simulation and beam data.

CHAPTER 7

SUMMARY AND OUTLOOK

7.1 RESULTS

A DIRC detector is ideal for meeting the hadronic PID requirements in the barrel region of an EIC due to its small radial footprint and excellent particle separation capabilities at sub-10 GeV/c particle momentum. The current baseline design of the EIC DIRC is based on the compact PANDA DIRC design [21], featuring a compact expansion volume and lens-based focusing. Both geometric and time-based reconstruction analysis were done on the GEANT4 simulation of the EIC DIRC. For the geometric reconstruction Figure 30 shows a reasonable performance that would allow for 3σ π/K separation (see Figure 22 for reference) at 6 GeV/c momentum for most polar angles and dropping only slightly below 3σ if it is assumed that a large correlated term of 1 mrad will be seen in the actual experiment. In the case of the time-based reconstruction (Figure 33) the simulation again predicts a 3σ separation for a majority of the polar angle range of the detector, with performance dropping for polar angles near perpendicular.

While it would be ideal to test these simulation results directly with physical measurements, at this stage of the R&D effort it is more sensible to take advantage of the synergy between the EIC DIRC group and other DIRC groups rather than spend some large fraction of the PID R&D budget on a single EIC DIRC prototype. A synergistic test beam campaign was carried out during the summers of 2015 and 2016 with the PANDA Barrel DIRC group to study the performance of a PANDA DIRC detector prototype using the components envisioned for the EIC DIRC, namely a new 3-layer lens focusing optic designed to have a flat focal plane across the face of the MCP-PMT detector plane. Verification that the GEANT4 simulation using this PANDA prototype geometry agrees with experimental data is key in ensuring that the predicted performance of the EIC DIRC is valid.

Along with the analysis of the performance of the EIC DIRC 3-layer lens in a particle beam, it was also necessary to investigate the radiation hardness of the center layer of lanthanum crown glass [28], NLaK33, as well as the actual shape of the focal plane to compare with simulation. Measurements of the radiation hardness were carried out at the Catholic

University of America using 160 keV X-ray cabinet [32] for irradiation and a monochromator [34] for measuring the transmission of the glass after each irradiation step. It was found that the glass suffers approximately 1.3% transmission loss per 100 rad of delivered dose (Figure 45). It is, at the time of this writing, unknown what the expected dose delivered to the DIRC detector at an EIC will be over the lifetime of the experiment. Alternatives and solutions are discussed in the next section.

Measurements of the focal plane of the 3-layer lens were done at Old Dominion University using a custom-built laser setup and 3D printed lens holder. Initial measurements showed a systematic shift in the position of the focal plane between data and simulation by roughly 4 cm. After many measurements and adjustments to the setup it was found that the cause of this shift was most likely due to a non-zero angle between the two laser beams of roughly 0.15 mrad. After this adjustment was implemented in the simulation, the measured data very nicely reproduces both the shape and position of the predicted focal plane for multiple tilt angles and even when shifting the beam off-center of the lens.

The analysis of the 2015 CERN test beam data from the PANDA DIRC prototype focused primarily on the configuration with the 3-layer lens, bar radiator, and 7 GeV/c beam momentum in an attempt to closely match the parameters of the EIC DIRC baseline design. Both the geometric and time-based reconstruction methods were used to determine the performance of the prototype. The GEANT4 simulation is in good agreement with the results of the analyzed experimental data for both the photon yield and the single photon resolution, which gives confidence to the results presented in Chapter 4 for the EIC DIRC that the desired PID performance can be achieved by such a detector.

7.2 FUTURE WORK

There are still several steps to take in the R&D effort for the EIC DIRC: further studies of the radiation hardness of NLaK33, alternative materials for the lens design, and building a full, baseline-design-compatible EIC DIRC prototype.

Tests of the radiation hardness of NLaK33 were done with a somewhat thick (1 cm) piece of glass. The central layer of the 3-layer lens design, however, is set to 0.56 cm at the thickest portion, and thins out to 0.2 cm at the edge (see Figure 27). It is unclear what the penetration depth of NLaK33 is, and therefore how big of a change a smaller volume of material would have on the transmission. Talks are currently underway with a manufacturer to procure a piece of glass with a smaller thickness to test the penetration depth.

Along with testing the penetration depth of NLaK33, tests are also planned for exposing

the material to neutron radiation. Again, the neutron flux at the DIRC detector in an EIC is unclear, but having a feel for the type of neutron damage the material can withstand will help in the development of the lens.

If, after all radiation tests of the thinner NLaK33 piece are complete, it is found that it will lose as significant amount of transmission after a relatively short time of running then an alternative material must be found for the lens. Currently there are investigations into making the lens out of a different material called lead fluoride (PbF_2). PbF_2 is ideal because of its high refractive index, similar to that of NLaK33, and its proven high radiation hardness [58]. The challenge with using PbF_2 in the lens is that many manufacturers are unwilling to work with it due to the fear of contamination of their tools with lead.

In order to fully test the EIC DIRC design a prototype must be constructed and tested in a hadron beam. To carry out such a test beam campaign, MCP-PMTs with appropriately sized 3×3 mm^2 pixels (crucial for the desired resolution) along with a correctly sized expansion volume and radiator bars must be procured. Costs can be somewhat mitigated if radiator bars from previous experiments could be used instead of purchasing new bars. It is currently planned to include the costs of a full test beam in the US as part of the 2019 EIC budget for detector R&D.

In conclusion, a DIRC detector is an ideal solution for hadronic PID in the barrel region around the electron/ion interaction point of an EIC due to its compact radial size and resolving power for charged particles with sub-10 GeV/c momentum. Many milestones have so far been achieved in the R&D efforts, including the verification of the EIC DIRC simulation package via the 2015 CERN test beam, confirmation of the shape of the new 3-layer spherical lens design at ODU, limited radiation hardness testing of the NLaK33 material at CUA, and extensive studies of the influence of high magnetic fields on MCP-PMTs at JLab.

BIBLIOGRAPHY

[1] P. Coyle, B. Ratcliff, et al. The DIRC counter: A New type of particle identification device for B factories. *Nucl. Instrum. Meth.*, A343:292–299, 1994.

[2] I. Adam et al. The DIRC particle identification system for the BaBar experiment. *Nucl. Instrum. Meth.*, A538:281–357, 2005.

[3] G. Zweig. An SU(3) model for strong interaction symmetry and its breaking. Version 2. In D.B. Lichtenberg and Simon Peter Rosen, editors, *DEVELOPMENTS IN THE QUARK THEORY OF HADRONS. VOL. 1. 1964 - 1978*, pages 22–101. 1964.

[4] H. Fritzsch and M. Gell-Mann. Current algebra: Quarks and what else? *eConf*, C720906V2:135–165, 1972. Proceedings, 16th International Conference on High-Energy Physics, ICHEP, Batavia, Illinois, 6-13 Sep 1972.

[5] R. Tribble et al. *Frontiers of Nuclear Science*. 2007. `http://science.energy.gov/np/nsac/`.

[6] A. Aprahamian et al. Reaching For the Horizon: The 2015 Long Range Plan For Nuclear Science. 2015.

[7] S. Shimizu. Low Q^2 Structure Functions including the Longitudinal Structure Function. In *QCD and high energy interactions. Proceedings, 44th Rencontres de Moriond, La Thuile, Italy, March 14-21, 2009*, pages 301–304, 2009. http://inspirehep.net/record/821571/files/arXiv:0905.4712.pdf.

[8] A. Accardi et al. Electron Ion Collider: The Next QCD Frontier - Understanding the glue that binds us all. *Eur. Phys. J.*, A52(9):268, 2016.

[9] L. B. Weinstein et al. Short Range Correlations and the EMC Effect. *Phys. Rev. Lett.*, 106:052301, 2011.

[10] S. Malace et al. The Challenge of the EMC Effect: existing data and future directions. *Int. J. Mod. Phys.*, E23(08):1430013, 2014.

[11] V. Guzey et al. Evidence for nuclear gluon shadowing from the ALICE measurements of PbPb ultraperipheral exclusive J/ψ production. *Phys. Lett.*, B726:290–295, 2013.

[12] S. Abeyratne et al. MEIC Design Summary. 2015. https://arxiv.org/abs/1504.07961.

[13] E. C. Aschenauer et al. eRHIC Design Study: An Electron-Ion Collider at BNL. 2014. https://arxiv.org/abs/1409.1633.

[14] M. Alfred et al. eRD14 - EIC PID consortium: An integrated program for particle identification (PID) for a future Electron-Ion Collider (EIC) detector. Technical report, 2017. http://phynp6.phy-astr.gsu.edu/eRD14/images/8/8c/ERD14_FY17_proposal.pdf.

[15] A. A. Watson. The Discovery of Cherenkov Radiation and its use in the detection of extensive air showers. *Nucl. Phys. Proc. Suppl.*, 212-213:13–19, 2011. 100 years of cosmic ray physics: From pioneering experiments to physics in space. Proceedings, International Seminar, CRIS 2010, Catania, Italy, September 13-17, 2010.

[16] C. Grupen and I. Buvat, editors. *Handbook of particle detection and imaging, vol. 1 and vol.2*. Springer, Berlin, Germany, 2012. http://www.springer.com/978-3-642-13270-4.

[17] G. Kalicy. Development and Test of a Prototype for the PANDA Barrel DIRC Detector at FAIR. *International Atomic Energy Agency*, 47, 2014. https://inis.iaea.org/search/search.aspx?orig_q=RN:47087576.

[18] S. Agostinelli et al. GEANT4: A Simulation toolkit. *Nucl. Instrum. Meth.*, A506:250–303, 2003.

[19] J. Va'vra et al. The Focusing DIRC - the First RICH Detector to Correct the Chromatic Error by Timing, and the Development of a New TOF Detector Concept. In *Instrumentation. Proceedings, 11th International Conference, VCI 11, Vienna, Austria, February 19-24, 2007*, 2007. http://www-public.slac.stanford.edu/sciDoc/docMeta.aspx?slacPubNumber=slac-pub-12803.

[20] M. Borsato et al. The focusing DIRC: An innovative PID detector. *Nucl. Instrum. Meth.*, A732:333–337, 2013. Proceedings, 13th Vienna Conference on Instrumentation (VCI 2013): Vienna, Austria, February 11-15, 2013.

[21] R. Dzhygadlo et al. The PANDA Barrel DIRC. *JINST*, 11(05):C05013, 2016. Proceedings, Workshop on Fast Cherenkov Detectors: Photon detection, DIRC design and DAQ (DIRC2015): Giessen, Germany, November 11-13, 2015.

[22] E. Etzelmller et al. Tests and developments of the PANDA Endcap Disc DIRC. *JINST*, 11(04):C04014, 2016. Proceedings, Workshop on Fast Cherenkov Detectors: Photon detection, DIRC design and DAQ (DIRC2015): Giessen, Germany, November 11-13, 2015.

[23] E. Torassa. Particle identification with the TOP and ARICH detectors at Belle II. *Nucl. Instrum. Meth.*, A824:152–155, 2016. Proceedings, 13th Pisa Meeting on Advanced Detectors : Frontier Detectors for Frontier Physics (FDFP 2015): La Biodola, Isola d'Elba, Italy, May 24-30, 2015.

[24] K. Föhl et al. TORCH - Cherenkov and Time-of-Flight PID Detector for the LHCb Upgrade at CERN. *JINST*, 11(05):C05020, 2016. Proceedings, Workshop on Fast Cherenkov Detectors: Photon detection, DIRC design and DAQ (DIRC2015): Giessen, Germany, November 11-13, 2015.

[25] J. Stevens et al. The GlueX DIRC Project. *JINST*, 11(07):C07010, 2016. Proceedings, Workshop on Fast Cherenkov Detectors: Photon detection, DIRC design and DAQ (DIRC2015): Giessen, Germany, November 11-13, 2015.

[26] G. Kalicy et al. High-performance DIRC detector for the future Electron Ion Collider experiment. *JINST*, 11(07):C07015, 2016.

[27] J. Va'vra. Simulation of the Focusing DIRC Optics with Mathematica. In *2008 IEEE Nuclear Science Symposium, Medical Imaging Conference and 16th International Workshop on Room-Temperature Semiconductor X-Ray and Gamma-Ray Detectors*, pages 2408–2412, 2008. http://www-public.slac.stanford.edu/sciDoc/docMeta.aspx?slacPubNumber=slac-pub-13464.

[28] SCHOTT North America. *Optical Glass Data Sheets*, 6 2015.

[29] L. Allison et al. High-performance DIRC detector for use in an Electron-Ion Collider. *PoS*, ICHEP2016:300, 2016.

[30] Sonneborn, 600 Parsippany Road, Suite 100, Parsippany, NJ 07054. https://www.sonneborn.com/products/north-america-latin-america-asia-pacific/white-mineral-oils.

[31] J. Cohen-Tanugi et al. Optical properties of the DIRC fused silica Cherenkov radiator. *Nucl. Instrum. Meth.*, A515:680–700, 2003.

[32] Faxitron, 575 Bond Street, Lincholnshire, IL 60069.
http://www.faxitron.com/sites/default/files/pdf/CP-160.pdf.

[33] RaySafe, Uggledalsvgen 29, S-427 40 Billdal, Sweden.
http://mediabank.raysafe.com/A/RaySafe+Media+Bank/1717.

[34] PerkinElmer, 940 Winter Street Waltham, MA 02451.
http://www.perkinelmer.com/product/lambda-950-uv-vis-nir-spectrophotometer-l950.

[35] P. DeVore et al. Light-weight Flexible Magnetic Shields For Large-Aperture Photomultiplier Tubes. *Nucl. Instrum. Meth.*, A737:222–228, 2014.

[36] P. K. Lightfoot et al. Characterisation of a silicon photomultiplier device for applications in liquid argon based neutrino physics and dark matter searches. *JINST*, 3:P10001, 2008.

[37] Hamamatsu, 360 Foothill Road, Bridgewater NJ 08807.
http://www.hamamatsu.com/jp/en/community/silicon_photomultipliers/index.html.

[38] K. Inami. MCP-PMT development for Belle-II TOP counter. *Phys. Procedia*, 37:683–690, 2012. Proceedings, 2nd International Conference on Technology and Instrumentation in Particle Physics 2011: Chicago, Illinois, 9-14 Jun 2011.

[39] F. Uhlig et al. Performance studies of microchannel plate PMTs. *Nucl. Instrum. Meth.*, A695:68–70, 2012. Proceedings, 6th International Conference on New Developments in Photodetection (NDIP11): Lyon, France, July 4-8, 2011.

[40] A. Lehmann et al. Systematic studies of micro-channel plate PMTs. *Nucl. Instrum. Meth.*, A639:144–147, 2011. Proceedings, 7th International Workshop on Ring Imaging Cherenkov Detectors (RICH 2010): Cassis, France, May 3-7, 2010.

[41] A. Lehmann et al. Performance studies of microchannel plate PMTs in high magnetic fields. *Nucl. Instrum. Meth.*, A595:173–176, 2008. Proceedings, 6th International Workshop on Ring Imaging Cherenkov Detectors (RICH 2007): Trieste, Italy, October 15-20, 2007.

[42] S. Hirose. Performance of the MCP-PMT for the Belle II TOP counter in a magnetic field. *Nucl. Instrum. Meth.*, A766:163–166, 2014. Proceedings, 8th International Workshop on Ring Imaging Cherenkov Detectors (RICH 2013): Shonan, Kanagawa, Japan, December 2-6, 2013.

[43] M. Akatsu et al. MCP-PMT timing property for single photons. *Nucl. Instrum. Meth.*, A528:763–775, 2004.

[44] S. Korpar et al. Photonis MCP PMT as a light sensor for the Belle II RICH. *Nucl. Instrum. Meth.*, A639:162–164, 2011. Proceedings, 7th International Workshop on Ring Imaging Cherenkov Detectors (RICH 2010): Cassis, France, May 3-7, 2010.

[45] Y. Ilieva et al. MCP-PMT studies at the High-B test facility at Jefferson Lab. *JINST*, 11(03):C03061, 2016. Proceedings, Workshop on Fast Cherenkov Detectors: Photon detection, DIRC design and DAQ (DIRC2015): Giessen, Germany, November 11-13, 2015.

[46] PHOTONIS, Domaine de PELUS Axis Business Park - Bat 5 E 18 avenue de Pythagore 33700 Merignac, France. https://www.photonis.com/.

[47] Photek, 26 Castleham Road, St Leonards on Sea, East Sussex, TN38 9NS, United Kingdom. http://www.photek.com/pdf/datasheets/detectors/DS006_Photomultipliers.pdf.

[48] C. D. Keith et al. The Jefferson Lab Frozen Spin Target. *Nucl. Instrum. Meth.*, A684:27–35, 2012.

[49] L. Durieu et al. Optics Studies for the T9 Beam Line in the CERN PS East Area Secondary Beam Facility. C0106181:1547–1549, 2001. Particle accelerator. Proceedings, Conference, PAC 2001, Chicago, USA, June 18-22, 2001.

[50] J. Schwiening representing the PANDA Cherenkov Group. The PANDA Barrel DIRC Detector. 9th International Workshop on Ring Imaging Cherenkov Detectors (RICH 2016), 2016.

[51] Bosch Tools. https://www.boschtools.com/us/en/boschtools-ocs/line-lasers-gll-2-80-123125-p/.

[52] M. Cardinali. Frontend Electronics for high-precision single photo-electron timing. *PoS*, TIPP2014:180, 2014. Proceedings, 3rd International Conference on Technology and Instrumentation in Particle Physics (TIPP 2014): Amsterdam, Netherlands, June 2-6, 2014.

[53] Eljen Technology, 1300 W. Broadway Sweetwater, TX, 79556, USA. http://www.eljentechnology.com/products/accessories/ej-550-ej-552.

[54] Advanced Laser Diode Systems A.L.S GmbH, Schwarzschildstr. 6, D-12489 Berlin, Germany. http://www.alsgmbh.com/.

[55] PicoQuant, Rudower Chaussee 29 (IGZ), 12489 Berlin, Germany. https://www.picoquant.com/products/category/picosecond-pulsed-driver/pdl-800-d-picosecond-pulsed-diode-laser-driver-with-cw-capability.

[56] J. Michel et al. The HADES DAQ system: Trigger and readout board network. *IEEE Trans. Nucl. Sci.*, 58:1745–1750, 2011. Proceedings, 17th Conference on Computing Applications in Nuclear and Plasma Sciences on Real Time (RT2010): Lisbon, Portugal, May 24-28, 2010.

[57] R. Brun and F. Rademakers. Root - an object oriented data analysis framework. http://root.cern.ch/.

[58] A. Barysevich et al. Radiation damage of heavy crystalline detector materials by 24-GeV protons. *Nucl. Instrum. Meth.*, A701:231–234, 2013.

APPENDIX A

GEOMETRIC RECONSTRUCTION FITTING PARAMETERS

TABLE 2: Fitting information for the 2015 CERN test beam set 151 data. The fit is shown as a gaussian (main peak) plus some assumption of the back ground (e.g. pol0 for assumption of a flat background). The range of the fit is given as mrad away from the position of the main peak to the left (low) and right (high).

Polar Angle (°)	Particle	Fit (gaus+)	Range low (mrad)	Range high (mrad)
20	pion	pol2	-30	+30
20	proton	pol2	-25	+60
25	pion	pol0	-35	+35
25	proton	pol2	-40	+45
30	pion	pol2	-40	+40
30	proton	pol1	-30	+50
35	pion	pol1	-40	+40
35	proton	pol1	-25	+35
40	pion	pol2	-30	+35
40	proton	pol2	-30	+45
45	pion	pol0	-35	+50
45	proton	pol0	-60	+60
50	pion	pol2	-35	+55
50	proton	pol2	-30	+40
55	pion	pol2	-35	+40
55	proton	pol0	-30	+30
60	pion	pol2	-30	+45
60	proton	pol2	-30	+45
65	pion	pol1	-35	+30
65	proton	pol2	-20	+25
70	pion	pol2	-35	+40
70	proton	pol2	-40	+50
75	pion	pol2	-30	+25

TABLE 2: Fitting information for the 2015 CERN test beam set 151 data. The fit is shown as a gaussian (main peak) plus some assumption of the back ground (e.g. pol0 for assumption of a flat background). The range of the fit is given as mrad away from the position of the main peak to the left (low) and right (high).

Polar Angle (°)	Particle	Fit (gaus+)	Range low (mrad)	Range high (mrad)
75	proton	pol2	-35	+35
80	pion	pol2	-30	+50
80	proton	pol2	-35	+35
85	pion	pol2	-40	+60
85	proton	pol2	-30	+35
90	pion	pol2	-40	+40
90	proton	pol2	-45	+45
95	pion	pol2	-50	+35
95	proton	pol2	-50	+30
100	pion	pol2	-50	+50
100	proton	pol2	-35	+35
105	pion	pol2	-30	+40
105	proton	pol1	-45	+30
110	pion	pol2	-40	+40
110	proton	pol2	-30	+45
115	pion	pol1	-50	+35
115	proton	pol0	-30	+30
120	pion	pol2	-50	+50
120	proton	pol2	-40	+40
125	pion	pol0	-50	+50
125	proton	pol2	-35	+35
130	pion	pol2	-25	+35
130	proton	pol2	-35	+60
135	pion	pol0	-50	+50
135	proton	pol0	-30	+30
140	pion	pol0	-20	+35
140	proton	pol2	-30	+30
145	pion	pol0	-30	+30

TABLE 2: Fitting information for the 2015 CERN test beam set 151 data. The fit is shown as a gaussian (main peak) plus some assumption of the back ground (e.g. pol0 for assumption of a flat background). The range of the fit is given as mrad away from the position of the main peak to the left (low) and right (high).

Polar Angle (°)	Particle	Fit (gaus+)	Range low (mrad)	Range high (mrad)
145	proton	pol0	-60	+60
150	pion	pol2	-40	+50
150	proton	pol2	-45	+30

APPENDIX B

ERROR EVALUATION FOR GEOMETRIC RECONSTRUCTION

TABLE 3: Evaluated errors for prototype DIRC data taken during the 2015 CERN test beam with bar radiator, 3-layer lens, 7 GeV/c beam momentum, and tagged proton events.

Polar Angle (°)	Quantity	Internal	Fitting	Binning	Time Cut	Stability
	photon yield (#)	1.417	-	-	-	-
20	SPR (mrad)	0.228	1.051	0.435	0.146	-
	mean θ_C (mrad)	0.313	0.392	0.157	0.195	-
		1.777	-	-	-	-
25		0.568	0.418	0.145	0.173	-
		0.385	0.173	0.095	0.153	-
		1.580	-	-	-	0.503
30		0.544	0.465	0.270	0.162	0.648
		0.413	0.311	0.167	0.198	0.426
		1.335	-	-	-	-
35		0.404	0.721	0.336	0.102	-
		0.480	0.171	0.264	0.299	-
		1.428	-	-	-	-
40		1.221	1.452	0.375	1.047	-
		0.561	0.585	0.174	0.198	-
		1.471	-	-	-	-
45		0.468	0.477	0.189	0.110	-
		0.321	0.196	0.124	0.182	-
		1.429	-	-	-	-
50		1.043	1.439	0.737	1.370	-
		0.926	3.862	0.551	0.441	-

TABLE 3: Evaluated errors for prototype DIRC data taken during the 2015 CERN test beam with bar radiator, 3-layer lens, 7 GeV/c beam momentum, and tagged proton events.

Polar Angle (°)	Quantity	Internal	Fitting	Binning	Time Cut	Stability
	photon yield (#)	1.708	-	-	-	-
55	SPR (mrad)	0.770	1.294	0.432	0.101	-
	mean θ_C (mrad)	0.452	0.246	0.198	0.128	-
		1.345	-	-	-	0.656
60		0.773	0.479	0.295	0.106	1.115
		0.655	0.262	0.167	0.036	1.768
		1.748	-	-	-	-
65		1.281	1.165	0.467	0.068	-
		0.659	0.494	0.202	0.013	-
		1.113	-	-	-	-
70		0.684	0.883	0.125	0.075	-
		0.569	0.291	0.092	0.084	-
		1.353	-	-	-	-
75		1.230	0.619	0.392	0.118	-
		0.888	0.479	0.234	0.319	-
		1.246	-	-	-	-
80		1.162	0.953	0.202	0.845	-
		0.714	0.445	0.129	0.104	-
		1.197	-	-	-	-
85		1.762	0.950	0.644	0.916	-
		1.904	0.794	0.315	0.264	-
		1.412	-	-	-	0.228
90		1.016	0.653	0.165	0.518	0.714
		0.537	0.433	0.150	0.322	0.014
		1.605	-	-	-	-
95		1.158	0.651	0.292	0.175	-
		1.069	0.332	0.421	0.512	-
		1.370	-	-	-	-
100		1.383	1.140	0.310	0.739	-
		0.726	0.266	0.199	0.093	-

TABLE 3: Evaluated errors for prototype DIRC data taken during the 2015 CERN test beam with bar radiator, 3-layer lens, 7 GeV/c beam momentum, and tagged proton events.

Polar Angle (°)	Quantity	Internal	Fitting	Binning	Time Cut	Stability
	photon yield (#)	1.250	-	-	-	-
105	SPR (mrad)	0.873	0.455	0.213	0.109	-
	mean θ_C (mrad)	0.809	0.139	0.136	0.241	-
		1.244	-	-	-	-
110		1.673	0.868	0.393	0.337	-
		0.569	0.251	0.175	0.063	-
		1.352	-	-	-	-
115		0.526	1.139	0.326	0.232	-
		0.629	0.247	0.292	0.177	-
		1.549	-	-	-	0.536
120		0.782	0.477	0.222	0.096	0.825
		0.417	0.151	0.133	0.073	1.479
		1.326	-	-	-	-
125		0.575	0.302	0.235	0.064	-
		0.355	0.210	0.143	0.081	-
		1.887	-	-	-	-
130		0.429	0.609	0.288	0.071	-
		0.311	0.506	0.186	0.068	-
		1.246	-	-	-	-
135		0.419	0.745	0.268	0.048	-
		0.271	0.456	0.160	0.062	-
		1.641	-	-	-	-
140		2.519	0.822	0.227	3.018	-
		0.335	0.226	0.181	0.138	-
		1.851	-	-	-	-
145		0.225	0.400	0.108	0.144	-
		0.284	0.135	0.082	0.139	-
		1.465	-	-	-	0.748
150		0.375	0.537	0.160	0.162	0.409
		0.411	0.236	0.090	0.090	1.145

TABLE 4: Evaluated errors for prototype DIRC simulation with bar radiator, 3-layer lens, and 7 GeV/c protons.

Polar Angle (°)	Quantity	Internal	Fitting	Binning	Time Cut
	photon yield (#)	2.019	-	-	-
20	SPR (mrad)	0.590	1.183	0.527	0.126
	mean θ_C (mrad)	0.391	0.787	0.134	0.218
		0.998	-	-	-
25		0.403	0.337	0.108	0.066
		0.400	0.220	0.099	0.215
		1.086	-	-	-
30		0.376	0.265	0.138	0.182
		0.430	0.185	0.095	0.228
		0.925	-	-	-
35		0.636	0.329	0.206	0.220
		0.449	0.276	0.148	0.055
		1.018	-	-	-
40		0.582	0.467	0.190	0.105
		0.385	0.238	0.149	0.112
		1.071	-	-	-
45		0.444	0.287	0.127	0.268
		0.404	0.068	0.123	0.129
		0.497	-	-	-
50		1.008	0.736	0.389	0.389
		0.673	0.542	0.216	0.092
		0.898	-	-	-
55		0.377	0.209	0.142	0.053
		0.371	0.043	0.117	0.089
		0.982	-	-	-
60		0.518	0.344	0.113	0.132
		0.300	0.167	0.095	0.017
		0.782	-	-	-
65		0.427	0.775	0.577	0.592
		0.350	0.417	0.243	0.199

TABLE 4: Evaluated errors for prototype DIRC simulation with bar radiator, 3-layer lens, and 7 GeV/c protons.

Polar Angle (°)	Quantity	Internal	Fitting	Binning	Time Cut
	photon yield (#)	0.593	-	-	-
70	SPR (mrad)	0.465	0.424	0.217	0.074
	mean θ_C (mrad)	0.455	0.139	0.139	0.018
		0.466	-	-	-
75		0.689	0.286	0.215	0.078
		0.463	0.121	0.207	0.060
		0.554	-	-	-
80		0.627	0.352	0.163	0.020
		0.384	0.116	0.168	0.047
		0.667	-	-	-
85		1.246	0.548	0.161	0.548
		0.619	0.171	0.135	0.030
		0.613	-	-	-
90		0.531	0.632	0.325	0.126
		0.396	0.334	0.199	0.120
		0.781	-	-	-
95		1.311	1.747	0.867	2.579
		2.105	0.910	0.482	0.073
		0.715	-	-	-
100		0.589	0.555	0.168	0.385
		0.397	0.176	0.198	0.025
		0.761	-	-	-
105		0.346	0.232	0.191	0.072
		0.414	0.122	0.174	0.062
		0.706	-	-	-
110		0.531	0.610	0.244	0.050
		0.559	0.208	0.199	0.012
		0.951	-	-	-
115		0.693	0.372	0.231	0.069
		0.391	0.116	0.103	0.044

TABLE 4: Evaluated errors for prototype DIRC simulation with bar radiator, 3-layer lens, and 7 GeV/c protons.

Polar Angle (°)	Quantity	Internal	Fitting	Binning	Time Cut
	photon yield (#)	0.653	-	-	-
120	SPR (mrad)	0.635	0.433	0.186	0.047
	mean θ_C (mrad)	0.446	0.207	0.153	0.068
		0.711	-	-	-
125		0.537	0.269	0.155	0.048
		0.342	0.063	0.100	0.007
		0.804	-	-	-
130		0.708	0.534	0.252	0.134
		0.362	0.462	0.148	0.035
		0.748	-	-	-
135		0.535	0.544	0.234	0.116
		0.236	0.151	0.208	0.080
		0.843	-	-	-
140		0.831	0.437	0.319	0.365
		0.412	0.152	0.225	0.130
		1.386	-	-	-
145		0.250	0.521	0.085	0.073
		0.282	0.098	0.087	0.188
		1.428	-	-	-
150		0.430	0.319	0.259	0.041
		0.292	0.227	0.119	0.124

VITA

Stacey Lee Allison
Department of Physics
Old Dominion University
Norfolk, VA 23529

Education

Old Dominion University, Norfolk, VA

- PhD Candidate in experimental nuclear physics, 2012–Present
- Master of Science, 2014

University of North Georgia, Dahlonega, GA

- Bachelor of Science in Physics, 2012
- Bachelor of Science in Mathematics, 2012
- Minor in Computer Science, 2012

Research Experience

- 2015–Present: Graduate research assistant studying and optimizing the design of Electron-Ion Collider DIRC detector via hardware component tests and extensive Monte Carlo simulation.
- 2013–2015: Graduate research assistant running simulations and building electromagnetic calorimeter crystals for the Jefferson Lab Hall A DVCS experiment at Old Dominion University clean room.

Publications

- L. Allison, et al., "High-performance DIRC detector for use in an Electron-Ion Collider", PoS, **ICHEP** (2016) 300.
- V. Sulkosky, et al., "Studies of relative gain and timing response of fine-mesh photomultiplier tubes in high magnetic fields", NIST A, **827** (2016) 137.
- G. Kalicy, et al., "High-performance DIRC detector for the future Electron Ion Collider experiment", JINST, **11** (2016) C07015.
- Y. Ilieva, et al., "MCP-PMT studies at the High-B test facility at Jefferson Lab", JINST, **11** (2016) C03061.

Typeset using LaTeX.